2022 Ph.D. thesis

Novel quantum phases
accompanied by rotational symmetry breaking
in strongly correlated electron systems

強相関電子系における
回転対称性の破れを伴う新奇量子相の研究

January 21, 2022

Department of physics, Kyoto University
Student ID: 0560-31-2059

Hinako Murayama

Abstract

In strongly correlated electron systems, the interacting degrees of freedom, such as charge, spin, and orbital, bring the emergence of diverse quantum phases, e.g., high-T_c superconductivity. For decades, central issues in condensed matter physics have been the elucidation of such emergent quantum phases and their phase transition accompanied by various types of symmetry breaking. An interesting example is a doped Mott insulating system. Due to the strong correlation effect, many quantum phases appear in the vicinity of the Mott insulating state, such as density waves, unconventional superconductivities, etc. This thesis presents studies on novel quantum phases accompanied by rotational symmetry breaking which appear in the vicinity of a Mott insulating phase. An electronic order characterized by rotational symmetry breaking is called a nematic order on the analogy of a nematic liquid crystal. To study a nematic phase transition, we performed ultra-precision measurements of magnetic torque and observed minuscule magnetic anisotropy arising from the spontaneous rotational symmetry breaking. Since magnetic torque is a thermodynamic quantity sensitively probing magnetic anisotropy, it is a powerful probe of a nematic phase transition.

The first study has revealed rotational symmetry breaking in the pseudogap state of high-T_c cuprate superconductors. High-T_c superconductivity was found more than 30 years ago in a cuprate family, which has square lattices composed of copper and oxygen. Despite their simple crystal and band structure, the mechanism of the high-T_c superconductivity has been a long-standing mystery in condensed matter physics. The pseudogap phenomenon is a key for understanding electron correlation in the cuprates. The pseudogap is a partial gap opening at the Fermi level in the vicinity of the superconducting phase. The initial interpretation of the pseudogap was as a precursor of superconductivity since the superconductivity accompanies the gap opening in the quasiparticle excitations, leaving several nodal points gapless. However, recent studies have reported various types of symmetry breaking in the pseudogap state, hinting that the pseudogap phenomena result from an electronic ordering. However, there has been a lack of evidence for an occurrence of a thermodynamic phase transition at the pseudogap onset temperature. A recent torque study on orthorhombic $YBa_2Cu_3O_{6+\delta}$ revealed a nematic ordering simultaneously with the pseudogap formation. By studying the doping dependence, they suggested a spontaneous rotational symmetry breaking at the tetragonal limit. By performing the magnetic torque measurements on a tetragonal model compound of the cuprates, $HgBa_2CuO_{4+\delta}$, we observed a spontaneous rotational symmetry breaking from C_4 to C_2 at the pseudogap onset temperature. The detailed analysis provides that the order parameter symmetry is B_{2g} type, which is 45° apart from the B_{1g}-type nematicity in $YBa_2Cu_3O_{6+\delta}$. Furthermore, a competing relationship between the nematic order and the charge-density-wave order is

suggested by the suppression of the magnetic anisotropy below the charge-density-wave onset temperature. These findings improve understanding of the electron correlation and intricate phase diagram of cuprates.

The second study has identified an anapole order in the hidden order phase of $Sr_2Ir_{1-x}Rh_xO_4$. Sr_2IrO_4 is an analogous material of a cuprate La_2CuO_4. However, the $5d$ electron of Ir and twisted arrangement of IrO_6 octahedra result in a different electron correlation from the cuprates. The ground state is a spin-orbit assisted Mott insulator, in which a charge gap opens at the Fermi level due to the correlation effect enhanced by strong spin-orbit coupling. The electron-doped systems exhibit the pseudogap opening and Fermi arc as observed in the cuprates. On the other hand, a hole-doped system $Sr_2Ir_{1-x}Rh_xO_4$ exhibits various types of symmetry breaking in the vicinity of the antiferromagnetic phase, the region of which is called the hidden order phase. Although the symmetry breakings resemble the pseudogap phase of the cuprates, the hidden order lacked the evidence for a thermodynamic phase transition and the order parameter symmetry was not completely clarified. By performing the torque measurements, we revealed the symmetry reduction to B_{2g} in the hidden order phase. Combining the results of the elastoresistance measurements, we concluded that the order parameter symmetry is E_u type, which is odd parity. Therefore, since the time-reversal symmetry breaking was also observed in the previous study, the hidden order is an exotic charge order breaking many symmetries: inversion, rotational, and time-reversal. A microscopic mechanism for those symmetry breakings is provided by theories of loop current orders. In a loop current order, nano-size loop current flows between atoms, inducing local magnetization. By discussing the symmetry of the torque response in the hidden order phase, we propose a pattern of loop currents that is different from the previously proposed one. We name the order after an electromagnetic moment found in certain atomic nuclei: anapole. The finding implies that a strong spin-orbit coupling would bring new physics in strongly correlated electrons.

Contents

Chapter 1

Introduction

1.1 Nematicity

An electron in metal effectively behaves like a free particle because of the shielding effect. On the other hand, localization of d-orbital or f-orbital often makes the shielding imperfect, where a simple one-electron approximation is not valid due to non-negligible Coulomb repulsion among electrons. Such a system is called a strongly correlated electron system, in which numerous parameters strongly interact with each other. The interacting degrees of freedom such as charge, spin, and orbital bring the emergence of diverse quantum phases, e.g., high-T_c superconductivity. For decades, central issues in condensed matter physics have been the elucidation of such emergent quantum phases and their phase transition accompanied by various types of symmetry breaking.

An interesting example is a liquid-solid transition of electrons. In a metal, electrons move around with interaction like a liquid. Such a state is called Fermi liquid, in which the excitations are described by a quasiparticle carrying the charge and spin of an electron. On the other hand, strong on-site Coulomb repulsion freezes them on a lattice as if molecules freeze in a solid. The solid of electrons is called a Mott insulator. In a Mott insulator, a charge gap opens at the Fermi level due to the strong Coulomb repulsion, whereas a band theory predicts a metallic state. Between the liquid and the solid, there exist competing electronic states characterized by various types of symmetry breaking due to the strong correlation effect. One is a state characterized by rotational symmetry breaking [1]. It is called nematicity in the analogy of a nematic liquid crystal. As shown in figures 1.1(a–c), a system consisting of long molecules can have a nematic phase between a solid and a liquid. In a nematic phase, molecules move around like a liquid but the orientation aligns toward one direction like a solid. The nematic liquid crystal preserves the translational symmetry but breaks the rotational symmetry. The transition from the liquid to the nematic liquid crystal accompanies the rotational symmetry breaking. In strongly correlated electron systems, nematic phases have been theoretically studied from either a weak coupling or a strong coupling perspective.

Without any symmetry breaking, the shape of the Fermi surface reflects the underlying crystal symmetry. It was demonstrated by Pomeranchuk that a Fermi liquid is thermodynamically stable when the Landau parameters are large enough and positive [2]. When the conditions are violated, the system undergoes a quantum phase transition to lower
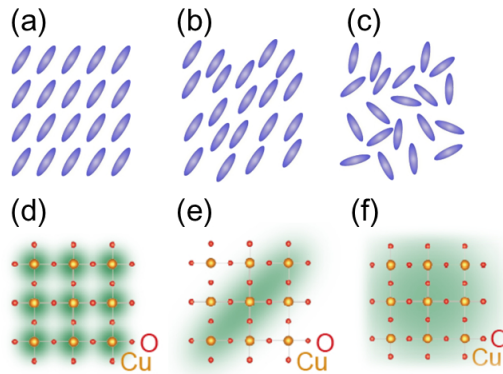
Figure 1.1: Cartoons for (a) solid, (b) nematic phase, (c) liquid in a system consisting of long molecules. (d) Mott insulator, (e) nematic order, (f) Fermi liquid of electrons in a solid.

symmetry accompanying the Fermi surface distortion [3], which is called a Pomeranchuk instability. Various models have been studied by perturbative approaches, leading to a nematic order by a Pomeranchuk mechanism [4–6]. On the other hand, nematic orders have been also studied from a perspective of partially melted stripe order such as density-wave state [7–12].

In this thesis, we present two examples for nematic orders in doped Mott insulators which are mapped onto a single-band Hubbard model on a 2D square lattice: a high-T_c cuprate superconductor [13, 14] and a spin-orbit assisted Mott insulator Sr_2IrO_4 [15].

1.2 High-T_c cuprate superconductors

1.2.1 Band structure and superconductivity

Cuprate is a family of copper oxide perovskite, some of which exhibit very high superconducting transition temperature T_c. The first discovery was reported on $La_{2-x}Ba_xCuO_4$ in 1986 [17]. The T_c exceeds the upper limit in Bardeen-Copper-Schrieffer (BCS) theory, which provides the microscopic mechanism for the superconductivity in conventional metal [18]. In the theory, the electrons form Cooper pairs and simultaneously condense by weak attractive interaction between electrons induced by electron-phonon coupling. However, distinct paring mechanisms were found in strongly correlated electron systems since electrons interact with each other in a more complex way. Such unconventional superconductors have been investigated for decades as a central issue in condensed matter physics. T_c of various superconductors is plotted as a function of the year of discovery in figure 1.2(a) [13]. Among the superconductors, the cuprate family has a record T_c at ambient pressure. The cuprate family has been attracting much attention not only due to the high-T_c superconductivity but also due to the complicated phase diagram with various quantum phases [13, 14].

Figure 1.2(b) shows the crystal structure of cuprate superconductors [19]. They have CuO_2 square lattices, which are separated by buffer layers. The number of the CuO_2 layers within the unit cell and the composition of the buffer layers are different among
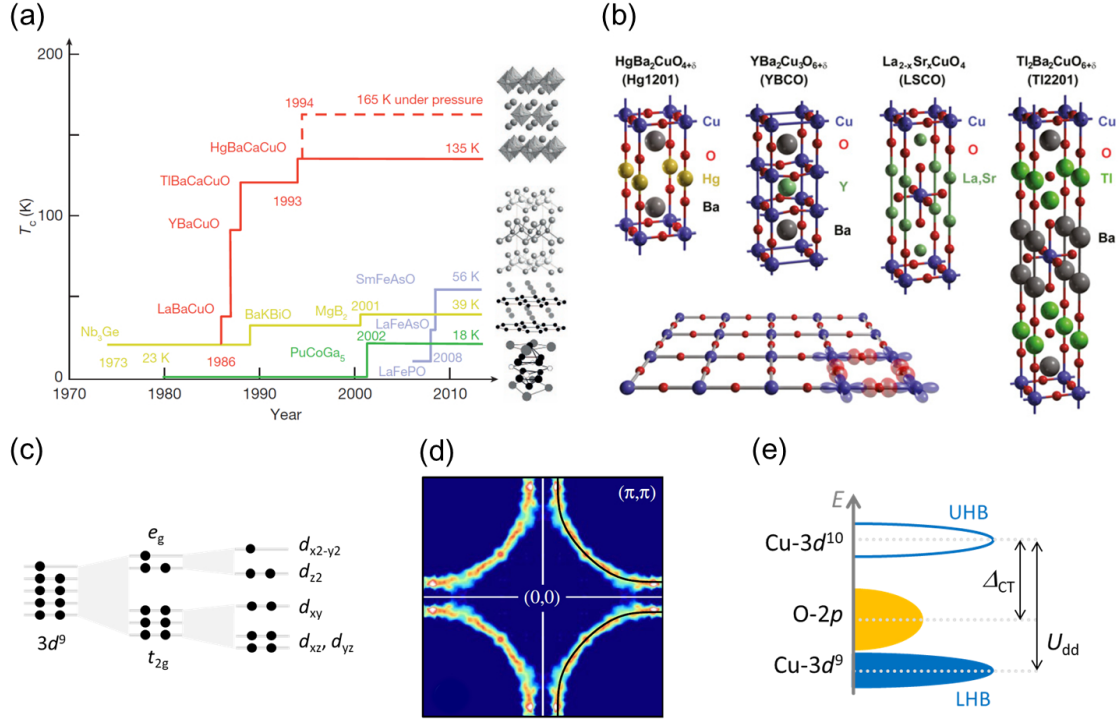
Figure 1.2: (a) The superconducting transition temperatures are plotted as a function of the year of discovery for various superconductors [13]. (b) The crystal structure of high-T_c cuprate superconductors. (c) Single ion picture of Cu $3d$ orbitals in the cuprate. (d) Fermi surface observed in ARPES measurements in overdoped Tl$_2$Ba$_2$CuO$_{6+\delta}$ [16]. (e) Band structure of the cuprates at the half-filling state.

the compounds. YBa$_2$Cu$_3$O$_{6+\delta}$ has an additional CuO-chain structure. In the cuprates, electrons are almost confined in the two-dimensional CuO$_2$ layer. Therefore, the minimal model is on a two-dimensional square lattice. Copper ions in the cuprate are in the Cu^{2+} state, having nine $3d$ electrons. A copper is surrounded by six oxygens forming the octahedral configuration. The oxygens induce a strong crystal field on Cu orbitals. The cubic crystal field splits the orbitals into two-fold degenerated e_g orbitals and three-fold degenerated t_g orbitals as shown in figure 1.2(c). In the cuprates, the octahedra are elongated in the normal direction to the layer by Jahn-Teller effect [20]. The distortion reduces the symmetry from the cubic to the tetragonal, removing the orbital degeneracy. The large Jahn-Teller distortion leaves only $3d_{x^2-y^2}$ orbital at the Fermi level. Figure 1.2(d) shows the Fermi surface observed in the angle-resolved photoemission spectroscopy (ARPES) on a heavily hole-doped Tl$_2$Ba$_2$CuO$_{6+\delta}$ ($T_c \sim 30\,\mathrm{K}$) [16]. A large hole Fermi surface surrounds (π, π) in the Brillouin zone. The Fermi surface is consistent with that of a single-band tight-binding model on a square lattice with finite next-nearest neighbor hopping (t'). The ratio to the nearest neighbor hopping (t) is typically $t'/t \sim 0.2$–0.4 [21]. It is well known that the sign and the size of t'/t are critical to the enhancement of the pairing correlation [22].

Though the half-filling state is metallic according to a band theory, the parent compounds are insulating due to the strong Coulomb repulsion. It is classified as a Mott
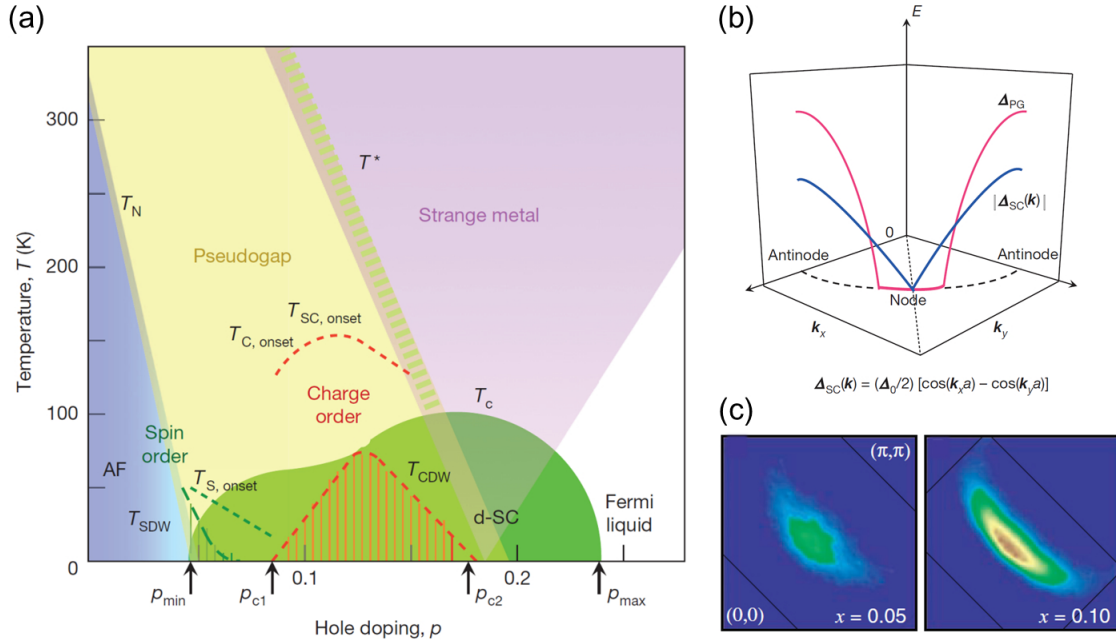
Figure 1.3: (a) A schematic phase diagram of the hole-doped high-T_c cuprate superconductors [13]. (b) A schematic of the superconducting gap Δ_{SC} and the pseudogap Δ_{PG} [13]. (c) The momentum distribution of spectral weight within $\pm 10\,\mathrm{meV}$ around the Fermi level in the ARPES measurements at $15\,\mathrm{K}$ on $Ca_{2-x}Na_xCuO_2Cl_2$ ($x = 0.05$ and 0.10) [32].

insulator [23]. The insulator-metal transition is well described by the single-band Hubbard model consisting of hopping (t) and onsite Coulomb repulsion (U) terms [24]. The model describes a metal when $U \ll t$ and a Mott insulator when $U \gg t$. Mott insulators are usually antiferromagnetic because the oppositely aligned neighboring spins can gain energy $4t^2/U$ by virtual hopping, which is called the exchange energy (J). Because of its single-band electronic structure and the presence of strong Coulomb repulsion, the cuprates have been theoretically studied with the one-band Hubbard model on a 2D square lattice.

Figure 1.2(e) shows the band structure of the parent compounds. Strong onsite Coulomb repulsion splits the Cu $3d_{x^2-y^2}$ band to the upper Hubbard band (UHB) and the lower Hubbard band (LHB). The gap size between these Hubbard bands is comparable to the onsite Coulomb repulsion on Cu site $U_{dd} \sim 10\,\mathrm{eV}$. In addition to the Hubbard bands, an oxygen $2p$ band exists between them. Electrons fill the O $2p$ band and the LHB, whereas the UHB is left empty. The lowest energy excitation is a charge transfer from O $2p_{x,y}$ to the neighboring Cu $3d_{x^2-y^2}$ [25–27]. Such an insulator is called a charge-transfer insulator [28]. The charge-transfer gap Δ_{CT} is $\sim 2\,\mathrm{eV}$. The magnetic moments on Cu sites exhibit a simple antiferromagnetic order around and below the room temperature [29,30]. The virtual hopping including oxygen $2p_{x,y}$ orbital results in extraordinarily large Cu-O-Cu superexchange interaction: $J \sim 0.13\,\mathrm{eV}$ in La_2CuO_4 [31]. The Néel temperature of La_2CuO_4 is $\sim 300\,\mathrm{K}$.

Due to the strong correlation in the cuprates, exotic electronic states appear by carrier doping as shown in the phase diagram of the hole-doping case (figure 1.3a). The hole dop-

ing on the parent compound rapidly suppresses the antiferromagnetic phase and changes the system metallic. The superconducting dome appears near the antiferromagnetic phase. The doping level corresponding to the maximum T_c is called the optimal dope. Materials below (above) the optimal doping level is referred to as underdoped (overdoped). The pairing in the cuprates is different from that in conventional s-wave superconductors. The superconducting wave function of the cuprate has $d_{x^2-y^2}$-wave symmetry, changing sign upon rotation by $90°$ [33–35]. The sign change requires the presence of a node in the (π, π) direction as shown in figure 1.3(b). The existence of gapless quasiparticle excitations at the node provides the thermodynamic properties distinct from the conventional superconductors. The d-wave symmetry of the superconductivity is explained by the pairing mediated by antiferromagnetic spin fluctuations [36–39], which survives in a wide range of hole concentration [40, 41]. However, understanding the superconductivity is not sufficient. Many other anomalous phenomena have been observed in the superconducting state of the cuprates. The pairing mechanism by antiferromagnetic spin fluctuations ignores the effect of strong electron-phonon coupling which may affect the superconductivity [42, 43]. Although d-wave superconductivity is easily degraded by structural disorder compared to s-wave one in BCS theory, the high-T_c superconductivity is strongly inhomogeneous [44]. Also, the superfluid density, a basic quantity for superconductivity, is anomalously small [45, 46]. Furthermore, since electrons are strongly correlated even at the optimal doping level, various unconventional electronic states coexist with the superconductivity in the phase diagram. Their nature and relation with the superconductivity are still elusive.

1.2.2 Fermi arc in the pseudogap state

A prominent electronic state in the cuprate is the pseudogap state, which exists in the underdoped region as shown with yellow area in figure 1.3(a). In early times, the pseudogap state was inferred by a reduction of the low-frequency spin excitations [47, 48]. In the pseudogap state, the out-of-plane resistivity shows a pronounced upturn [49], whereas the in-plane resistivity decreases [19, 50, 51]. The temperature dependence of the in-plane resistivity is proportional to T^2 at low temperature in the pseudogap state. The T^2 resistivity is consistent with the resistivity in a Fermi liquid. The magnetoresistance obeys Kohler's rule in one of the cuprates [52]. Although the transport property associates a Fermi liquid, electrons are strongly correlated in the underdoped regime. The conventional mean-field treatments like a Fermi liquid may fail to describe the pseudogap phenomenology.

The astonishing character of the pseudogap is a partial gap opening in the Fermi surface [53, 54]. As shown in figure 1.3(b), the quasiparticle excitations are gapped in the antinodal direction but gapless in the nodal direction. The Fermi surface in the pseudogap state has an end within the Brillouin zone, which is called the Fermi arc. Figure 1.3(c) shows the Fermi arc in the pseudogap state of $Ca_{2-x}Na_xCuO_2Cl_2$ observed in the ARPES measurements [32]. The momentum distribution of spectral weight is integrated within $\pm 10\,\mathrm{meV}$ around Fermi level for $x = 0.05$ and 0.10. The measurements were performed at $15\,\mathrm{K}$, which is higher than $T_c \sim 13\,\mathrm{K}$ in $x = 0.10$. $x = 0.05$ was not superconducting. In a Fermi liquid, the Fermi surface is the boundary between occupied and unoccupied states, which does not abruptly end inside the Brillouin zone. The effective potential with
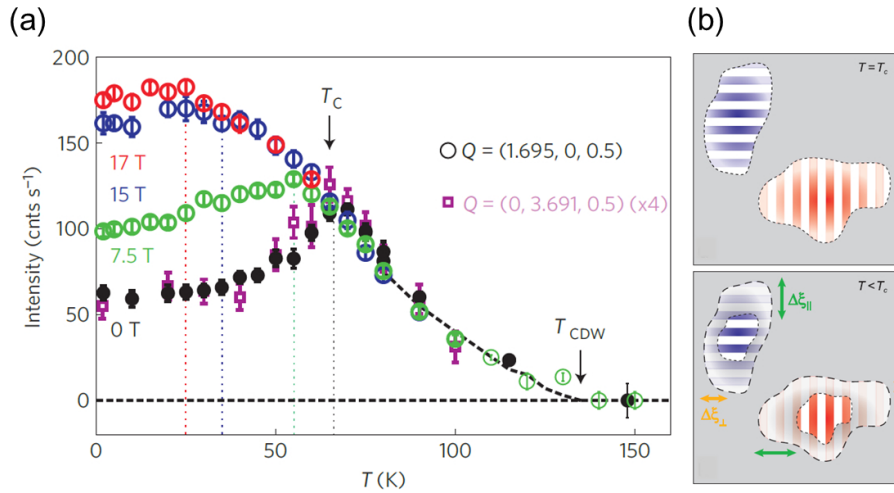
Figure 1.4: (a) The temperature dependence of the peak intensity at the satellite peak arising from the CDW order in the X-ray diffraction study on YBCO ($p = 0.12$) [65]. (b) Cartoons for the stripe charge order at zero field in YBCO [66].

translational symmetry breaking, such as a density-wave state, can reconstruct a large Fermi surface, producing a small Fermi pocket. Even in this case, the Fermi pocket must still form a connected manifold. Although some studies propose that the Fermi arcs can be the front half of such a pocket [55, 56], the backside of the pocket has not been observed yet. In the superconducting state, the Fermi arc was also observed in the underdoped region by the Bogoliubov quasiparticle interference in scanning tunneling spectroscopy (STS) measurements [35, 44, 57, 58].

Since the gap in the antinodal direction gradually evolves from the pseudogap state to the superconducting state by decreasing temperature, the partial gap opening was firstly attributed to the precursor of the pairing; pairs already start to form at the pseudogap onset temperature T^*, while large phase fluctuations prohibit the long-range order until temperature reaches T_c. The large fluctuations surviving much above T_c were observed by optical measurements [59–61]. Also, some ARPES and STS studies suggest that the Fermi arc is due to the lifetime broadening of a d-wave node [62–64]. If the pseudogap is due to precursor of the superconductivity, an occurrence of the pseudogap formation is a cross-over phenomenon.

1.2.3 Various types of symmetry breaking in the pseudogap state

On the other hand, recent experiments indicate that various electronic orders coexist in the pseudogap state, suggesting that the pseudogap formation results from an electronic ordering. One is a static density wave state appearing at low temperature in the pseudogap state. The incommensurate stripe spatial modulations of spin and charge density were firstly reported in the $La_{2-x}Sr_xCuO_4$ (LSCO) family [67]. The modulation occurs at $p \sim 1/8$ where the superconducting dome is suppressed. The stripes are metallic and even superconducting at low temperatures. Subsequently, the hourglass dispersion was found by inelastic neutron scattering [68]. The neck of the hourglass dispersion locates at the commensurate antiferromagnetic wave vector. The hourglass dispersion is associated with
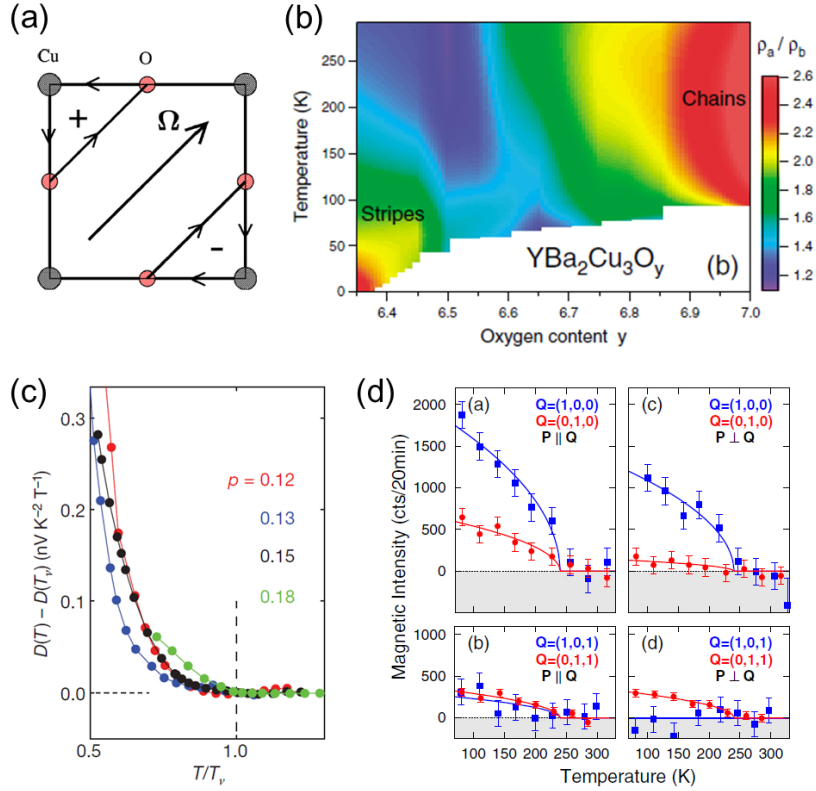
Figure 1.5: (a) Cartoon of a loop current order parameter defined with magnetization $(+, -)$ induced by a pair of loop current (arrows) [79]. (b) The in-plane anisotropy of the resistivity in YBCO is plotted as a function of temperature and oxygen content [80]. (c) The in-plane anisotropy of the Nernst coefficient D in underdoped YBCO is plotted as a function of the normalized temperature T/T_ν. T_ν is the onset temperature of the anisotropy [81]. (d) The temperature dependence of the spin-flip scattering intensity at Bragg peaks $\boldsymbol{Q}$ in spin-polarized neutron measurements on underdoped YBCO [82].

the incommensurate magnetic order, but it persists for larger doping where the stripe order is no longer condensed [69].

Recently, a short-range incommensurate charge density wave (CDW) was discovered in other hole-doped cuprates by X-ray measurements [70–73]. The X-ray measurements demonstrated a competing relationship between the short-range CDW and the superconductivity [65, 74, 75]. Figure 1.4(a) shows the scattering intensity at the satellite peak arising from the CDW order in the X-ray diffraction study on YBCO ($p = 0.12$) [65]. The peak appears at $T_{CDW} < T^*$ and smoothly evolves toward T_c, then abruptly drops below T_c. The typical onset temperature $T_{C,onset}$ is shown with a dotted line in the phase diagram (figure 1.3a). The intensity recovers by applying the magnetic field along the c-axis to suppress the superconductivity. The resonant X-ray scattering measurements revealed that the correlation length is also suppressed in the superconducting state [66]. Furthermore, the study found the pattern of the CDW in YBCO is stripe and not checkerboard as shown in figure 1.4(b). Under the high field, the presence of an electron pocket is suggested by transport measurements [76–78], which is associated with the Fermi surface reconstruction due to the CDW order.

Whereas the density wave states exist at temperatures much lower than the pseudo-gap onset temperature, breaking the translational symmetry, recent experimental studies reported an occurrence of other symmetry breakings at T^*. Those symmetry breakings suggest that the pseudogap state is an electronic order characterized by various types of symmetry breaking. The first observation is the time-reversal symmetry breaking in the ARPES measurements with circular polarization on Bi2212 [83]. The time-reversal symmetry breaking was also observed in the subsequent spin-polarized neutron scattering measurements on Hg1201 [84] and YBCO [85] . The intrinsic spin-flip scattering was observed below T^* at a Bragg peak without accompanying any additional peak, indicating the order is $\boldsymbol{q} = 0$ type. Those measurements are also discussed in section 3.1.2. The microscopic origin of the time-reversal symmetry breaking is theoretically proposed as loop current orders, which break various symmetries: time-reversal, rotational, and inversion [86, 87]. As shown in figure 1.5(a), a loop current order parameter Ω is defined by magnetization which is induced by a pair of loop currents, clockwise one and anticlockwise one, flowing between Cu and oxygen atoms within the unit cell. The order is also consistent with the inversion symmetry breaking, which was observed in optical second-harmonics generation (SHG) measurements in the pseudogap state of YBCO [88] and the antiferromagnetic phase of the parent compound $Sr_2CuO_2Cl_2$ [89].

1.2.4 Nematicity in the pseudogap state

Another symmetry breaking that is discussed in the pseudogap state is the four-fold rotational symmetry about the c-axis. In underdoped YBCO, a nematic tendency was observed by transport measurements [80, 81]. Figure 1.5(b) shows the in-plane anisotropy of the resistivity ρ_a/ρ_b of YBCO as a function of temperature and oxygen content [80]. The in-plane anisotropy is finite in the whole region because the crystal structure of YBCO is orthorhombic, which only has C_2 rotational symmetry about the c-axis. The anisotropy is enhanced toward the overdoped region due to the increase of the orthorhombicity by oxygen doping into the CuO chain. On the other hand, the anisotropy is also enhanced in a very underdoped regime, in which the crystal orthorhombicity is much decreased. The enhancement of the anisotropy suggests a strong nematic tendency in the underdoped region. However, the onset temperature of the enhancement does not correspond to the T^* line in the phase diagram. The nematic tendency was attributed to the stripe order rather than the pseudogap state.

The nematic tendency of YBCO was also observed in the Nernst response [81]. In the underdoped region of the hole-doped cuprates, large Nernst response was found, which has been associated with density-wave states [90–92]. Reference [81] discusses that the onset temperature of the Nernst response T_ν corresponds to the T^* line in YBCO. The Nernst coefficient when $\Delta T \parallel a$, ν_a, is different from that when $\Delta T \parallel b$, ν_b. The difference $D \equiv \nu_a - \nu_b$ is plotted as a function of the normalized temperature T/T_ν in figure 1.5(c). The finite anisotropy appears below T_ν, which corresponds to T^*. They also found the enhancement of the normalized anisotropy $(\nu_a - \nu_b)/(\nu_a + \nu_b)$, which can be viewed as a nematic order parameter. However, the later study of Nernst effect reported that the onset temperature of the nematicity was much lower than T^* [93]. They also discussed that the anisotropy near the optimally doped region arises from the CDW ordering. Therefore, it

is unclear how the nematic tendency relates to the pseudogap state.

The in-plane anisotropy was also reported in the spin-polarized scattering measurements. [82] as shown in figure 1.5(d). The blue squares and the red circles indicate the intrinsic spin-flip scattering intensity at the Bragg peak $\boldsymbol{Q} = (H, 0, L)$ and $(0, K, L)$, respectively. The scattering intensity is different between those two Bragg peaks, indicating the finite in-plane anisotropy. However, it is still unclear whether the $\boldsymbol{q} = 0$ order spontaneously breaks the rotational symmetry, or a nematicity existing above T^* makes the order anisotropic.

Recently, a nematic ordering at T^* was reported by the torque measurements on YBCO [94] (also discussed in section 3.1.4). The in-plane anisotropy of the susceptibility $\chi_{aa} - \chi_{bb}$ shows a kink at T^* as a function of temperature, and the anisotropy develops below T^*. It seems that the in-plane magnetic anisotropy consists of two anisotropy: the intrinsic large anisotropy of the pseudogap state and the background anisotropy due to the orthorhombic crystal structure. They studied doping dependence in detail, suggesting that the spontaneous rotational symmetry breaking occurs even at the tetragonal limit. The orthorhombicity of YBCO can act as an external field to nematic orders, coupling with a nematic order parameter and inducing a nematic order. However, the orthorhombiciy prevents the verification of the spontaneous symmetry breaking in the tetragonal limit. To verify if the nematic ordering is a universal phenomenon of the pseudogap state, it is important to observe the rotational symmetry breaking in a tetragonal system.

The STS measurements on Bi2212 suggest that the microscopic origin of the nematicity is anisotropy of oxygen $2p_x/p_y$ orbitals [58, 95, 96]. Figure 1.6(a) shows dI/dV spectra at low temperature for various doping levels. By decreasing the doping level, the V-shape gap splits into the inside gap Δ_0 and the outside one Δ_1. Δ_0 and Δ_1 are respectively the superconducting gap and the pseudogap. Δ_0 and Δ_1 are plotted as a function of energy and hole concentration in figure 1.6(b). Δ_0 and Δ_1 roughly track T_c and T^* in the $T - p$ phase diagram. Figure 1.6(c) shows the real space map of $Z(\boldsymbol{r}, \omega) \equiv \frac{dI/dV(\boldsymbol{r}, \omega)}{dI/dV(\boldsymbol{r}, -\omega)}$ at the pseudogap energy $\omega = \Delta_1$. The inset shows the Fourier transform $\tilde{Z}(q_x, 0)$ and $\tilde{Z}(0, q_y)$, indicating the in-plane anisotropy at the Bragg peaks $\boldsymbol{Q_x} = (1, 0)2\pi/a$ and $\boldsymbol{Q_y} = (0, 1)2\pi/a$. The Bragg peak anisotropy $O_n^Q(e) \equiv \frac{Re\tilde{Z}(\boldsymbol{Q_x}, e) - Re\tilde{Z}(\boldsymbol{Q_y}, e)}{\tilde{Z}(e)}$ evolves toward $e \sim \Delta_1$. To distinguish the contribution from oxygen site and Cu site, the real space anisotropy was calculated using $Z(\boldsymbol{R}, e = \Delta_1)$ at O_x and O_y sites shown in figure 1.6(d); $O_n^O \equiv \sum_R \frac{Z(R_x + a/2, R_y) - Z(R_x, R_y + a/2)}{\tilde{Z}(e)N}$. As well as the Bragg peak anisotropy, O_n^O evolves toward $e \sim \Delta_1$. On the other hand, the real space anisotropy calculated by Cu site $O_n^{Cu} \equiv \sum_R \frac{Z(R_x + a, R_y) - Z(R_x, R_y + a)}{\tilde{Z}(e)N}$ is negligible. These results suggest that the intra-unit-cell nematicity arises from the anisotropy of oxygen orbitals and the characteristic energy of the nematicity is close to the pseudogap energy. However, since the measurements were performed at low temperatures, it is unclear if the intra-unit-cell nematicity is identical to the nematicity appearing at the pseudogap onset temperature. The anisotropy at oxygen sites was also observed in the nuclear magnetic resonance measurements on the orthorhombic $YBa_2Cu_4O_8$ [97, 98]. The Knight shift between the two oxygens O_x and O_y are different only below the pseudogap onset temperature. Together with an idea of loop current order, the anisotropy at oxygen sites infers that the pseudogap phenomena may not be fully described by a single-orbital picture such as a single-band Hubbard model.

A recent STS study suggests that the characteristic energies of the $q = 0$ nematicity,
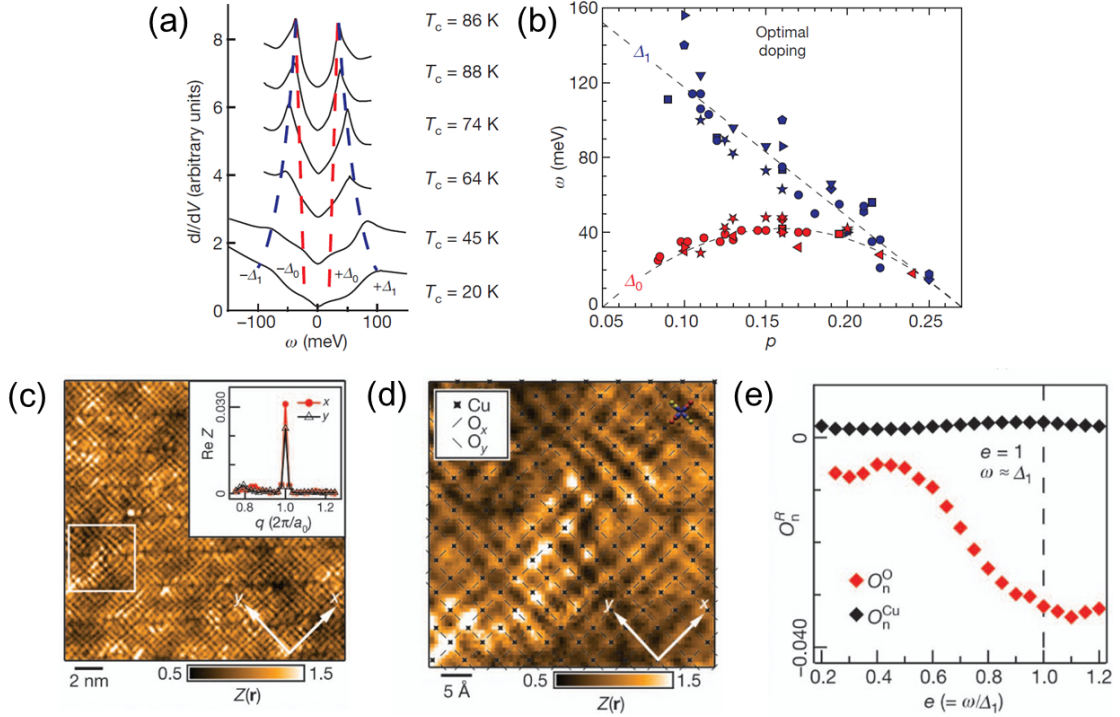
Figure 1.6: STS measurements on underdoped Bi2212 at $\approx 4.3\,\mathrm{K}$ [95]. (a) dI/dV spectra at low temperatures for various doping levels. Δ_0 and Δ_1 respectively indicate the super-conducting gap and the pseudogap. (b) Δ_0 and Δ_1 are plotted as a function of energy and hole concentration. (c) The real space map of $Z(\boldsymbol{r})$. The inset shows the momentum scan of the Fourier transform $\tilde{Z}(\boldsymbol{r})$. (d) The real space map of $Z(\boldsymbol{r})$. (e) O_n^O and O_n^{Cu} spectra.

CDW, and the pseudogap are consistent with each other, inferring that those phenomena originate in an identical order [96]. This is consistent with an idea of vestigial nematicity; quenched disorder destroys the long-range stripe CDW order, leaving the $\boldsymbol{q} = 0$ nematicity [99–101]. At the pseudogap onset temperature, a stripe CDW ordering may open a partial gap in the Fermi surface, but the disorder can destroy the long-range charge order, only allowing observation of $\boldsymbol{q} = 0$ nematicity.

1.2.5 Quantum criticality

In understanding the phase diagram, it is a longstanding argument if the pseudogap open-ing is a cross-over phenomenon or a thermodynamic phase transition. After the discovery of the pseudogap, the Fermi arc was firstly attributed to the precursor of superconduc-tivity [46]. In this scenario, T^* line extends toward the overdoped region so that the pseudogap region can cover the superconducting dome in the phase diagram. However, the change of Fermi surface topology, from a Fermi arc to a large Fermi surface, was observed inside the superconducting dome by STS measurements [58]. The current under-standing is that the pseudogap onset temperature T^* line continuously extends inside the superconducting dome as shown in figure 1.3(a). As discussed in previous sections, recent experimental observations suggest that electronic ordering occurs in the pseudogap state,

accompanying various types of symmetry breaking. This scenario infers an occurrence of a thermodynamic phase transition at T^*. In many studies on symmetry breaking, the measurements were performed in a range of hole concentrations in which $T^* > T_c$. For $T^* < T_c$, the time-reversal symmetry breaking was observed in optimally doped YBCO by a polar Kerr effect study [102]. However, there had been a lack of thermodynamic evidence for the phase transition at T^* for a long time. The recent torque study on orthorhombic YBCO reported a clear kink in the temperature dependence of the in-plane magnetic anisotropy, suggesting an occurrence of a nematic order at T^* [94]. It should be investigated if the thermodynamic transition at T^* also occurs in a tetragonal system.

If a continuous phase transition occurs at zero temperature at the terminal of T^* line, a quantum phase transition occurs at the corresponding quantum critical point (QCP) inside the superconducting dome. The presence of the QCP inside the superconducting dome suggests that strong fluctuations arising from the QCP may impact the pairing mechanism as discussed in other unconventional superconductors [103–105]. The presence of the QCP is suggested by a non-Fermi liquid behavior in the strange metal state (purple area in Figure 1.3a) [106]. The most basic difference between the strange metal and a conventional metal is the absence of quasiparticles. The T-linear resistivity was observed up to as high a temperature as measured [107], even when the mean free path was shorter than the electron de Broglie wavelength, violating the Heisenberg uncertainty principle for the quasiparticles. Some experimental anomalies in the strange metal were explained by the phenomenological marginal Fermi liquid [108]. Later, a quantum criticality was proposed to explain the low-energy excitations. The timescale $\hbar/k_B T$ characterizes the electronic dynamics of the strange metal [109–111], which is associated with Planckian dissipation [112]. It is inferred that any fundamentally perturbative approach starting with a free particle description cannot treat the pairing mechanism of the superconductivity.

Lastly, we note again the importance of understanding the pseudogap state to reveal the electron correlation and the pairing mechanism in the cuprate. We performed torque measurements on a model compound of the cuprate to clarify if an occurrence of the thermodynamic phase transition at T^* is universal in the cuprate. A tetragonal crystal $HgBa_2CuO_{4+\delta}$ was used so that we could verify if the nematicity in the pseudogap state arises from a spontaneous rotational symmetry breaking.

1.3 Spin-orbit assisted Mott insulator Sr_2IrO_4

1.3.1 Electronic structure and magnetism

Among transition metal oxides, many Mott insulators have been found in $3d$ electron systems such as the cuprate family. On the other hand, in $4d$ or $5d$ transition metal oxide, d-orbitals are more spatially extended, resulting in smaller on-site Coulomb repulsion. For example, Sr_2RhO_4, a $4d$ isostructural compound to a cuprate La_2CuO_4, is metallic [115, 116]. Although the Fermi surface is almost identical to Sr_2RhO_4 in a calculation without spin-orbit coupling (SOC) [117–120], a Mott insulating state was found in a $5d$ system Sr_2IrO_4 in 2008 [114, 120]. The mechanism of the Mott gap formation is closely related to strong SOC in the $5d$ orbital of Ir. Since the electronic structure is mapped onto a single-band Hubbard model on a 2D square lattice like the cuprate [121], various
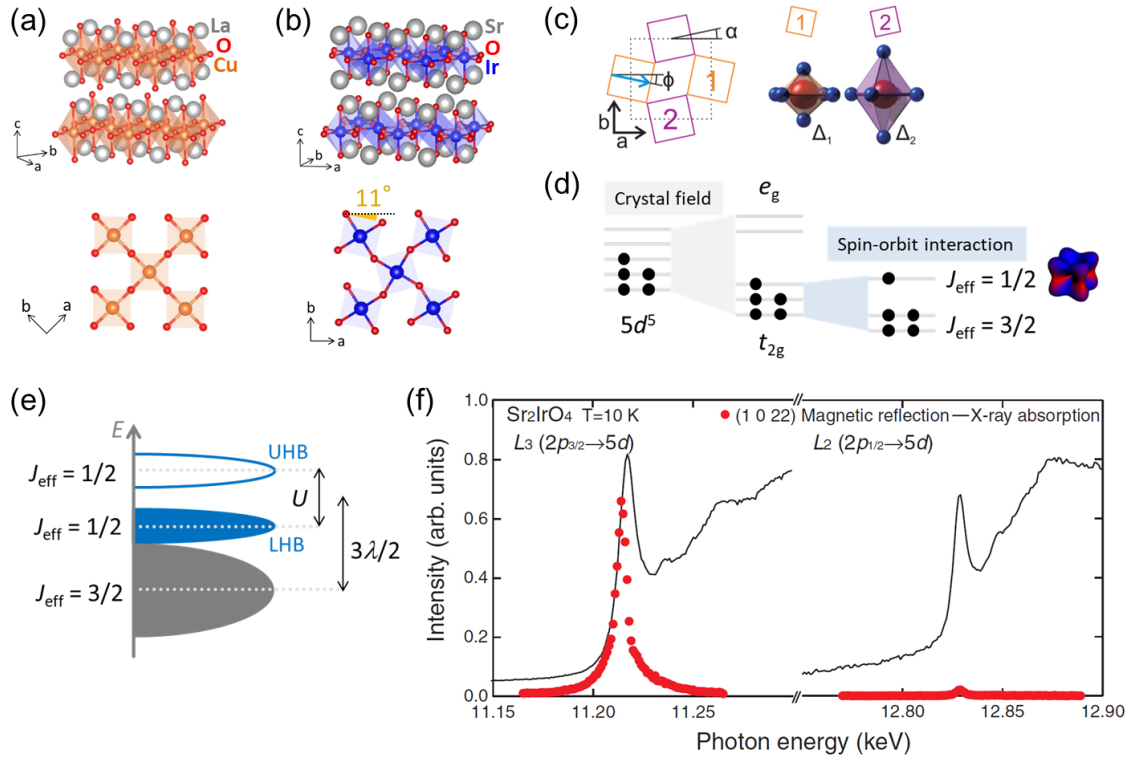
Figure 1.7: (a) Crystal structure of La_2CuO_4 and (b) Sr_2IrO_4. (c) Two different IrO_6 octahedra in Sr_2IrO_4 [113]. (d) Single ion picture of Sr_2IrO_4. (e) Band structure of Sr_2IrO_4. (f) Magnetic reflection $(1, 0, 22)$ (red circles) and X-ray absorption spectra (black line) at $L_3(2p_{3/2})$ and $L_2(2p_{1/2})$ edges in Sr_2IrO_4 [114].

competing electronic orders are expected in a doped Sr_2IrO_4. Furthermore, strong spin-orbit interaction would drive quantum phases distinct from those in the cuprate.

Figures 1.7(a,b) compare the crystal structure of La_2CuO_4 and Sr_2IrO_4. Like the square lattice of CuO_2 in La_2CuO_4, Ir-O bonds form a square lattice, but IrO_6 octahedra tilt to each other by $11°$. The octahedra rotation reduces the symmetry of the crystal to $I4_1/acd$. We just note that recent neutron and SHG studies propose a lower symmetry $I4_1/a$ [122,123]. They suggest that there exist two types of IrO_6 octahedra with a slightly different crystal field as shown in figure 1.7(c). The electronic structure in a single-ion picture is shown in figure 1.7(d). Ir ion takes Ir^{4+} state in Sr_2IrO_4, having five electrons in the $5d$ orbitals. The octahedral crystal field removes the degeneracy by splitting the $5d$ orbitals to e_g orbitals and t_{2g} orbitals. Since the system prefers the low-spin state, all the five electrons reside in the t_{2g} orbitals. Sr_2RhO_4, which is metallic, also has five electrons in the t_{2g} orbitals. However, the substitution of Rh with Ir enhances the SOC three times stronger $\lambda \sim 0.4\,\mathrm{eV}$, splitting the t_{2g} orbitals into $J_{eff} = 1/2$ and $J_{eff} = 3/2$. Only the narrow $J_{eff} = 1/2$ band remains near the Fermi level, which requires a moderate Coulomb interaction $\sim 2\,\mathrm{eV}$ to open a charge gap [124]. As shown in figure 1.7(e), there exist only the Hubbard bands near the Fermi level. Oxygen bands are well below the Fermi level [125], in contrast to the cuprate. The system is called a spin-orbit assisted Mott insulator. Indeed, the LDA+SOC+U solution reproduces the electronic band structure which was observed
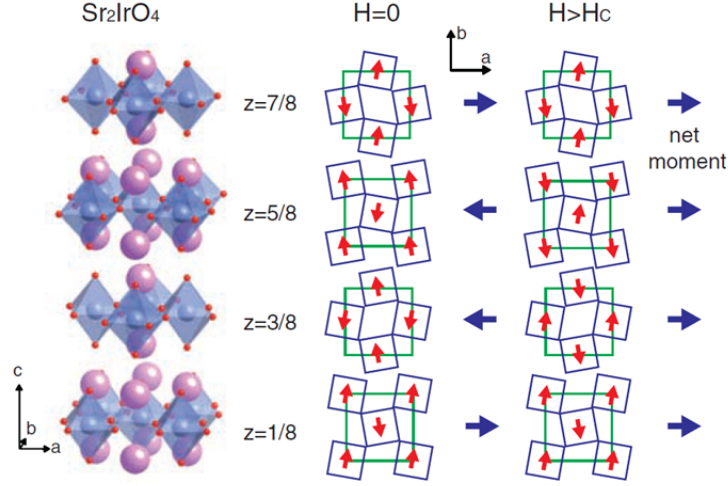
Figure 1.8: The magnetic moment configuration in the AFM phase of Sr_2IrO_4 [114].

in the ARPES measurements [120].

The $J_{eff} = 1/2$ state of Sr_2IrO_4 was studied by X-ray measurements [114]. Figure 1.7(f) shows X-ray absorption spectra (black line), in which the peak intensity at Ir L_3 edge is comparable to that at L_2 edge. Whereas X-ray absorption spectroscopy is a first-order process, resonant X-ray scattering (RXS) is a second-order process, which is sensitive to a phase of the wave function of valence electrons. In a $S = 1/2$ model, where t_{2g} splits to $|xy\rangle$ and $\{|yz\rangle, |zx\rangle\}$, $L_3(2p_{3/2} \to |xy\rangle)$ process and $L_2(2p_{1/2} \to |xy\rangle)$ process equally occurs. On the other hand, in $J_{eff} = 1/2$ state, the $L_2(2p_{1/2} \to J_{eff} = 1/2)$ process is much suppressed compared to the $L_3(2p_{3/2} \to J_{eff} = 1/2)$ process. Resonant scattering intensity at $(1, 0, 22)$ peak is shown with red circles in figure 1.7(f). The peak at the L_2 edge is strongly suppressed compared to the peak at the L_3 edge, suggesting that the valence band is the $J_{eff} = 1/2$ state. However, it is pointed out that the suppression of the L_2 edge does not necessarily imply the $J_{eff} = 1/2$ state when the pseudospin lies in the ab-plane [126–128]. A Slater insulator is also discussed in Sr_2IrO_4 [129] because of a significant gap reduction across $T_N \sim 240\,K$ [130, 131]. However, the charge gap is much larger than the magnetic energy scale $J \sim 60\,meV$ [132–134]. The current understanding of the ground state in Sr_2IrO_4 is a mixed Slater and Mott character [135–137].

In a tetragonal system, the tetragonal crystal field Δ mixes $J_{eff} = 1/2$ and $J_{eff} = 3/2$ states [124]. The Kramers doublets $\{|\tilde{\uparrow}\rangle, |\tilde{\downarrow}\rangle\}$ are written with $|L_z, S_z\rangle$. $|L_z = 0\rangle = |xy\rangle$ and $|L_z = \pm 1\rangle = \mp\frac{1}{\sqrt{2}}(|yz\rangle \pm i|za\rangle)$.

$$|\tilde{\uparrow}\rangle = +\sin\theta|0, \uparrow\rangle - \cos\theta|+1, \downarrow\rangle \qquad (1.1)$$
$$|\tilde{\downarrow}\rangle = -\sin\theta|0, \downarrow\rangle + \cos\theta|-1, \uparrow\rangle \qquad (1.2)$$

Here θ is a degree of the mixing, which is determined by the spin-orbit interaction λ and the tetragonal crystal field; $\tan 2\theta = 2\sqrt{2}\lambda/(\lambda - 2\Delta)$. The doublet is called a pseudospin. The pseudospin-1/2 moments are contributed more by orbital than by spin [120, 138]. The orbital-dominated magnetism is sensitive to the bond geometry. Therefore, the interaction between the pseudospins can be different from the Heisenberg interaction. For example,

Kitaev interaction is realized in a honeycomb lattice [124]. Magnetic interaction in Mott insulators is calculated through a virtual hopping between two neighboring sites. $|xy\rangle$, $|xz\rangle$, and $|yz\rangle$ are mixed up in $J_{eff} = 1/2$ state. In $180°$ bonding geometry, the hopping is allowed only between the same orbitals, resulting in isotropic Heisenberg interaction between the $J_{eff} = 1/2$ pseudospin in Sr_2IrO_4 [121, 124]. However, virtual excitations to $J_{eff} = 3/2$ state by finite Hund's coupling J_H can lead to anisotropic interaction. The pseudospin Hamiltonian is,

$$\mathcal{H} = \sum_{\langle i,j \rangle} J\boldsymbol{S}_i\boldsymbol{S}_j + \Gamma_1 S_i^z S_j^z \pm \Gamma_2(S_i^x S_j^x - S_i^y S_j^y) \tag{1.3}$$

Here Γ_1 and Γ_2 depend on θ and J_H/U. Since Γ_2 does not contribute to the classical energy, only Γ_1 leads to anisotropy. Γ_1 depends on fine-tuning of the parameters. A sizable anisotropy Γ_1 is suggested by using an experimentally determined value of $\Delta \sim 137\,\mathrm{meV}$ [15, 139].

In Sr_2IrO_4, the Néel transition occurs at $T_N \sim 240\,K$. The magnetic moment configuration is determined by resonant X-ray scattering and neutron diffraction as shown in figure 1.8 [114, 140]. The moments are locked along the octahedral direction, tilting to each other. The moment angle ϕ corresponds to the octahedral rotation angle α (figure 1.7c) in a cubic system. In a tetragonal system, the tetragonal crystal field Δ results in $\phi/\alpha \neq 1$ by mixing $J_{eff} = 1/2$ and $J_{eff} = 3/2$ states [124]. Although $\phi/\alpha \neq 1$ when $\Delta \neq 0$, the neutron study reports $\alpha \sim \phi$ in Sr_2IrO_4 [140] and even in $Sr_2Ir_{1-x}Rh_xO_4$ [122], where the SOC is reduced by Rh substitution. It is proposed that the robustness of ϕ/α can result from the different tetragonal crystal fields between the two octahedra as shown in 1.7(c) [113, 140].

Due to the canted moment configuration, each IrO_2 layer has a weak net ferromagnetic moment $\sim 0.14\,\mu_B/\mathrm{Ir}$ [141] which orders in a $(+ - -+)$ pattern along the c-axis by small interlayer couplings [142]. Above the critical field $H_c \approx 0.2\,\mathrm{T}$, the moment configuration is rearranged to a ferromagnetic $(+ + ++)$ pattern. In the antiferromagnetic phase, spin-wave dispersion was observed by RIXS measurements [134]. The dispersion is quite similar to that observed in La_2CuO_4, but the bandwidth of the magnon branch is smaller because of the reduced energy scale of t and U. The dispersion is well fitted with a Heisenberg Hamiltonian consisting of nearest neighbor antiferromagnetic interaction $\sim 60\,\mathrm{meV}$, second nearest neighbor ferromagnetic interaction $\sim -20\,\mathrm{meV}$, and third nearest neighbor antiferromagnetic interaction $\sim 15\,\mathrm{meV}$. Therefore, Sr_2IrO_4 realizes strongly correlated AFM on 2D square lattice. In the analogy of the cuprate, we expect various electronic orders in doped Sr_2IrO_4.

1.3.2 Pseudogap and symmetry breaking

It is proposed that the low-energy electron structure of Sr_2IrO_4 is mapped onto a pseudospin-1/2 Hubbard model on a square lattice [121]. Since the high-T_c superconductivity in the cuprates has been studied with a single-band Hubbard model, unconventional superconductivity is also expected in doped Sr_2IrO_4 [146–149]. Compared to the cuprates, the energy scale of the Hubbard model is about 50% smaller in Sr_2IrO_4. Although $5d$ orbitals are more spatially extended, the nearest neighbor hopping t is smaller by $\sim 60\%$ than that in the cuprates. This is because the $J_{eff} = 1/2$ state is less spread, reducing the overlap
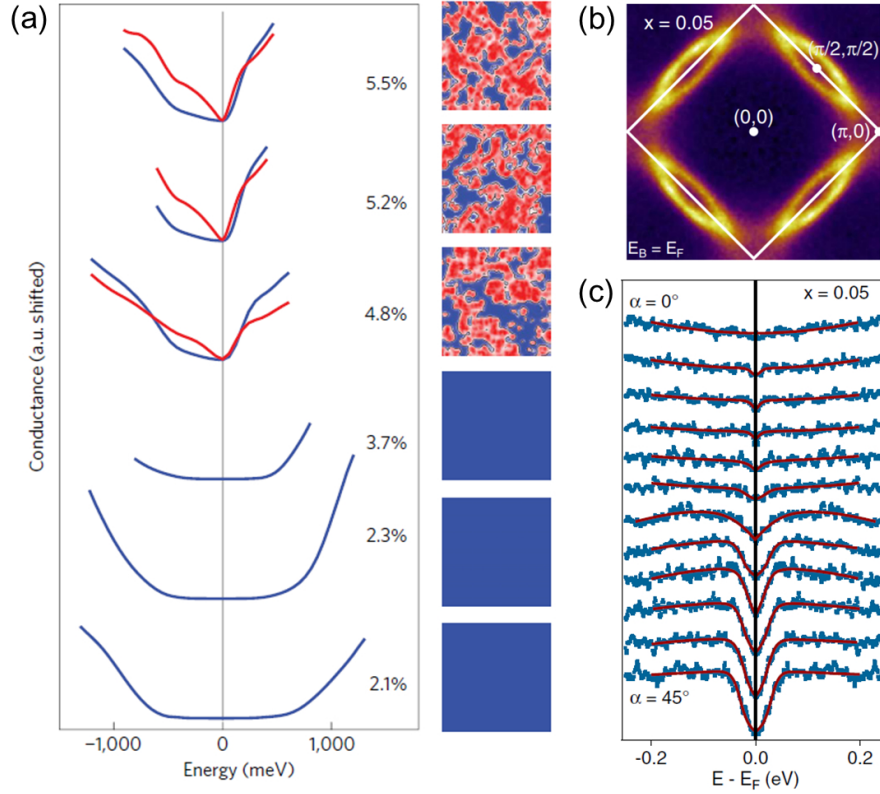
Figure 1.9: (a) Conductance spectra at 2-7 K in STM measurements on $Sr_{2-x}La_xIrO_4$ [143]. The pseudogap and Mott gap regions are mapped with red and blue colors respectively. (b) Constant energy contour and (c) symmetrized energy distribution curves of $x = 0.05$ at Fermi level in ARPES measurements [144]. The measurements were performed at 8 K. α is an angle from the (π, π) direction.

between the nearest neighbor pseudospins. Since U is also smaller in Sr_2IrO_4, the ratio t/U is close to that of the cuprates. In the cuprate, it is well known that the sign and the magnitude of the second nearest neighbor hopping t' are critical to the enhancement of the pairing correlation [22]. The ratio of nearest and second nearest-neighbor hopping is $|t'/t| \approx 0.23$ in Sr_2IrO_4, which is similar to the typical value in the cuprate [21]. On the other hand, the sign of t' is opposite to that of the cuprate. Since the sign is reversed by a particle-hole transformation, the doping phase diagram of Sr_2IrO_4 is expected to be the particle-hole conjugate to that of the cuprate. Adding an electron makes a closed shell both in the cuprate and Sr_2IrO_4. In the cuprate, removing an electron adds a hole in the oxygen $2p$ orbital rather than into Cu $3d$ orbital, leading to Zhang-Rice singlet state [150]. On the other hand, the hole is doped into d orbital in Sr_2IrO_4, leading to the low-spin d^4 configuration. Also, it is crucial if the single-band Hubbard model is also valid for doped Sr_2IrO_4.

La substitution at the Sr site dopes electron, suppressing the antiferromagnetic order by $\sim 3\%$ substitution [151–153]. The STM measurements on $Sr_{2-x}La_xIrO_4$ reported an appearance of V-shape gap for $x > 0.04$ as shown in figure 1.9(a) [143]. The gap is referred to as the pseudogap in the analogy of the cuprates. Within a sample, the pseudogap region
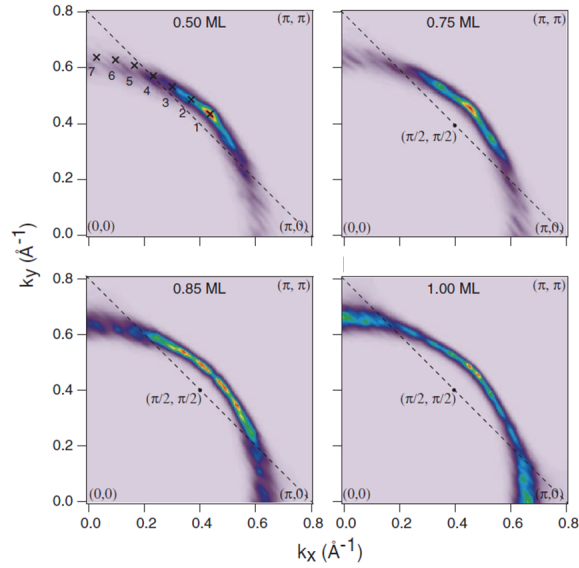
Figure 1.10: Constant energy maps at Fermi surface for different surface coverage of potassium observed in ARPES measurements at 70 K [145].

appears around clusters of dopant atoms in an inhomogeneous way. In $Sr_{2-x}La_xIrO_4$, Fermi arc was observed in the ARPES measurements [144, 154, 155]. Figure 1.9(b) shows the constant energy contour at the Fermi level for $x = 0.05$ which was observed in the ARPES measurements [144]. The Brillouin zone for undistorted square lattice is used in the figure, whereas the actual Brillouin zone is folded to the square (white line) by the structural distortion. The lens-like pocket in the (π, π) direction results from the back folding of the circular large Fermi surface by the structural distortion. On the other hand, the spectral weight is weak at the square pocket in the $(\pi, 0)$ direction which should be also created by the back folding. The gap opening in the $(\pi, 0)$ direction is demonstrated by angle dependence of symmetrized energy distribution curves as shown in Figure 1.9(c). The gap already opens at the edge of the lens. Therefore, the lens-like electron pocket is composed of two disconnected Fermi arcs. Another way of electron doping is in situ deposition of potassium atoms on a cleaved sample surface of Sr_2IrO_4 [145, 156]. The Fermi arc evolves to the large Fermi surface by increasing the potassium coverage as shown in figure 1.10. At one-monolayer covering (1ML) of potassium corresponds to $\sim 9\%$ electron doping.

On the other hand, hole doping is achieved by substituting Ir^{4+} with Rh^{3+} [122, 157–161]. The magnetic order is suppressed by $\sim 17\%$ [157, 158], which is much higher than La-doped case $\sim 3\%$. The difference suggests the hole-electron asymmetry in the phase diagram. In contrast to La doping, the spectral weight is observed at the square hole pocket in the $(\pi, 0)$ direction, which may consist of four Fermi arcs [159]. In the phase diagram of $Sr_2Ir_{1-x}Rh_xO_4$, a hidden order state exists in the vicinity of the antiferromagnetic phase, which is characterized by inversion, rotation, and time-reversal symmetry breaking [123, 162]. Since the observation is quite similar to that in the pseudogap phase of the cuprate, $Sr_2Ir_{1-x}Rh_xO_4$ has recently attracted much attention. The hidden order is discussed in detail in section 4.1.3. In the analogy of the cuprate, we expect electron nematicity in the

hidden order state. However, the hidden order lacks thermodynamic evidence for the phase transition, and the order parameter symmetry is not determined. To reveal the hidden order, we performed the magnetic torque measurements on $Sr_2Ir_{1-x}Rh_xO_4$, discussing the order parameter symmetry.

Chapter 2

Field-angle resolved magnetic torque measurement

Magnetic torque is a quantity that is sensitive to both magnetic anisotropy and phase transition because it is a field-angle derivative of free energy. Therefore, the magnetic torque is a powerful probe for nematic phase transition: phase transition accompanied by rotational symmetry breaking. This chapter firstly introduces previous studies on magnetic torque measurements. Second, the measurement principle and experimental setup are explained in detail. We also mention a careful treatment of the background signal at the end of the chapter.

2.1 Magnetic torque measurements

2.1.1 Free energy and phase transition

Torque $\boldsymbol{\tau}$ is a rotational force represented by a cross product of position $\boldsymbol{r}$ and force $\boldsymbol{F}$; $\boldsymbol{\tau} = \boldsymbol{r} \times \boldsymbol{F}$. The work W by the force is given by integrating the force along the displacement $d\boldsymbol{s}$; $W = \int \boldsymbol{F}(\boldsymbol{s})d\boldsymbol{s}$. The displacement of rotation is represented by the corresponding angular displacement $d\boldsymbol{\theta}$ and the radius vector $\boldsymbol{r}$; $d\boldsymbol{\theta} \times \boldsymbol{r}$. Since $W = \int \boldsymbol{F}(\theta)d\boldsymbol{\theta} \times \boldsymbol{r} = \int \boldsymbol{r} \times \boldsymbol{F}d\boldsymbol{\theta} = \int \boldsymbol{\tau}d\boldsymbol{\theta}$, an infinitesimal displacement around a fixed axis, $d\theta$, changes the free energy F by $-\tau d\theta$. In other words, torque is the angle derivative of the free energy; $\tau = -\partial F/\partial\theta$. Therefore, torque is sensitive to the magnetic anisotropy of free energy. In condensed matter physics, torque is often measured to study magnetization in materials. A magnetic moment $\boldsymbol{M}$ in an external field $\boldsymbol{B}$ has potential energy $-\boldsymbol{M} \cdot \boldsymbol{B}$. The field-angular derivative of the energy gives a torque $\boldsymbol{\tau} = \boldsymbol{M} \times \boldsymbol{H}$. The torque is called "magnetic torque", which rotates a crystal under the eternal field.

Torque measurements have been performed on magnets to study magnetic anisotropy. Almost the first study is on a single crystal of cubic $Ho_xTb_{1-x}Fe_2$ [163]. RFe_2 family orders magnetically below $\sim 600\,K$, having large magnetocrystalline anisotropy [164]. The magnetic anisotropy of free energy is directly probed by the field-angle dependence of the magnetic torque. Cubic expansion of the magnetocrystalline anisotropy energy E is;

$$
\begin{aligned}
E = K_0 + K_1(x^2y^2 + y^2z^2 + x^2z^2) + K_2x^2y^2z^2 + K_3(x^2y^2 + y^2z^2 + x^2z^2)^2 \\
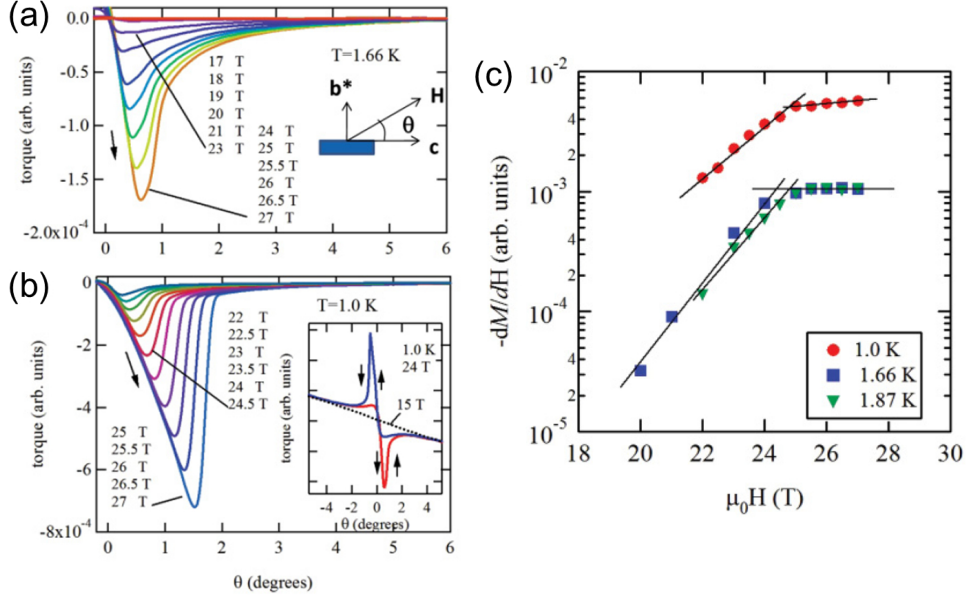+ K_4(x^2y^2 + y^2z^2 + x^2z^2)(x^2y^2z^2) + \cdots \quad (2.1)
\end{aligned}
$$

Figure 2.1: Magnetic torque measurements on the organic superconductor λ-(BETS)$_2$FeCl$_4$ [169]. (a) The field-angle θ dependence of the magnetic torque at 1.66 K. The inset shows the measurement setup.(b) θ dependence of the magnetic torque at 1.0 K. (c) The field dependence of $-dM_z/dH_z$.

The magnetic torque of Ho$_x$Tb$_{1-x}$Fe$_2$ was measured with a field of 1.76 T at room temperature. The field rotated within (110) surface of the crystal. The anisotropy energy is rewritten with the field angle θ by the transformation $x = \frac{1}{\sqrt{2}}\cos\theta, y = -\frac{1}{\sqrt{2}}\cos\theta, z = \sin\theta$. The measurements were performed on several samples with different compositions, revealing a shift of easy axis from [111] to [110], and [100] by substitution of Ho with Tb. The anisotropy coefficients K_i were determined by the fit of the torque with $-\frac{\partial E}{\partial \theta}$;

$$E = K_0 + \frac{K_1}{4}(\cos^4\theta + \sin^2 2\theta) + \frac{K_2}{4}\sin^2\theta\cos^4\theta + \frac{K_3}{16}(\cos^4\theta + \sin^2 2\theta)^2$$
$$+ \frac{K_4}{16}\sin^2\theta\cos^4\theta(\cos^4\theta + \sin^2 2\theta) + \cdots \quad (2.2)$$

The study also calculated the coefficients of cubic harmonics expansion [165]. The technique was also applied on hexagonal DyNi$_5$, in which the hexagonal c-axis is the hard axis, to study magnetocrystalline anisotropy in the basal hexagonal plane [166]. Later the technique was applied to paramagnetic TbAl$_2$ [167]. The study found a slight anisotropy arising from a second rank tensor susceptibility in the paramagnetic state [167]. A subsequent theoretical study formulated the reconstruction of the anisotropy free energy from the magnetic torque in the general case [168]. Those studies demonstrated the potential of magnetic torque for probing slight anisotropy arising from electrons.

Measuring magnetic torque is also an effective way to detect a phase transition since the torque is a thermodynamic quantity. Whereas magnetization is linear as a function of an external field in a paramagnetic state, magnetic torque is quadratic, enabling measurements of the susceptibility with the high resolution under the high field. Also, the measurement technique is much easier than other thermodynamic quantities, providing an

advantage in either ultra-low temperature or high field environments. Therefore, magnetic torque often probes a tiny anomaly resulting from a phase transition that is hardly probed by other thermodynamic quantities: magnetization, heat capacity, etc. A good example is a Fulde-Ferrell-Larkin-Ovchinnikov (FFLO) transition. FFLO superconductivity has been investigated at the low-temperature and high-field region of clean 2D superconductors in which the upper critical field H_{c2} exceeds the Pauli limit. References [170, 171] report torque measurements on an organic 2D superconductor κ-(BEDT-TTF)$_2$Cu(NCS)$_2$ with an in-plane magnetic field. A large anomaly is observed in the field dependence of the torque at H_{c2}, which exceeds the Pauli limit. An additional anomaly is observed just below the H_{c2} only at low temperature, corresponding to the Pauli limit in the phase diagram. The results suggest the presence of a distinct superconducting phase above the Pauli limit such as FFLO states. These techniques and discussions are also applied to a transition metal dichalcogenide NbS$_2$ [172].

A study on another 2D organic superconductor λ-(BETS)$_2$FeCl$_4$ reports the field-angular dependence of the torque [169]. The magnetic field rotated within the b^*c (zx) plane of the crystal, as shown in the inset of figure 2.1(a). θ is the angle from the c-axis. Figures 2.1(a,b) show the θ dependence of the torque at $1.66\,\mathrm{K}$, and $1.0\,\mathrm{K}$, respectively. The measured torque is $\tau_y = \mu_0(M_z H_x - M_x H_z) = \mu_0 H_x H_z(M_z/H_z - M_x/H_x)$. For highly 2D superconductors with a nearly parallel field to the plane, $\tau_y \fallingdotseq \mu_0 M_z H_x$ because $|M_z/H_z| \gg |M_x/H_x|$ when the in-plane field H_x is much larger than the in-plane lower critical field H_{c1} [173]; $\tau_y \fallingdotseq \mu_0 M_z H_x$. The H_z derivative of M_z is;

$$\frac{dM_z}{dH_z} \fallingdotseq \frac{d}{dH_z}\left(\frac{\tau_y}{\mu_0 H_x}\right) \tag{2.3}$$

$$= \left(\frac{dH_z}{d\theta}\right)^{-1}\frac{d}{d\theta}\left(\frac{\tau_y}{\mu_0 H_x}\right) \tag{2.4}$$

$$= -\frac{1}{\mu_0 H \cos\theta}\frac{d}{d\theta}\left(\frac{\tau_y}{H_x}\right) \tag{2.5}$$

The slope of τ_y/H_x is proportional to dM_z/dH_z at $\theta = 0$, which is a third-rank tensor susceptibility. The slope $d/d\theta(\tau_y/H_x) \propto -dM_z/dH_z$ at $\theta = 0$ is plotted as a function of $\mu_0 H$ in figure 2.1(c). $-dM_z/dH_z$ shows the kink inside the superconducting phase, which indicates an occurrence of a thermodynamic phase transition. The similar technique was applied to other FFLO candidates κ-(BEDT-TTF)$_2$Cu(NCS)$_2$ [174] and β-(BEDT-TTF)$_2$SF$_5$CH$_2$CF$_2$SO$_3$ [175].

2.1.2 Rotational symmetry breaking

As discussed in the previous section, magnetic torque is a thermodynamic quantity sensitive to phase transition and magnetic anisotropy of free energy. Therefore, torque measurements have been recently applied to detect phase transitions accompanied by rotational symmetry breaking. Here we first calculate a formula of magnetic torque in a tetragonal system and then introduce previous studies which observed nematic transitions by performing magnetic torque measurements. In a paramagnetic state, the leading order in magnetic free energy is the quadratic term $\chi_{ij}H_iH_j$. Here χ_{ij} is the second-rank magnetic susceptibility tensor, satisfying $M_i = \chi_{ij}H_j$. The matrix elements in χ_{ij} are restricted

by permutation symmetry and crystal symmetry [176, 177]. The permutation symmetry $\chi_{ij} = \chi_{ij}$ is given by the symmetry of second derivatives in the free energy. If the free energy is smooth enough as a function of the magnetic field,

$$\chi_{ij} = \frac{\partial^2 F}{\partial H_i \partial H_j} = \frac{\partial^2 F}{\partial H_j \partial H_i} = \chi_{ji} \tag{2.6}$$

The condition does not fold if, for example, a magnetic field-induced transition occurs. Furthermore, the matrix elements are limited by the symmetry of the crystal. Due to Neumann's principle that any physical properties must have the symmetry of the point group of the crystal, the tensor must be invariant to the symmetry operations of the point group; $\chi = U\chi U^{-1}$. U is the matrix representation of a symmetry operation such as rotation, inversion, and reflection.

In a crystal with C_4 symmetry, the susceptibility satisfies $\chi = C_4 \chi C_4^{-1}$. Assumed the C_4 rotation about the c-axis, $\chi_{aa} = \chi_{bb}$ and $\chi_{ab} = \chi_{ba} = \chi_{ac} = \chi_{ca} = \chi_{bc} = \chi_{cb} = 0$. The susceptibility tensor under the C_4 symmetry is,

$$\chi(C_4) = \begin{pmatrix} \chi_{aa} & 0 & 0 \\ 0 & \chi_{aa} & 0 \\ 0 & 0 & \chi_{cc} \end{pmatrix} \tag{2.7}$$

Next, we consider the case when rotational symmetry breaking occurs in a way $C_4 \to C_2$. The susceptibility under C_2 symmetry is,

$$\chi(C_2) = \begin{pmatrix} \chi_{aa} & \chi_{ab} & 0 \\ \chi_{ab} & \chi_{bb} & 0 \\ 0 & 0 & \chi_{cc} \end{pmatrix} \tag{2.8}$$

The symmetry reduction makes χ_{aa} and χ_{bb} unequal and introduces off-diagonal components χ_{ab}. Magnetic torque arising from $\chi(C_2)$ is,

$$\boldsymbol{\tau} = \mu_0 V \boldsymbol{M} \times \boldsymbol{H} \tag{2.9}$$

$$= \mu_0 V \begin{pmatrix} \chi_{aa} & \chi_{ab} & 0 \\ \chi_{ba} & \chi_{bb} & 0 \\ 0 & 0 & \chi_{cc} \end{pmatrix} \begin{pmatrix} H\sin\theta\cos\phi \\ H\sin\theta\sin\phi \\ H\cos\theta \end{pmatrix} \times \begin{pmatrix} H\sin\theta\cos\phi \\ H\sin\theta\sin\phi \\ H\cos\theta \end{pmatrix} \tag{2.10}$$

$$= \frac{1}{2}\mu_0 V H^2 \begin{pmatrix} \sin 2\theta(\chi_{ba}\cos\phi + \chi_{bb}\sin\phi - \chi_{cc}\sin\phi) \\ \sin 2\theta(\chi_{cc}\cos\phi - \chi_{aa}\cos\phi - \chi_{ab}\sin\phi) \\ (1 - \cos 2\theta)(\frac{\chi_{aa}-\chi_{bb}}{2}\sin 2\phi - 2\chi_{ab}\cos 2\phi) \end{pmatrix} \tag{2.11}$$

Here the magnetic field is expressed in polar coordinates. When the field is applied within the ab-plane ($\theta = \pi/2$), $\tau_a = \tau_b = 0$. Only τ_c is nonzero;

$$\tau_c = \frac{1}{2}\mu_0 V H^2 [(\chi_{aa} - \chi_{bb})\sin 2\phi - 2\chi_{ab}\cos 2\phi] \tag{2.12}$$

Without the rotational symmetry breaking, $\tau_c = 0$ since $\chi_{aa} = \chi_{bb}$ and $\chi_{ab} = 0$. However, when the C_4 symmetry is reduced to C_2, $\chi_{aa} \neq \chi_{bb}$ and/or $\chi_{ab} \neq 0$ is finite, inducing two-fold sinusoidal oscillation in τ_c as a function of the azimuthal field angle ϕ. Therefore, the rotational symmetry breaking can be detected as an appearance of two-fold oscillation
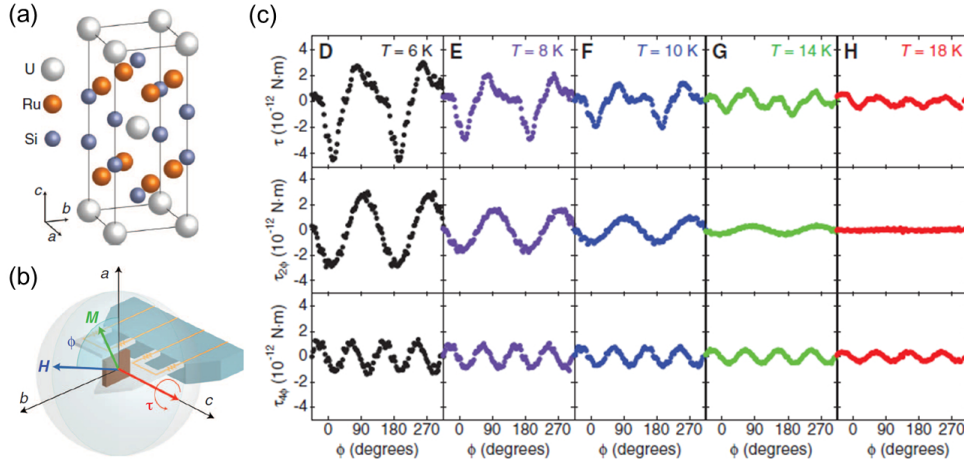
Figure 2.2: Magnetic torque measurements on URu_2Si_2 [178] (a) The crystal structure of URu_2Si_2. (b) The measurement setup. (c) The field-angle dependence of the magnetic torque. $\tau_{2\phi}$ ($\tau_{4\phi}$) is the two (four) -fold oscillations determined by the Fourier analysis.

in τ_c. In a system without any additional symmetries, both $\chi_{aa} - \chi_{bb}$ and χ_{ab} can be finite when C_4 is reduced to C_2. On the other hand, if the system has additional rotational or mirror symmetries, either $\chi_{aa} - \chi_{bb}$ or χ_{ab} is finite. For example, in a crystal of D_{4h} symmetry 5.3, the symmetry reduction $C_4 \to C_2$ occurs in two ways when the inversion symmetry is not broken: B_{1g} and B_{2g}. In the former case, only $\chi_{aa} - \chi_{bb}$ is finite, inducing two-fold sine oscillation in τ_c, whereas χ_{ab} is finite, inducing two-fold cosine oscillation in the latter case.

A good example of the application is the study on URu_2Si_2 [178, 179]. URu_2Si_2 is a heavy fermion compound that shows a superconducting transition at $T_c = 1.4\,\text{K}$. Another phase transition occurs at higher temperature $T_h = 17.5\,\text{K}$, accompanying a large jump of heat capacity [180]. The electronic state between T_c and T_h is called the hidden order because the order parameter and the mechanism are still elusive. The torque measurements were performed to understand the rotational symmetry of the order parameter. Figure 2.2(a) is the crystal structure of URu_2Si_2. The compound has tetragonal symmetry, which has a four-fold rotational symmetry about the c-axis. The field was applied within the ab-plane as shown in figure 2.2(b). The in-plane field induces magnetic torque $\boldsymbol{\tau} \parallel c$, which rotates the crystal about the c-axis. Thus, the leading order of the torque signal follows equation 2.12. The torque shows oscillating behavior as a function of the field angle ϕ as shown in figure 2.2(c). The oscillation is not a simple sinusoidal curve due to the presence of higher-order oscillations. The Fourier analysis was performed by fitting the oscillations with $\sum_n A_n \sin 2n\pi(\phi + \phi_n)/360$. The study reports that n-odd terms are absent and the leading orders are $n = 2$ and $n = 4$. $\tau_{2\phi} \equiv \tau - \sum_{n \neq 2} A_n \sin 2n\pi(\phi + \phi_n)/360$ and $\tau_{4\phi} \equiv \tau - \sum_{n \neq 4} A_n \sin 2n\pi(\phi + \phi_n)/360$ are plotted together with τ in figure 2.2(c). The appearance of the finite two-fold oscillation $\tau_{2\phi}$ below T_h indicates the rotational symmetry breaking from C_4 to C_2. The microscopic origin of $n = 4$ term is not discussed. $\tau_{2\phi} \approx A_{2\phi} \cos 2\phi$ demonstrates that $\chi_{ab} \neq 0$, and $\chi_{aa} = \chi_{bb}$. Furthermore, the field and temperature dependences of the two-fold oscillation provide information on the hidden order and its phase transition. Although equation 2.12 indicates $A_{2\phi} \propto H^2$, the field
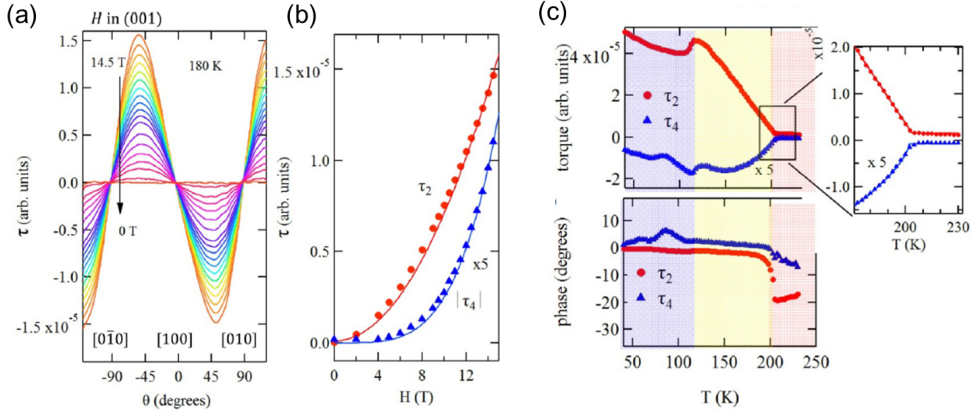
Figure 2.3: Torque measurements on $Cd_2Re_2O_7$ with the magnetic field in (001) surface [182]. (a) The field angle dependence of the magnetic torque at 180 K. (b) The field dependence of τ_2 and τ_4 at 180 K. (c) τ_2, τ_4, θ_2, and θ_4 at 14.5 T are plotted as a function of temperature.

dependence of $A_{2\phi}$ is not monotonic. This suggests that χ_{ab} is dependent on the field. The temperature dependence is superlinear; $\chi_{ab} \propto c(T_h - T) + c'(T_h - T)^2$. The leading order is the linear term. On the other hand, the standard mean-field theory expects the temperature dependence of the order parameter η is square-root $\eta \propto (T_h - T)^{1/2}$. The linear temperature dependence suggests, for example, that χ_{ab} comes from the second-order of the order parameter; $\chi_{ab} \propto \eta^2$. This study provides a lot of information on the hidden order transition and the symmetry of the order parameter.

This technique is also applied to an iron-based superconductor to study the orbital order which breaks the rotational symmetry [181]. Furthermore, a recent torque study revealed the rotational symmetry breaking in the pseudogap state of a high-T_c cuprate superconductor [94].

2.1.3   An odd parity order

It is important to experimentally determine the order parameter symmetry when revealing the microscopic mechanism of electronic orders. Magnetic torque measurements are effective not only for discussing rotational symmetry but also for inversion symmetry. The torque study on $Cd_2Re_2O_7$ [182] is a good example of the application to an odd-parity order. The compound shows a second-order phase transition at $T_{s1} \sim 200$ K with a symmetry reduction from the centrosymmetric cubic structure to the noncentrosymmetric tetragonal structure. The phase transition accompanies the displacement of oxygen ions. Despite the small displacement, the density of states drastically decreases, implying an electronic origin. Optical second harmonic generation (SHG) studies [183, 184] suggested the coexistence of two primary order parameters. However, the symmetry of those order parameters was controversial. This is because the odd-parity order coexists with the even-parity, but SHG is sensitive only to odd-parity order parameters. The magnetic torque measurements compensated for the insufficient information because torque is sensitive to even-parity order parameters.

Figures 2.3 show results of the torque measurements with the magnetic field in the (001) plane. Below T_{s1}, the torque shows both two-fold and four-fold oscillations as a function of the field angle. Figure 2.3(a) shows the field-angle θ dependence of the torque at $180\,\mathrm{K}$. The phase of the oscillations are almost field-independent. The torque curves are well fitted with the function $\tau(\theta) = \tau_2 \sin 2(\theta - \theta_2) + \tau_4 \sin 4(\theta - \theta_4)$ at all the fields. The field dependence of τ_2 and τ_4 is shown in Figure 2.3(b). The solid lines are the quadratic fit for τ_2 and the quartic one for τ_4.

The discussion is based on the expansion of the magnetic free energy with basis functions of the irreducible representations in the crystal point group O_h. The character table of the cubic point group O_h is shown in table 5.1. The irreducible representations are labeled with Mulliken symbols. A_{1g} is the symmetry equivalent to O_h. A, E, and T represent one-, two-, and three-dimensional subgroups, respectively. g/u is an index for even/odd-parity subgroups. The coupling terms between the magnetic field and the order parameter are expanded with the basis functions, which are listed in table 5.2.

$$F_{mag} = \sum_{\Gamma \in O_h} a_2^{\Gamma} h^{\Gamma}(\boldsymbol{\eta}) f_2^{\Gamma}(\boldsymbol{H}) + a_4^{\Gamma} k^{\Gamma}(\boldsymbol{\eta}) f_4^{\Gamma}(\boldsymbol{H}) \tag{2.13}$$

The free energy includes only the quadratic and quartic function of the field (f_2 and f_4), since the torque signal consists of $\tau_2 \propto H^2$ and $\tau_4 \propto H^4$. Γ is an irreducible representation of O_h group. h^{Γ} and k^{Γ} are functions of the order parameter $\boldsymbol{\eta}$ which have the symmetry Γ. h/k and f of the same symmetry couple together so that the free energy can preserve the crystal symmetry. a_2^{Γ} and a_4^{Γ} are coupling constants. As shown in figure 2.3(c), $\theta_2 \approx 0°$; $\tau_2 \propto \sin 2\theta$. The magnetic torque arises from the free energy $\propto \cos 2\theta$ since the torque is calculated by $\tau = -\frac{\partial F}{\partial \theta}$. The in-plane field $\boldsymbol{H} = (H\cos\theta, H\sin\theta, 0)$ gives the quadratic functions of the field $f_2^{A_{1g}}(\boldsymbol{H}) = H^2$, $f_2^{E_g}(\boldsymbol{H}) = \{-H^2, H^2\cos 2\theta\}$, and $f_2^{T_{2g}}(\boldsymbol{H}) = \{0, 0, \frac{1}{2}H^2\sin 2\theta\}$. Only $f_2^{E_g}$ is consistent with the observed τ_2. In the same way, the four-fold oscillation $\tau_4 \propto \sin 4\theta$ indicates the contribution of $f_4^{A_{1g}}(\boldsymbol{H})$ or $f_4^{E_g}(\boldsymbol{H})$ in the free energy. $f_4^{A_{1g}}(\boldsymbol{H})$ is eliminated by the same measurement and analysis with the field in the $(1\bar{1}0)$ plane. Thus, the field-angle dependence of the torque determines the free energy,

$$F_{mag} = a_2 h^{E_g}(\boldsymbol{\eta}) f_2^{E_g}(\boldsymbol{H}) + a_4 k^{E_g}(\boldsymbol{\eta}) f_4^{E_g}(\boldsymbol{H}) \tag{2.14}$$

The temperature dependence provides further information on $h^{E_g}(\boldsymbol{\eta})$ and $k^{E_g}(\boldsymbol{\eta})$. Figure 2.3(c) demonstrates $\tau_4 \propto (T_{s1} - T)^{1/2}$, suggesting that $k^{E_g}(\boldsymbol{\eta})$ is a linear function of a mean-field order parameter η_{E_g} which has E_g symmetry. On the other hand, $\tau_2 \propto T_{s1} - T$ suggests that $h^{E_g}(\boldsymbol{\eta})$ is a quadratic function of the order parameter. Since the crystal symmetry is reduced to E_u by the structural transition at T_{s1}, the order parameter is likely to belong to E_u; η_{E_u}. Because $E_u \otimes E_u = A_{1g} \oplus A_{2g} \oplus E_g$, quadratic functions of η_{E_u} can have the symmetry E_g. In this manner, the coexistence of an odd-parity and even-parity order parameters was demonstrated by the comprehensive discussion of temperature, field, and the field-angle dependence of the magnetic torque.

2.2 Torque measurements by piezoresistive microcantilevers

To measure the magnetic torque of a tiny crystal $\sim 100\,\mu\mathrm{m}$, we used a technique with piezoresistive microcantilevers. A microcantilever was firstly utilized for the magnetic
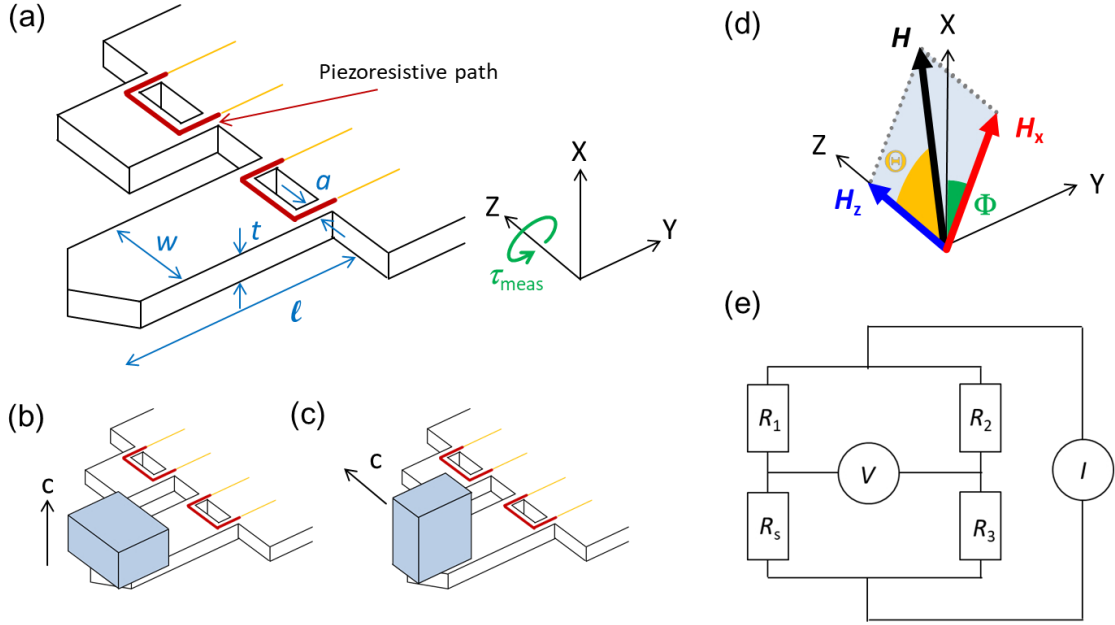
Figure 2.4: (a) A schematic of a cantilever PRC120/400, SEIKO instruments. XYZ is the coordinate of the cantilever, which rotates with respect to the xyz coordinate of the superconducting magnets. (b) The sample alignment in the out-of-plane anisotropy measurements, and (c) in the in-plane anisotropy measurements. (d) The orientation of the magnetic field. (d) The Wheatstone bridge.

torque measurements more than fifty years ago [185]. Currently, the technique is one of the most popular ones among torque measurement techniques used in condensed matter physics because of its ease to use in ultrahigh vacuum and at low temperatures. Although the technique is not applied to ultralow temperature measurements due to the Joule heating in a piezo resistor ($\sim 10^{-5}$ J/s when $I = 300\,\mu$A is applied), the heating scarcely increases the sample temperature in a range of temperature where we measured the torque $\sim$ 10–300 K.

We used a commercial microcantilever for atomic force microscopy (PRC120 and PRC400, SEIKO instruments). The technique using the cantilever was established by E. Ohmichi [186]. The cantilever consists of a 120/400 μm cantilever (PRC120/400) and a shorter reference lever as shown in Figure 2.4(a). The lever size of PRC120 is $l = 120\,\mu$m, $w = 50\,\mu$m, and $t = 5\,\mu$m. Only the length is different in PRC400; $l = 400\,\mu$m. The deflection of the lever is detected by the piezoresistive path made of p-doped silicon (red thick line) at the base of the lever. Since the lever moves within XY-plane, only the torque along the Z-axis (rotation about the Z-axis) is detected as a change in the resistance of the piezo resistor.

A sample was fixed on a longer lever with commercially available instant adhesive. When measuring the out-of-plane anisotropy of the magnetic torque, the sample was mounted on a lever so that $c \parallel X$ as shown in Figure 2.4(b). On the other hand, $c \parallel Z$ in the in-plane anisotropy measurements as shown in Figure 2.4(c). We applied the magnetic field of 4 T in the normal state measurements but reduced it to 1.5 T in the superconducting state to prevent the damage on the lever by the large superconducting

diamagnetism. The magnetic field $\boldsymbol{H}$ within the XY-plane induces the torque along the Z-axis. In the measurements on Hg1201, the field was also applied in a tilted plane using two superconducting magnets due to the large misalignment (discussed in 3.2.3). We applied $\boldsymbol{H_x}$ within the XY-plane by a split coil and $\boldsymbol{H_z}$ along the Z-axis by a solenoid coil as shown in Figures 2.4(d). $\boldsymbol{H} = \boldsymbol{H_x} + \boldsymbol{H_z}$ makes an angle Θ from the Z-axis. Here XYZ labels the coordinates of the lever, and xyz labels that of the magnets. Whereas $Z \parallel z$, the XY-plane rotates with respect to the xy-plane by a mechanical rotator. Φ is the rotation angle.

Reference [186] provides the formula of the relation between the torque τ and the resistance of the piezo resistor.

$$\frac{\Delta R}{R_s} = \pi_L \frac{6\tau}{2at^2} \tag{2.15}$$

Here a is the neck width of the lever as shown in Figure 2.4(a). $\pi_L \sim 4.5 \times 10^{-10}\,\mathrm{m^2/N}$ is the longitudinal piezoresistive coefficient for Si in the [100] direction. R_s is the resistance of the piezo resistor on the lever at zero fields, and ΔR is a small displacement from R_s when the magnetic field is applied, inducing the magnetic torque. To measure the small ΔR with high resolution, we prepared the Wheatstone as shown in Figure 2.4(e). R_1 is the piezo resistor of the reference lever. To complete the bridge, we used another pair of levers without mounting sample, the resistances of which are R_2 and R_3. The bridge is well balanced, since $R_s \fallingdotseq R_1 \fallingdotseq R_2 \fallingdotseq R_3 \fallingdotseq R$. When the finite torque changes the resistance, $R_s = R \rightarrow R + \Delta R$ ($\Delta R \ll R$), the voltage V changes by $\Delta V \approx \Delta RI/4$. Therefore, the torque is calculated by

$$\tau = \frac{2at^2}{3\pi_L} \frac{4}{IR_s} \Delta V \tag{2.16}$$

We applied the current $I = 300\,\mu\mathrm{A}$ in the measurements.

Figure 2.5 shows a schematic of the measurement setup. We used vector magnets consisting of a split coil and a solenoid coil, which were placed in a reservoir filled with liquid Helium. To increase the sample temperature up to room temperature, we inserted the variable temperature insert (VTI) in a reservoir. The VTI did not have any thermometers or heaters. We pumped up the gas inside with a diaphragm pump to inlet the liquid Helium from the reservoir through a needle valve. We controlled the VTI temperature by tuning a manual needle valve and a manual flow controller. To stabilize the VTI temperature, we left the system for more than half a day after the tuning before starting the measurements. The needle valve was closed in the measurements above $\sim 200\,\mathrm{K}$. In the VTI, we inserted a probe with a vacuum-can (v-can). The v-can was filled with exchange gas (^{4}He, $0-10\,\mathrm{mbar}$). The copper block was placed at the end of the probe and located at the center of the magnets. On the copper block, we attached a Cernox thermometer to monitor the base temperature, a carbon chip resistor $\sim 400\,\Omega$ to heat the base, and the piezoresistive microcantilevers to measure the torque. The cantilevers were attached to the copper block so that $Z \parallel z$ as shown in Figures 2.4. The impedance of the Wheatstone bridge was measured by the Delta mode using a nanovoltmeter (6221, KEITHLEY) and a current source (2182A, KEITHLEY). The instruments communicate with each other through RS-232 and a trigger link. The resistance of the base thermometer was monitored by a temperature controller (Lake Shore 336). The controller was also
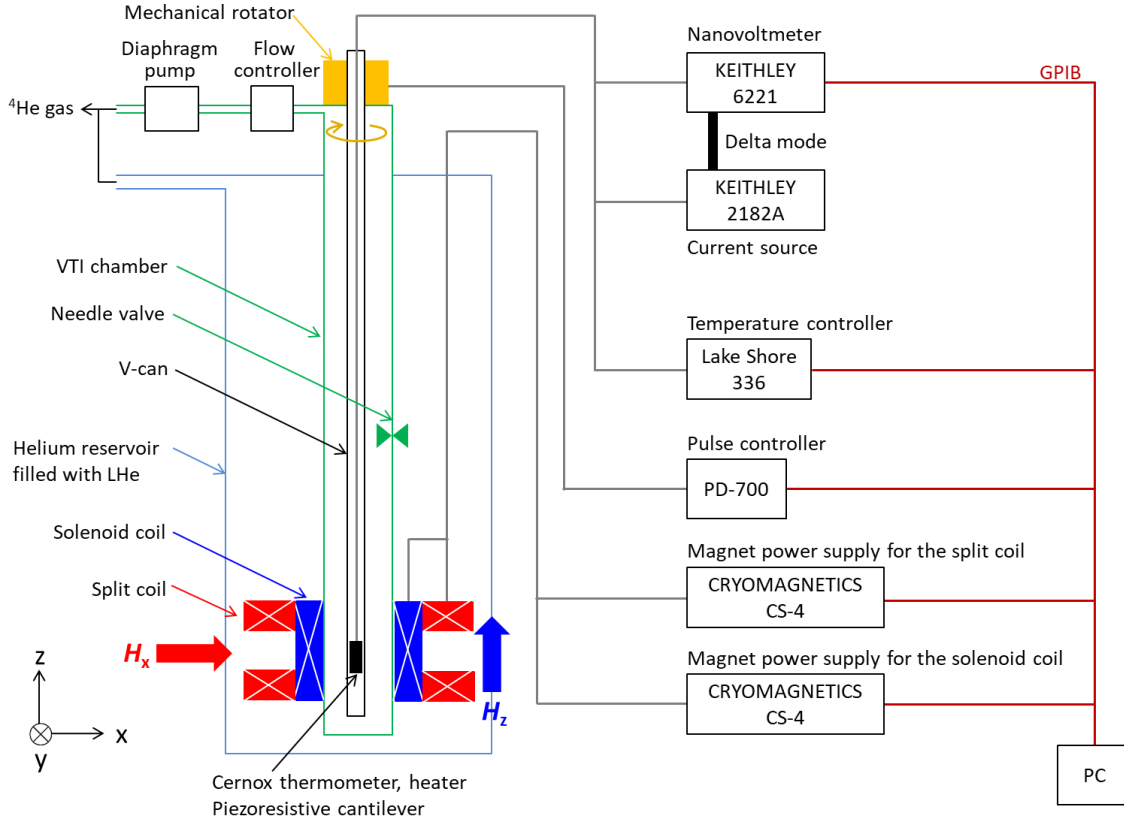
Figure 2.5: A schematic of the measurement setup.

used to output the heater current. To rotate the field with respect to the sample plane, we rotated the probe with the mechanical rotator. The rotator was controlled with a pulse controller (PD700, NIKKA DENSOK LIMITED). The superconducting coils were charged with magnet power supplies (CS-4, CRYOMAGNETICS). The upper limit of the field was $4\,\mathrm{T}$ for the split coil and $2\,\mathrm{T}$ for the solenoid coil.

We monitored and controlled the instruments by GPIB communication using Labview software. All the measurements were automatized with a program shown in Figure 2.9. The program consists of three parts. One is a loop for monitoring the voltage of the cantilever. Another is a loop for controlling the temperature. We read the base temperature, computed the PID parameter, and output the heater current. The main part is the measurement sequence. In Figure 2.9, we show two types of sequence: Φ-scan and Θ-scan. The Φ-scan was used for the torque measurements of the in-plane and the out-of-plane anisotropy. The Θ-scan was used for the misalignment detection on Hg1201. In the Φ-scan, we left the system for 0.5-2 hours after changing the target temperature of the base temperature. Since the VTI did not have a heater, the base heater heated the VTI through the exchange gas in the probe. Due to the large volume of the VTI, it takes a long time to stabilize the temperature of the whole system.
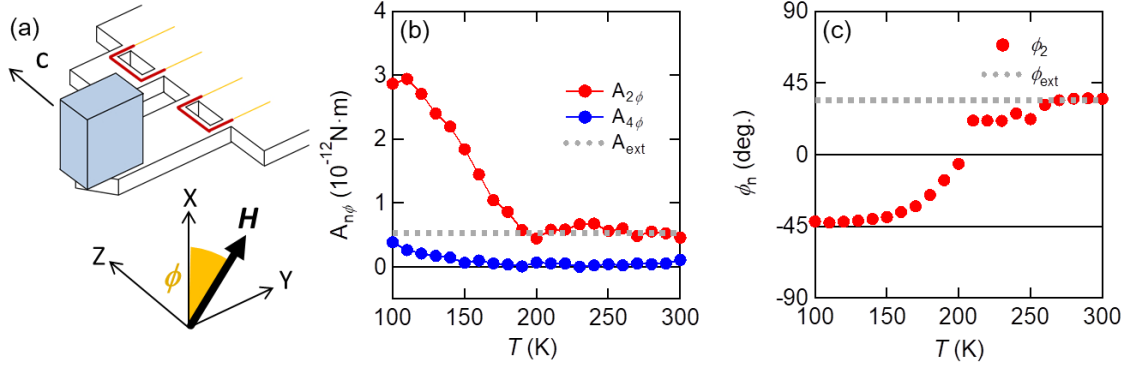
Figure 2.6: (a) The sample alignment in the in-plane magnetic torque measurements on $Sr_2Ir_{1-x}Rh_xO_4$ ($x = 0.095$). (b) Temperature dependence of the amplitude of the two-fold oscillation $A_{2\phi}$ (red circles) and four-fold oscillation $A_{4\phi}$ (blue circles). The gray dotted line indicates the amplitude of the extrinsic two-fold oscillation A_{ext}. (c) Temperature dependence of the phase for the two-fold oscillation ϕ_2. The gray dotted line indicates the phase of the extrinsic two-fold oscillation ϕ_{ext}.

2.3   Treatment of background signal

In this section, we discuss treatment of the background signal, which possibly arises from the anisotropic magnetoresistance of the piezoresistor itself. Here we use data that are discussed in later chapters. Figures 2.6 show raw data in the in-plane magnetic torque measurements on $Sr_2Ir_{1-x}Rh_xO_4$ ($x = 0.095$). In the measurements, the crystal was mounted on a cantilever so that the c-axis was parallel to the Z-axis as shown in Figure 2.6(a). The sample misalignment was very small because the sample was a plate-like shape, the largest facet of which was normal to the c-axis. The a/b-axis was away from the X/Y-axis. The field was applied within the XY-plane, which is parallel to the ab-plane. Since the crystal has tetragonal symmetry, $\tau_a = \tau_b = 0$, and only τ_c can be finite. Equation 2.12 indicates the absence of the field-angle dependence in a paramagnetic state of the tetragonal system. However, the finite two-fold oscillation was observed as a function of the field angle ϕ even at room temperature. We fitted the data with sinusoidal curves $\sum_{n=0}^{8} A_n \sin 2\pi(\phi - \phi_n)/360$. The temperature dependence of A_2 and A_4 is shown in figure 2.6(b). A_2 develops at low temperature with a clear kink at $\sim 200\,\mathrm{K}$. On the other hand, finite A_2 still exists above $200\,\mathrm{K}$, and it is almost temperature independent. The similar temperature dependence was also observed in ϕ_2 as shown in 2.6(c). We regarded the temperature-independent two-fold oscillation above $200\,\mathrm{K}$ as an extrinsic signal arising from the anisotropic magnetoresistance of the piezoresistor. We averaged A_2 and ϕ_2 above $250\,\mathrm{K}$, which is much higher than the onset temperature of the intrinsic signal. The average values, A_{ext} and ϕ_{ext}, are indicated with dotted lines in figures 2.6(b,c). We subtracted the extrinsic signal $\tau_{ext} = A_{ext} \sin 2\pi(\phi - \phi_{ext})/360$ from the raw data to discuss only the intrinsic signal. A_{ext} and ϕ_{ext} were different among cantilevers.

In contrast to the crystal of $Sr_2Ir_{1-x}Rh_xO_4$, the crystal facets of $HgBa_2CuO_{4+\delta}$ were off the high-symmetry axes as shown in Figure 2.7(a). We usually had a large misalignment ~ 10–$20°$. The details for the misalignment detection are discussed in the next chapter.
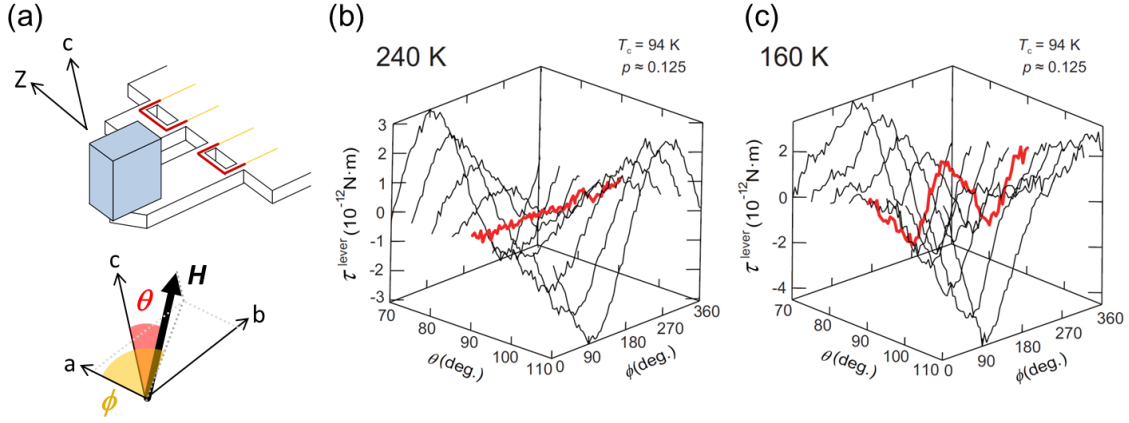
Figure 2.7: (a) The sample alignment in the in-plane magnetic torque measurements on HgBa$_2$CuO$_{4+\delta}$. (b) The field angle dependence of the torque τ^{lever} at 240 K [187] and (c) at 160 K for $p \approx 0.125$ [187]. The background two-fold oscillation is subtracted.

Figures 2.7(b,c) show the field-angle dependence of the magnetic torque of HgBa$_2$CuO$_{4+\delta}$ $p \approx 0.125$. The field angle was measured from the crystal axes. In the figures, the extrinsic two-fold oscillation is already subtracted. The red line indicates the torque when the field rotates within the ab-plane. At 240 K, the torque is independent of the field angle ϕ when $\theta = 90°$, whereas the finite field-angle dependence appears when the field is applied off the ab-plane. When the field is off the ab-plane, τ_a and τ_b are nonzero due to the out-of-plane anisotropy in the magnetic susceptibility (Equation 2.11). On the other hand, at 160 K, the finite two-fold oscillation appears when $\theta = 90°$.

The field-angle dependence of the toque at 240 K, 180 K, and 160 K is shown in figures 2.8(a–c). The extrinsic two-fold oscillation is subtracted in the figures. Without the intrinsic in-plane anisotropy, the pattern of the color plot has the inversion center at $(\theta, \phi) = (90°, 180°)$ as shown in figure 2.8(a). On the other hand, the inversion center is lost when the intrinsic in-plane anisotropy appears. Figures 2.8(d–f) show the calculation of the torque response. They were calculated by using the experimentally determined χ_{ab} and $\chi_{cc} - \chi_{aa}$. The calculation is consistent with the measured one. Figure 2.8(g) shows the calculation of the torque response when the field is applied within a plane tilted away from the ab-plane of crystal. In the calculation, we assumed the case that the field plane is tilted by 5°, $\theta' = (\theta - 5°) \cos(\phi - 20°)$, for example. The field-angle dependence is different from figures 2.8(a–c). Therefore, the symmetric pattern in figure 2.8(a) indicates that the field was precisely applied within the ab-plane of the sample in those measurements.
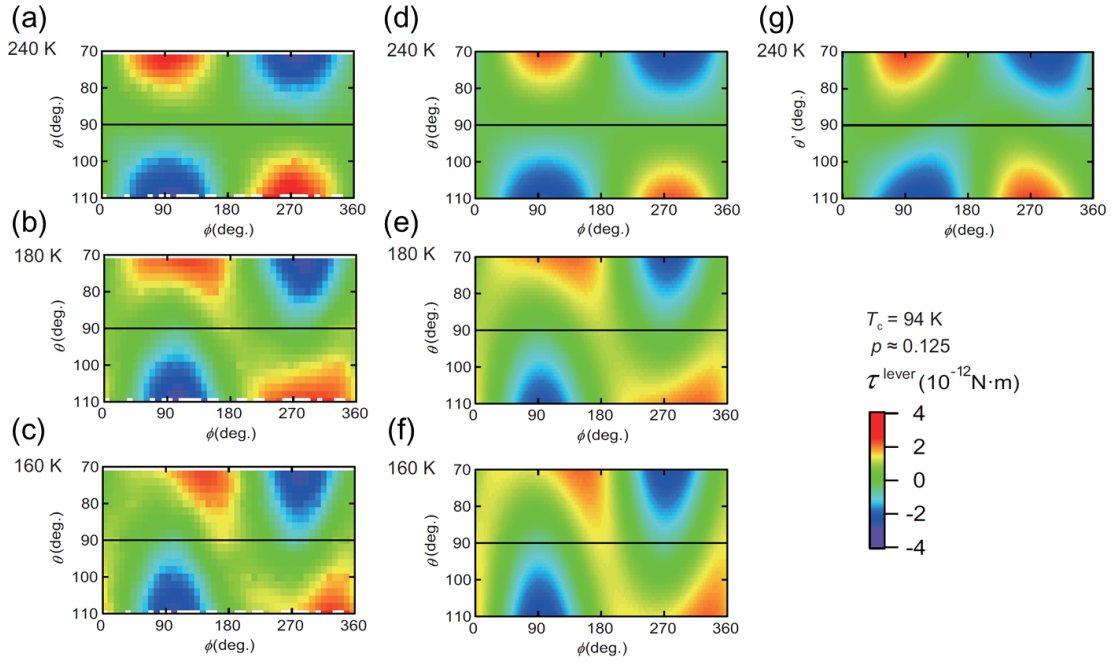
Figure 2.8: (a-c) The field-angle dependence of the measured magnetic torque for $p \approx 0.125$ at 240 K, 180 K, and 160 K. The extrinsic two-fold oscillation is subtracted [187]. (d-f) The calculation of the toque response at 240 K, 180 K, and 160 K [187]. The experimentally determined χ_{ab} and $\chi_{cc} - \chi_{aa}$ were used for the calculation. (g) The simulated torque response with the misalignment $\theta' = (\theta - 5°)\cos(\phi - 20°)$ [187].
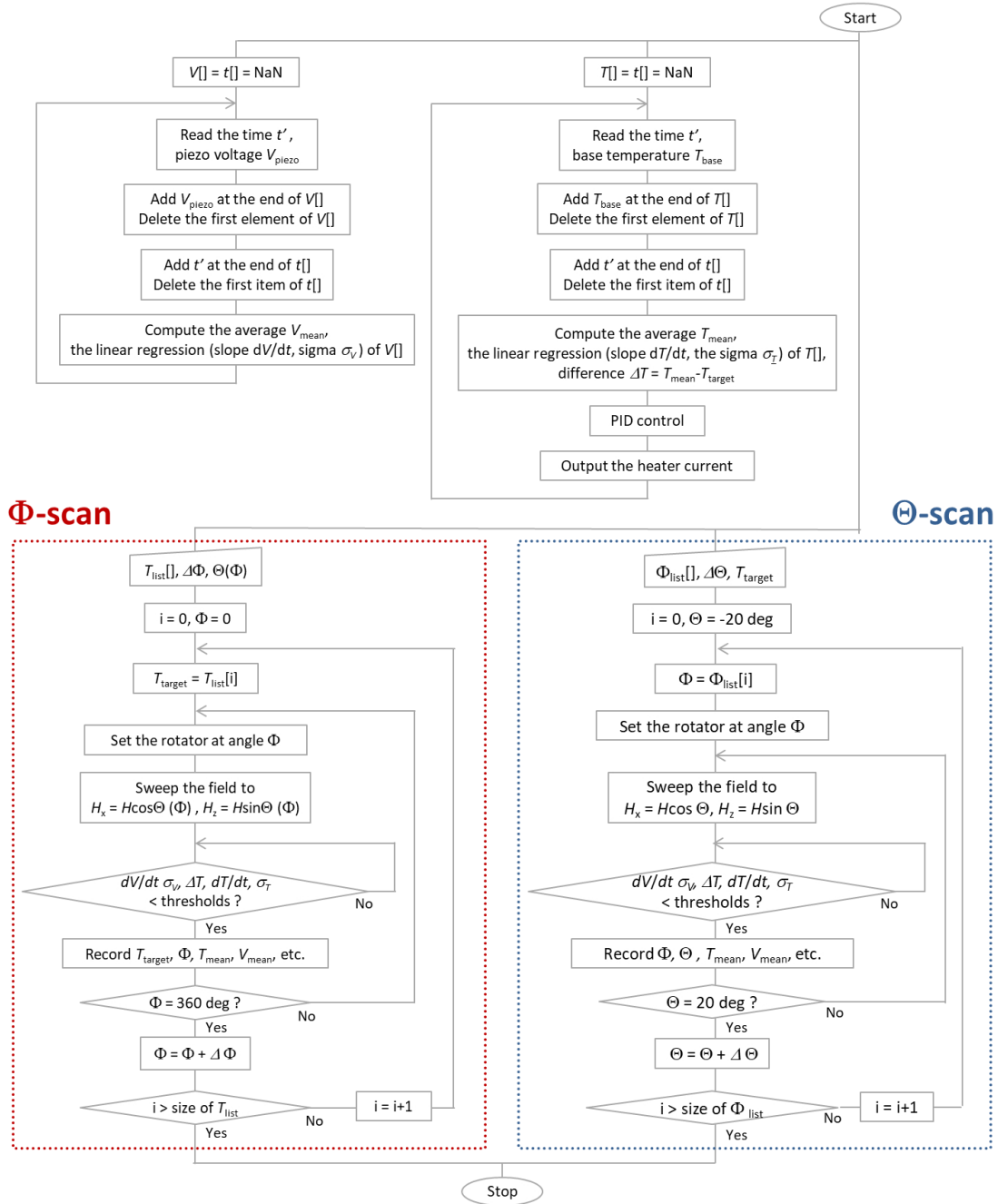
Figure 2.9: A flow chart of the program for the torque measurements.

Chapter 3

Diagonal nematicity in the pseudogap phase of HgBa$_2$CuO$_{4+\delta}$

In the history of high-T_c cuprate superconductors, it has been a controversial issue if the pseudogap formation is a phase transition or a cross-over phenomenon. Recently, various types of symmetry breaking were reported in the pseudogap state, suggesting the presence of an electronic order, but the phase transition was not observed at the pseudogap onset temperature in thermodynamic quantities. A recent torque study on YBa$_2$Cu$_3$O$_{6+\delta}$ (YBCO) implies that a nematic phase transition occurs at the pseudogap onset temperature. However, the rotational symmetry is already broken in the normal state due to its orthorhombicity, which can act as an external field to nematic orders. It is unclear if the nematic ordering spontaneously occurs in other cuprates. To verify the spontaneous rotational symmetry breaking, the measurements in a tetragonal system are necessary. HgBa$_2$CuO$_{4+\delta}$ (Hg1201) is one of the cuprates with a simple tetragonal crystal structure. In this chapter, we firstly introduce the basic properties and the phase diagram of Hg1201. Next, we report the magnetic torque measurements on Hg1201 and comprehensively discuss the nematic order in the pseudogap phase of high-T_c cuprate superconductors.

3.1 Phase diagram of HgBa$_2$CuO$_{4+\delta}$

3.1.1 Superconductivity and pseudogap formation

HgBa$_2$Ca$_{n-1}$Cu$_n$O$_{2n+2+\delta}$ ($n = 1, 2, 3$) is a cuprate family, one of which holds the world record of superconducting critical temperature T_c at ambient pressure [192]. Among the family, $n = 1$ case (Hg1201) has the simplest crystal structure. As shown in figure 3.1(a), this compound does not have a complex structure such as CuO chain in YBCO, which reduces the rotational symmetry about the c-axis from C_4 to C_2. In Hg1201, Ba acts as a spacer and extends the distance between Cu and the in-plane oxygen ~ 1.94 Å. The distance between Cu and the apical oxygen ~ 2.79 Å is relatively longer than that in other cuprates. Also, the material has a very flat CuO$_2$ plane. The flatness of the CuO$_2$ plane has been considered to influence superconductivity. Because of the very simple tetragonal crystal structure, Hg1201 is called a model compound of the high-T_c cuprate superconductors. The compound is suitable for studying electronic states intrinsic to the
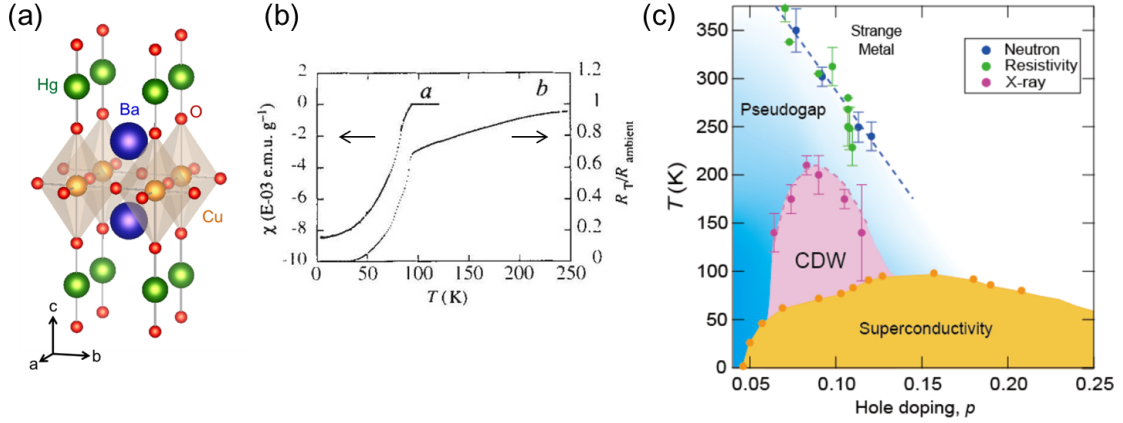
Figure 3.1: (a) The crystal structure of Hg1201. (b) The first report of the superconductivity in Hg1201 [188]. The magnetic susceptibility and the normalized resistivity are plotted together. (c) The phase diagram of Hg1201. The superconducting dome (yellow area) is determined by the onset temperatures of the superconducting diamagnetic response (orange circles) [189]. The pseudogap onset temperatures are determined by resistivity measurements [19] (green circles) and neutron scattering measurements (blue circles) [84, 190]. The CDW onset temperatures are determined by X-ray measurements (purple circles) [73, 191].

CuO$_2$ square lattice. By tuning the hole concentration with oxygen doping, Hg1201 shows the superconductivity at $T_c \sim 95$ K in the optimal doping [188]. Figure 3.1(b) shows the magnetic susceptibility and the normalized resistivity which were presented in the first report of the compound.

Figure 3.1(c) shows the phase diagram of the compound. The superconducting dome (yellow area) is determined by the onset temperatures of the superconducting diamagnetic response in the magnetic susceptibility [189]. The dome is suppressed around $p = 0.10$. The suppression is universally observed in the hole-doped cuprates, which is associated with the competing relation between the charge-density-wave (CDW) state and the superconducting state [65, 74]. In many high-T_c cuprate superconductors, the antiferromagnetic Mott insulating state appears at the half-filling state $p = 0$. However, we do not show the Mott phase in the phase diagram of Hg1201 because any previous studies do not report an occurrence of the Mott-transition or a presence of the antiferromagnetic order in underdoped Hg1201.

In Hg1201, the strange metal state is also identified by T-linear resistivity [19, 52, 84, 194]. The temperature dependence of the normalized resistivity $\rho/\rho(400\,\text{K})$ for an underdoped sample ($T_c \approx 80$ K) is shown in figure 3.2(a) [19]. The residual resistivity is very small compared to other cuprates. The T-linear resistivity $\rho \propto T$ is observed above $T^* \approx 280$ K. The change of the slope from T-linear is also observed in the underdoped region among a wide variety of the hole-doped cuprates [19]. It is widely accepted among the hole-doped cuprates that T^* is consistent with the pseudogap onset temperature. Also in Hg1201, we define the boundary between the strange metal and the pseudogap state by T^* as shown in figure 3.1(c) with the green circles. In addition to the resistivity, the pseudogap opening above T_c is suggested by several measurements [194–196], but Hg1201
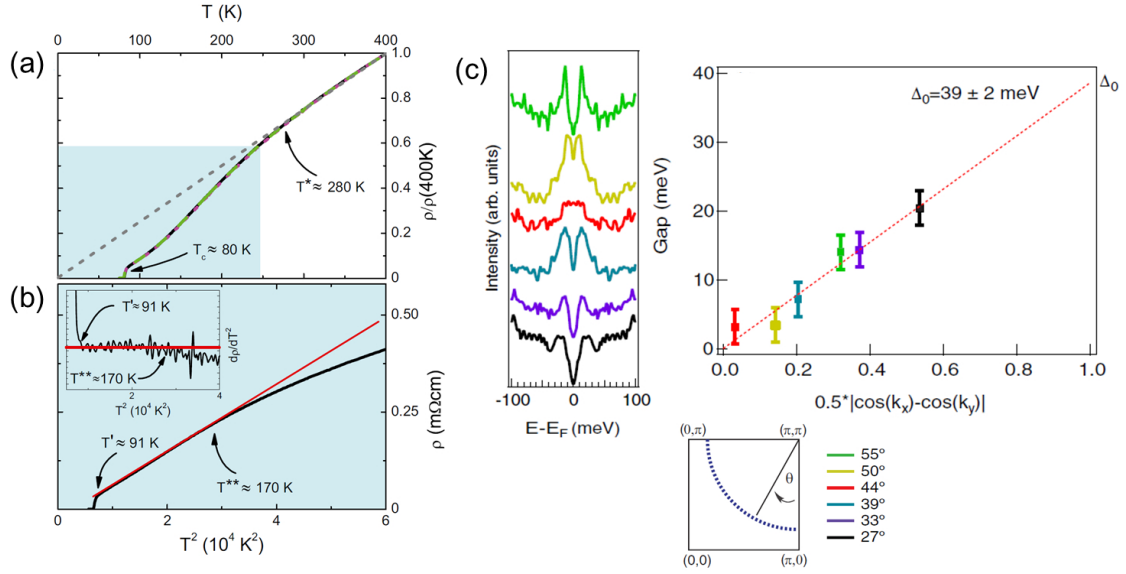
Figure 3.2: (a) The temperature dependence of the normalized resistivity $\rho/\rho(400\,K)$ for an under doped sample $T_c \approx 80\,\mathrm{K}$ [19]. T^* marks the temperature where the resistivity deviates from the T-linear extrapolation. T_c marks the midpoint of the resistive transition. (b) ρ is plotted as a function of T^2. T^{**} and T' are respectively the onset and offset temperature of quadratic resistivity. (c) Energy distribution curves in the ARPES measurements [193]. The background is subtracted. The angles label the momentum at which the curves are taken.

still lacks the direct observation of the Fermi arcs. The direct measurements of the Fermi surface, such as scanning tunneling microscopy (STM) and angle-resolved photoemission spectroscopy (ARPES), are not so much reported on Hg1201 owing to the absence of a charge-neutral cleavage plane.

In figure 3.2(b), the resistivity is plotted as a function of T^2. The Fermi-liquid-like resistivity $\rho \propto T^2$ is observed below $T^{**} \approx 170\,K$. The Fermi liquid behavior in the pseudogap state is also observed in the optical conductivity [195] and magnetoresistance [52]. Kohler's rule is satisfied in the pseudogap state of Hg1201 [52], whereas it is violated in La$_{2-x}$Sr$_x$CuO$_4$ (LSCO) and YBCO [197–199].

The superconducting gap was observed in tunneling spectroscopy measurements on the polycrystalline sample [200]. The V-shaped gap in dI/dV was well fitted by assuming a d-wave gap. The node of the superconducting gap is observed by the ARPES studies [193]. The left panel of figure 3.2(c) shows the symmetrized energy distribution curves at $10\,K$ on a nearly optimally doped sample ($T_c = 95\,K$). The background is subtracted from the curves. The curves are taken on k_F at various momentum as labeled. The estimated gap size is plotted as a function of the simple d-wave form, $0.5|\cos k_x - \cos k_y|$, as shown in the right panel. Extrapolation to $0.5|\cos k_x - \cos k_y| = 1$ (red dotted line) suggests the maximum gap $\sim 39 \pm 2\,\mathrm{meV}$, which is consistent with the gap size estimated by other measurements [200, 201].
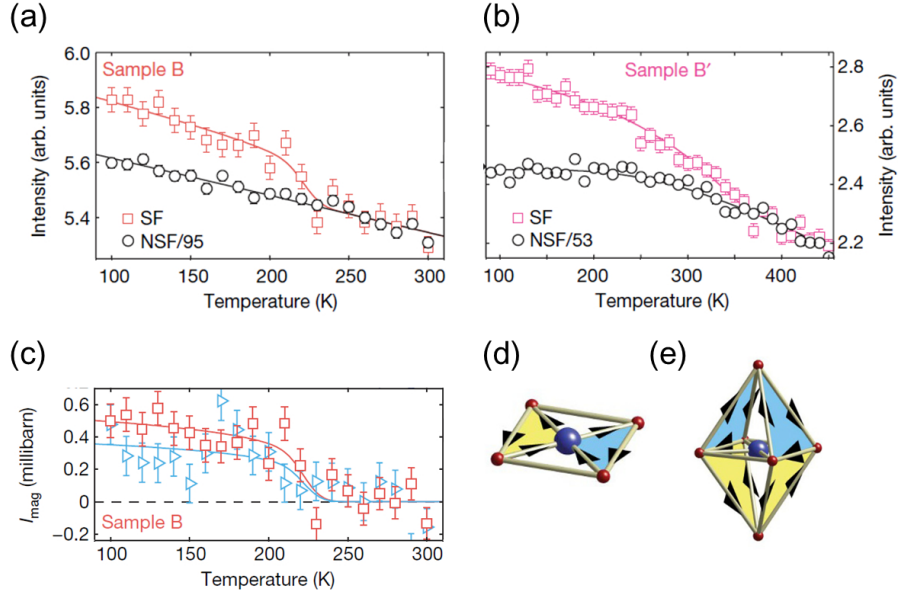
Figure 3.3: The spin-polarized neutron scattering measurements on Hg1201 [84]. (a) The scattering intensities at the Bragg peak $\boldsymbol{Q} = (1, 0, 1)$ are plotted as a function of temperature for sample B ($T_c = 81\,\mathrm{K}$) and (b) sample B' ($T_c = 61\,\mathrm{K}$). Red square and black circles represent spin-flip (SF) and the background (NSF/95) intensities, respectively. The spin polarization $\boldsymbol{P}$ is parallel to $\boldsymbol{Q}$. (c) The difference between the SF and the background intensities at the Bragg peak $\boldsymbol{Q} = (1, 0, 1)$ in sample B is plotted as a function of temperature. Red squares and blue triangles represent $\boldsymbol{P} \parallel \boldsymbol{Q}$ and $\boldsymbol{P} \perp \boldsymbol{Q}$, respectively. (d) Schematics of an in-plane loop current pattern and (e) a loop current pattern involving apical oxygen.

3.1.2   Time-reversal symmetry breaking in the pseudogap state

The time-reversal symmetry breaking has been investigated in the pseudogap state of the hole-doped cuprates after the circular dichroism was observed in the pseudogap state of Bi-2212 [83]. The first finding in Hg1201 was provided by the spin-polarized neutron scattering measurements [84]. Figure 3.3(a) shows the temperature dependences of the spin-flip (SF) scattering intensity (red squares) at the Bragg peak $\boldsymbol{Q} = (1, 0, 1)$ in sample B ($T_c = 81\,\mathrm{K}$). The normalized non-spin-flip (NSF) scattering intensity is also plotted with black circles. The spin polarization $\boldsymbol{P}$ was parallel to $\boldsymbol{Q}$, and $\boldsymbol{P}$ was in the scattering plane. Above 250 K, the SF intensity shows the same temperature dependence as the NSF intensity. The SF intensity arises from the nuclear Bragg scattering due to the imperfect polarization of the nuclear spin. The normalization factor 95 was determined so that the NSF intensity corresponds to the SF one above 250 K. On the other hand, below 250 K, the SF intensity deviates from the NSF one, indicating an appearance of intrinsic scattering in the SF channel. Therefore, the time-reversal symmetry is broken below 250 K.

After the measurement, sample B was annealed to reduce the oxygen content. The annealed one, sample B', shows lower critical temperature $T_c \sim 61\,K$. Figure 3.3(b) shows the temperature dependence of SF and the background (NSF/53) intensities. Here $\boldsymbol{P} \parallel \boldsymbol{Q}$ and $\boldsymbol{Q} = (1, 0, 1)$. The additional SF intensity also appears in sample B', but the

onset temperature is higher than sample B due to the reduced hole concentration. The onset temperatures are plotted in the phase diagram (Figure 3.1c) with the blue circles together with the temperatures reported in Ref. [190]. The temperatures are consistent with the pseudogap onset temperatures determined in the resistivity measurements [19]. This suggests that the time-reversal symmetry breaking occurs when the pseudogap opens. The observations are qualitatively and quantitatively consistent with YBCO.

The origin of the time-reversal symmetry breaking has been attributed to a loop current order [86, 202]. Figure 3.1(d) shows a pattern of the loop currents which has been mostly discussed. The loop currents flow within the ab-plane, inducing the magnetic moments perpendicular to the plane. However, the polarization dependence of the SF intensity suggests that the scattering moment is not polarized along the c-axis. Figure 3.3(c) shows the temperature dependence of the difference between the SF and the background intensities in sample B. The red squares represent the difference when $\boldsymbol{P} \parallel \boldsymbol{Q}$, which is also shown in figure 3.1(a). On the other hand, the blue triangles represent the difference when the polarization is different by 90° $\boldsymbol{P} \perp \boldsymbol{Q}$ ($\boldsymbol{P}$ is in the scattering plane). When $\boldsymbol{P} \perp \boldsymbol{Q}$, the additional SF intensity is reduced by $\sim 35\%$ compared to the case of $\boldsymbol{P} \parallel \boldsymbol{Q}$. Only the perpendicular component of magnetic moments $\boldsymbol{M}$, $\boldsymbol{M}_\perp = \boldsymbol{M} - (\boldsymbol{M} \cdot \hat{\boldsymbol{Q}})\hat{\boldsymbol{Q}}$, contributes to the magnetic scattering [203]. The magnetic scattering in the NSF channel is proportional to $|\boldsymbol{M}_\perp \cdot \boldsymbol{P}|^2$, and that in the SF channel is proportional to $|\boldsymbol{M}_\perp|^2 - |\boldsymbol{M}_\perp \cdot \boldsymbol{P}|^2$. Assumed that $\boldsymbol{M} \parallel c$, the magnetic scattering would be fully suppressed in the SF channel when $\boldsymbol{P} \perp \boldsymbol{Q}$. However, as shown in figure 3.3(c), the magnetic scattering in the SF channel was finite also when $\boldsymbol{P} \perp \boldsymbol{Q}$. To explain the finite SF scattering in both polarizations, we need magnetic moments with a non-negligible component in the ab-plane. Such magnetic moments can be induced by loop currents involving the apical oxygen as shown in Figure 3.3(e) [204, 205]. The later study also determines that the moment direction is 70 ± 10 degrees away from the normal to the CuO$_2$ plane [206].

Since any additional peaks were not observed other than the Bragg peaks, the order is called $\boldsymbol{q} = 0$ magnetic order. The magnetic excitations in the $\boldsymbol{q} = 0$ magnetic order of Hg1201 were investigated by the spin-polarized inelastic neutron scattering measurements [207]. In the cuprates, unpolarized inelastic neutron scattering measurements have revealed the gapped excitations at $\boldsymbol{q}_{AF} = (0.5, 0.5)$ [208, 209]. The characteristic X-shape "hourglass" dispersion appears through $\boldsymbol{q}_{AF}$ in the superconducting state. Whereas the "hourglass" dispersion is also observed in the superconducting state of Hg1201, the dispersion changes to a Y-shape in the pseudogap state as observed in YBCO [210–212]. In the spin-polarized inelastic neutron scattering measurements, the broad peak centering around $\boldsymbol{q} = 0$ was observed in addition to the $\boldsymbol{q}_{AF}$ peak [207]. The additional SF intensity appears in a narrow range of energy 52–56 eV below the pseudogap onset temperature, extending throughout the Brillouin zone with weak dispersion. The excitations are associated as a fundamental collective mode of the $\boldsymbol{q} = 0$ pseudogap order.

3.1.3 Charge density wave state

The charge-density-wave (CDW) state in Hg1201 has been investigated by the X-ray measurements [73, 191]. Cu L_3 edge resonant X-ray diffraction (RXD) measurements were performed on a sample of $p \sim 0.09$, $T_c = 72$ K [73]. Figure 3.4(a) shows the momentum
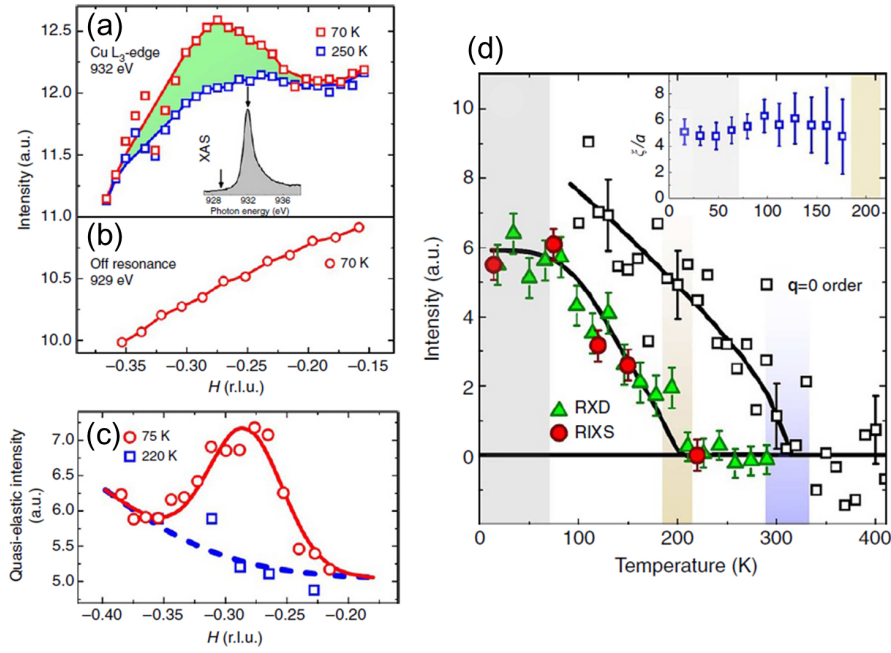
Figure 3.4: The X-ray scattering measurements on Hg1201 [73]. (a) Cu L_3 edge (921 eV) RXD measurements were performed on Hg1201 ($p \sim 0.09$, $T_c = 72$ K). The momentum scan was taken along $(H, 0, L)$ at 70 K (red squares) and 250 K (blue squares). (b) The momentum scan at off-resonant energy 929 eV at 70 K. (c) The inelastic X-ray measurements were performed on the same sample with σ-polarization at the Cu L_3 edge energy. The integrated intensity of the quasi-elastic peak is plotted as a function of H for 70 K (red circles) and 220 K (blue squares). (c) The temperature dependence of the integrated intensity in the momentum scan of RXD (green triangles) and RIXS (red circles). The scattering intensity of the $q = 0$ order [190] is plotted together with white squares. The inset shows the temperature dependence of the CDW correlation length normalized by the lattice constant.

scan along $(H, 0, L)$ at 70 K (red squares) and 250 K (blue squares). At 70 K, the broad peak centers around $H_{CDW} \approx 0.27$. The peak is not due to atomic displacement since the peak is absent at off-resonant energy (929 eV) as shown in figure 3.4(b). The resonant inelastic X-ray (RIXS) measurements were also performed on the same sample with σ-polarization at the Cu L_3 edge energy [73]. The quasi-elastic peak in the energy spectrum was integrated and plotted as a function of H in figure 3.4(c). The intensity at 75 K and 220 K is plotted with the red circles and the blue squares, respectively. At 75 K, the broad peak exists at $H_{CDW} \approx 0.28$. The peak position is consistent with that in the RXD measurements. The enhancement of the scattering intensity observed in both RXD and RIXS is due to the CDW formation. The CDW modulation periodicity is $1/H_{CDW} \approx 3.5a$. Here a is Cu-O-Cu bond length.

Figure 3.4(d) shows the temperature dependence of the CDW peak intensity. The green triangles and the red circles indicate the intensity in the RXD and RIXS measurements, respectively. The finite intensity appears below $T_{CDW} \sim 200\,K$. The intensity is saturated in the superconducting state ($T_c = 72$), which is different from the CDW in YBCO. In the
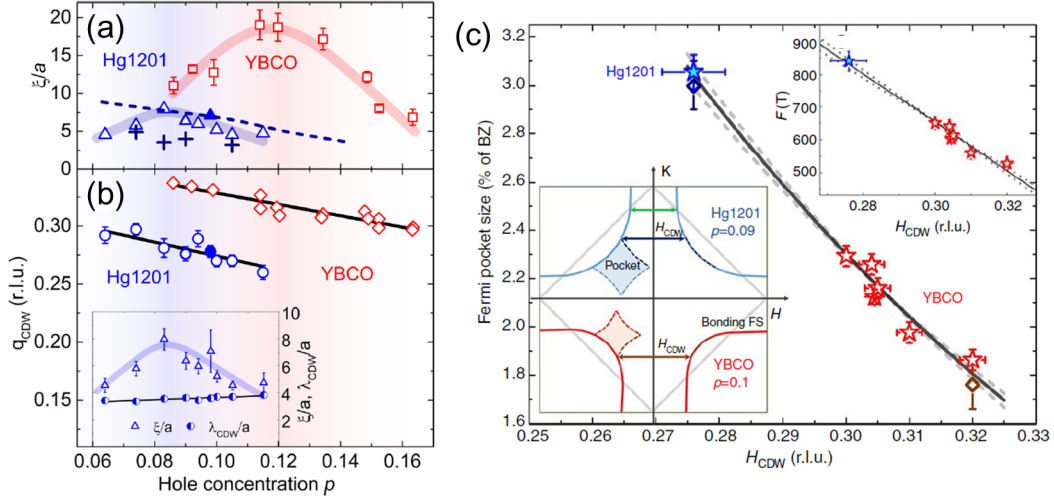
Figure 3.5: (a,b) The doping dependence of the CDW correlation length ξ/a and the CDW modulation wave vector q_{CDW} [191]. The blue triangles and circles respectively indicate the ξ/a and q_{CDW} determined by RXD measurements. The blue crosses indicate the correlation length at 20 K which is estimated by the extrapolation in the temperature dependence. ξ/a and q_{CDW} in YBCO [75] are also shown with red markers. The inset of (b) compares the correlation length and the CDW modulation periodicity λ_{CDW}/a. (c) The Fermi pocket size is plotted as a function of the CDW wave vector [73]. The size of the Fermi pocket was determined by the quantum oscillation, and the CDW wave vector was determined by the X-ray measurements. The inset shows the quantum oscillation frequency as a function of the CDW wave vector. The Brillouin zone is drawn inside the main panel. The solid lines are the Fermi surfaces calculated by the tight-binding model. Arrows indicate the length of the CDW wave vector. The diamond-shaped area is an electron Fermi pocket which is reconstructed by a biaxial CDW order.

superconducting state of YBCO, the CDW peak intensity is strongly suppressed with a clear kink at T_c [65]. The suppression is the evidence for the competing relation between the CDW and superconductivity. In figure 3.4(d) , the scattering intensity of the $q = 0$ magnetic order in the neutron scattering measurements [190] is also plotted with white squares. T_{CDW} is distinctively lower than the onset temperature of the $q = 0$ order. The inset shows the temperature dependence of the correlation length ξ estimated by the FWHM. The correlation length is almost independent of temperature. $\xi/a \approx 5$ is just slightly longer than the CDW modulation periodicity.

The doping dependence is investigated in the later RXD study [191]. The CDW onset temperatures are plotted with purple circles in the phase diagram (Figure 3.1c). The CDW phase extends in a doping range where the superconducting dome is suppressed. Figure 3.5(a) shows that the correlation length ξ/a also has a maximum at $p \sim 0.08$, where the dome is most suppressed. The consistency suggests that the CDW competes with the superconductivity in Hg1201, too. Figures 3.5(a,b) show the correlation length ξ/a (blue triangles) and the CDW modulation wave vector q_{CDW} (blue circles) as a function of the hole concentration. For comparison, those values in YBCO [75] are also plotted with the red markers. The correlation length in Hg1201 is less than half the length in

YBCO. The maximum correlation length is achieved at slightly lower hole concentration in Hg1201 than in YBCO. This is because the superconducting dome is suppressed at a slightly lower doping level in Hg1201. q_{CDW} in Hg1201 is slightly shorter than that in YBCO, but the doping dependence of q_{CDW} is quite similar to that in YBCO. The inset in (b) compares the correlation length ξ/a and the CDW modulation periodicity λ_{CDW}. ξ/a is comparable to λ_{CDW}/a at $p \sim 0.115$. At further doping level, at $p \sim 0.126$, the CDW peak is absent.

The CDW correlation is a candidate for driving the Fermi surface reconstruction at a low-temperature and high-field region in the under-doped cuprates. Inside the pseudogap state of Hg1201, the sign change from the positive to the negative is observed in the Hall and Seebeck coefficients [91]. The measurements were performed with a high field to suppress the superconductivity. The sign change indicates the appearance of electron Fermi surfaces. The negative Nernst coefficient is also reported [91]. Those transport properties indicating the appearance of electron pockets are also reported in YBCO [78, 92, 213]. In YBCO, the presence of Fermi pockets is reported by the quantum oscillation measurements [76]. The multi-frequency spectra in YBCO also include additional hole-like Fermi surface contributions, which may arise from the complicated crystal structure. On the other hand, the single oscillation frequency is reported in Hg1201 [214, 215]. The single frequency indicates the presence of a single electron Fermi surface. The frequency quantitatively agrees with a diamond-shaped electron pocket by biaxial CDW reconstruction as shown in Figure 3.5(c). In the figure, the size of the Fermi pocket is plotted as a function of the CDW wave vector [73]. The size of the Fermi pocket was determined by the quantum oscillation measurements, and the CDW wave vector was determined by the X-ray measurements. The relation between the two quantities collapses on a single curve (solid line), suggesting that the CDW is related to the Fermi surface reconstruction. However, the Fermi surface reconstruction is not reported in the ARPES study [193, 196]. The ARPES measurements were performed at zero field. The recent transport study discusses that the phase transition occurs at a high-field and low-temperature region in the underdoped cuprates [216]. The phase transition is associated with the Fermi surface reconstruction from Fermi arcs to an electron pocket due to a bidirectional CDW order [216].

3.1.4   Rotational symmetry breaking in the pseudogap state

The rotational symmetry breaking in the pseudogap state has not been reported in Hg1201, but it has been well discussed in other hole-doped cuprates. The rotational symmetry breaking in the pseudogap state was firstly suggested by the anisotropic Nernst effect in YBCO. In the pseudogap state of YBCO, the Nernst effect shows large in-plane anisotropy [81, 93]. The Nernst coefficient is extremely anisotropic at low temperature, being roughly ten times larger with $\Delta T \parallel b$ than with $\Delta T \parallel a$. It is recently proposed that the microscopic origin of the anisotropy is the difference between the two in-plane oxygen sites: one connecting Cu in the a-axis direction and the other connecting Cu in the b-axis direction [98]. The microscopic anisotropy has been more investigated in Bi2212 by STM measurements [58, 95, 96]. However, it is still unclear how the oxygen anisotropy is related to the partial gap opening and the symmetry breakings in the pseudogap state.

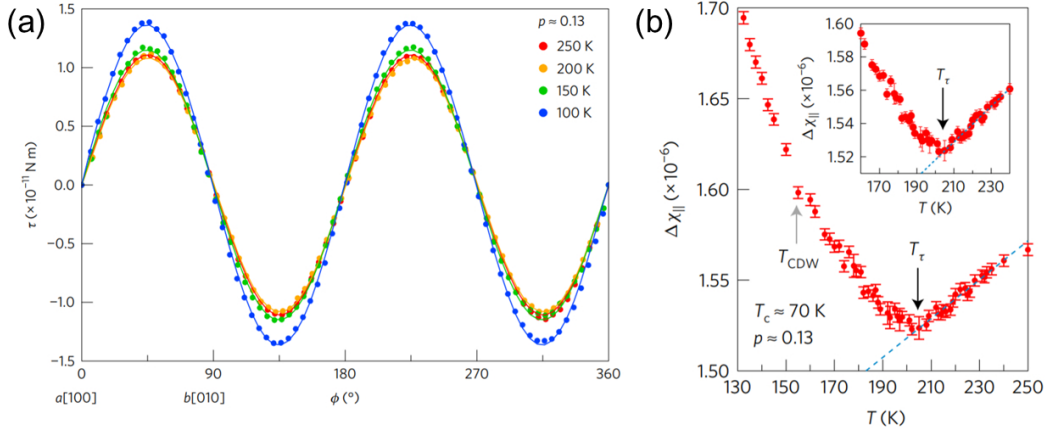In YBCO, magnetic in-plane anisotropy was recently observed in the torque measure-

Figure 3.6: The magnetic torque measurements on YBCO [94]. (a) The in-plane field-angle dependence of the magnetic torque τ for $p \approx 0.13$. ϕ is the field angle from the a-axis. The applied field is 7 T. (b) The temperature dependence of the in-plane anisotropy in the magnetic susceptibility $\Delta\chi_{\parallel} = \chi_{aa} - \chi_{bb}$ for $p \approx 0.13$. T_τ marks the temperature at which the anisotropy exhibits a kink. T_{CDW} is the CDW onset temperature.

ments [94]. Figure 3.6(a) shows the field-angle dependence of the magnetic torque with a field of 7 T. The two-fold sinusoidal torque was observed in a wide range of temperatures, indicating $\chi_{aa} \neq \chi_{bb}$ (equation 2.12). The in-plane anisotropy of the susceptibility $\Delta\chi_{\parallel} = \chi_{aa} - \chi_{bb}$ is plotted as a function of temperature in figure 3.6(b). $\Delta\chi_{\parallel}$ exhibits a kink-like anomaly at T_τ, which is consistent with the pseudogap onset temperature determined by other experiments [81, 85]. The kink in the magnetic susceptibility indicates the occurrence of a thermodynamic phase transition. The anisotropy indicates that the system has C_2 rotational symmetry about the c-axis, which breaks the C_4 symmetry of the CuO$_2$ square lattice. The increase of the anisotropy suggests that the pseudogap state is characterized by the rotational symmetry breaking in the CuO$_2$ plane. However, the finite in-plane anisotropy was also observed above the pseudogap onset temperature due to the orthorhombic crystal structure of YBCO. The orthorhombicity can act as an external field on the nematicity, which may induce the nematic order and align the nematic domain. Therefore, it is still unclear if the pseudogap state spontaneously breaks the rotational symmetry.

To reveal the electronic state in the pseudogap state, it is important to verify if the in-plane anisotropy appears in the pseudogap state of a tetragonal system. Hg1201 is a suitable system since it has a simple tetragonal crystal structure as shown in Figure 3.1(a). However, there are not any previous studies on the nematicity in Hg1201. As discussed in the next section, we performed the torque measurements on Hg1201 to study if the nematic phase transition occurs at the pseudogap onset temperature without the orthorhombicity.

3.2 Magnetic torque measurements of HgBa$_2$CuO$_{4+\delta}$

We performed magnetic torque measurements on a hole-doped cuprate Hg1201. In this section, we explain the results and analyses in the magnetic torque measurements, and discuss the nematic phase transition and the order parameter. We also compare the results with the previous study of the nematicity in YBCO.

3.2.1 Sample preparation

Crystal growth

Three crystals of Hg1201 with different doping levels were prepared; $p \approx 0.11, 0.12, 0.125$. $p \approx 0.11$ and 0.125 were prepared by Ayako Yamamoto in Shibaura Institute of Technology, using a solid-state reaction [189,217]. Powders of HgO, CuO, and BaO were mixed, shaped, and sealed in a quartz tube. Carbonate contamination in BaO was carefully eliminated in the process of heating BaCO$_3$ at $1060\,°$ for $10\,$h several times in a vacuum. Then the shaped bar was sintered in a sealed quartz tube at 750 - 900 °C for $10\,$h and then quenched by water. As-grown samples show a broad superconducting transition. The typical on-set temperature is $98\,$K. Reducing the carbonate contamination is critical for achieving the higher T_c as shown in figure 3.7 [189]. In the study, the carbon content in Hg1201 samples was determined by infrared spectroscopy. Magnetization was measured by a superconducting quantum interference device (SQUID) magnetometer with a magnetic field of $20\,$Oe. Most of the carbon exists as BaO$_{1-x}$(CO$_3$)$_x$ and Hg$_{1-y}$(CO$_3$)$_y$Ba$_2$CuO$_{4+\delta}$. The careful treatment of carbonate contamination achieves a clean sample with a high transition temperature. Annealing at 240–250 °C under various O$_2$ pressures (10^{-6} - 6 atm) controls oxygen content and makes the oxygen distribution homogeneous. Figure 3.8 is a list of annealing conditions, lattice constants, oxygen contents, and superconducting transition temperatures [189], which are respectively determined by X-ray powder diffraction (XRD), iodometric titration, and SQUID. Crystals used for the torque measurements were naturally grown to the size of $\sim 100\,\mu$m and annealed under oxygen. Figures 3.9(a,c) are photos of crystals prepared by this method. The size of the crystals is $150 \times 140 \times 30\,\mu$m^3 for the crystal in figures 3.9(a) and $120 \times 150 \times 50\,\mu$m^3 for the crystal in figures 3.9(c).

On the other hand, $p \approx 0.12$ was cut and annealed from a large crystal which was prepared by Jingnan Cai, Jacob Freyermuth, and Martin Greven in the University of Minnesota [218]. The precursor Ba$_2$CuO$_3$ was prepared by heating the powder of Ba(NO$_3$)$_2$ and CuO at 920 °C in the special quartz kettle with oxygen flow. The high vapor pressure of HgO is the main difficulty of growing large single crystals. The precursor and HgO were mixed stoichiometric proportion and placed in a zirconia crucible together with excess HgO to compensate for a vapor of HgO. The crucible was sealed in a quartz tube with $1.5\,$mm thickness and heated at 800 °C. It was gradually heated up to 1020 °C and then cooled down by 2 °C/h. As-grown samples show the superconductivity at 75–80 K. Oxygen contents are controlled and made homogeneous by annealing at 300–350 °C under oxygen flow. Small crystals $\sim 100\,\mu$m were cut from a large crystal $\sim 2\,$mm. Although the large crystal showed superconductivity at 95 K, the cut small crystals showed various transition temperatures, and the transition was broad due to inhomogeneity of oxygen distribution. Those crystals were annealed in an oxygen atmosphere again by using an
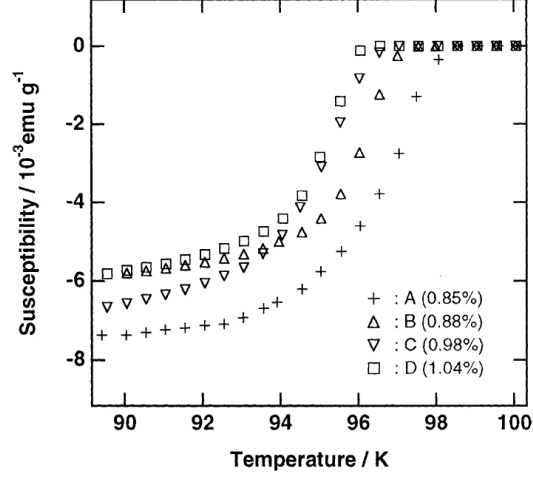
Figure 3.7: Temperature dependence of the magnetic susceptibility of as-grown samples prepared by solid-state reaction [189]. The samples are labeled by the ratio of carbon contents to stoichiometry.

Sample no.	Annealing conditions	a (Å)	c (Å)	V (Å^3)	Oxygen content	T_c (K)
1	Vac. 500°C, 6 days	3.8986(4)	9.5540(9)	144.21	–	Nonsuper.
2	Vac. 450°C, 10 days	3.8948(2)	9.5474(6)	144.82	–	Nonsuper.
3	Vac. 400°C, 10 days	3.8940(4)	9.5500(8)	144.81	4.025	26
4	Vac. 350°C, 6 days	3.8920(1)	9.550(1)	144.66	4.03	46
5	Vac. 300°C, 10 days	3.8895(2)	9.5455(5)	144.40	–	62
6	Ar 400°C, 10 days	3.8869(2)	9.5436(5)	144.18	4.045	72
7	Ar 350°C, 10 days	3.8853(4)	9.5412(7)	144.03	–	77
8	Ar 300°C, 8 days	3.8843(4)	9.5395(9)	143.93	–	83
9	O$_2$ 0.01% 300°C, 7 days	3.8825(2)	9.5377(9)	143.77	4.06	91
10	O$_2$ 0.1% 300°C, 7 days	3.8810(3)	9.5335(6)	143.59	–	95
11	O$_2$ 100% 300°C, 7 days	3.8789(1)	9.5315(4)	143.41	4.09	98
12	O$_2$ 100% 280°C, 7 days	3.8775(1)	9.5259(9)	143.28	–	98
13	O$_2$ 100% 240°C, 21 days	3.8759(3)	9.523(1)	143.06	–	92
14	O$_2$ 6 atm 320°C, 8 days	3.8750(3)	9.5174(6)	142.91	4.10	86
15	O$_2$ 6 atm 270°C, 8 days	3.8743(4)	9.5157(6)	142.83	–	80

Figure 3.8: A list of annealing conditions, lattice constants, oxygen content, and superconducting transition temperatures [189]. The definition of T_c is the onset temperature of the superconducting diamagnetism.
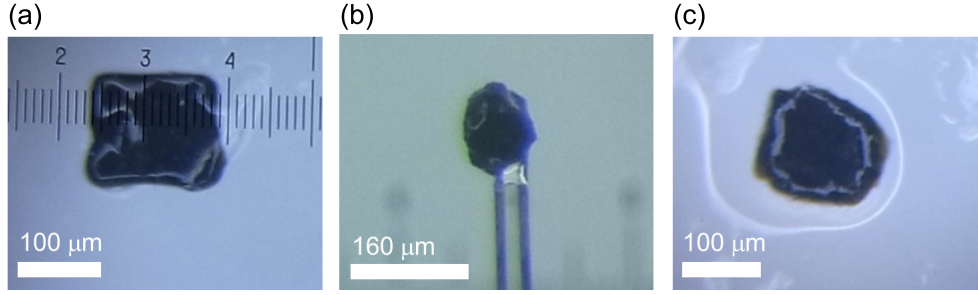
(a)

(b)

(c)

Figure 3.9: (a-c) Photos of crystals used for the torque measurements. The doping levels were determined by magnetization and X-ray diffraction measurements; $p \approx 0.11$, 0.12, and 0.125, respectively.

Table 3.1: Crystals used for torque measurements.

Hole concentration	Dimension	T_c	Growth method
$p \approx 0.11$	$150 \times 140 \times 30\,\mu\mathrm{m}^3$	86 K	Ref. [189, 217]
$p \approx 0.12$	$90 \times 90 \times 40\,\mu\mathrm{m}^3$	90 K	Ref. [218]
$p \approx 0.125$	$120 \times 150 \times 50\,\mu\mathrm{m}^3$	94 K	Ref. [189, 217]

infrared image furnace (Sinku-Riko inc.). A crystal used for the torque measurements was annealed at 200 °C for seven days under 1.9 atm oxygen. Figure 3.9(b) is a photo of the crystal prepared by this method. The size of the crystal is $90 \times 90 \times 40\,\mu\mathrm{m}^3$.

Three crystals listed in table 3.1 were prepared by the two distinct methods. A possible difference is a deficiency of Hg. Reference [189] reports 3% by Reitveld refinement of neutron powder diffraction. On the other hand, reference [218] reports 10% by coupled plasma mass spectroscopy.

Determination of T_c

As shown in table 3.1, the three crystals show different transition temperatures T_c. To study the normal state, the reasonable definition of T_c is an onset temperature of the superconductivity. Magnetization measurements were performed by using a Quantum Design Magnetic Properties Measurement System (MPMS). The magnetic field of 10 Oe was applied along the c-axis, which is perpendicular to the CuO$_2$ plane. A sample was fixed in a plastic straw with Apiezon grease. Figure 3.10 shows the temperature dependence of magnetization M normalized by the magnetization at 5 K. The magnetization was measured under field-cooling (FC) and zero-field-cooling (ZFC). The solid line is a linear fit of the drop in ZFC magnetization. The line has an intersection with an extrapolation

Table 3.2: Lattice constants determined by XRD measurements.

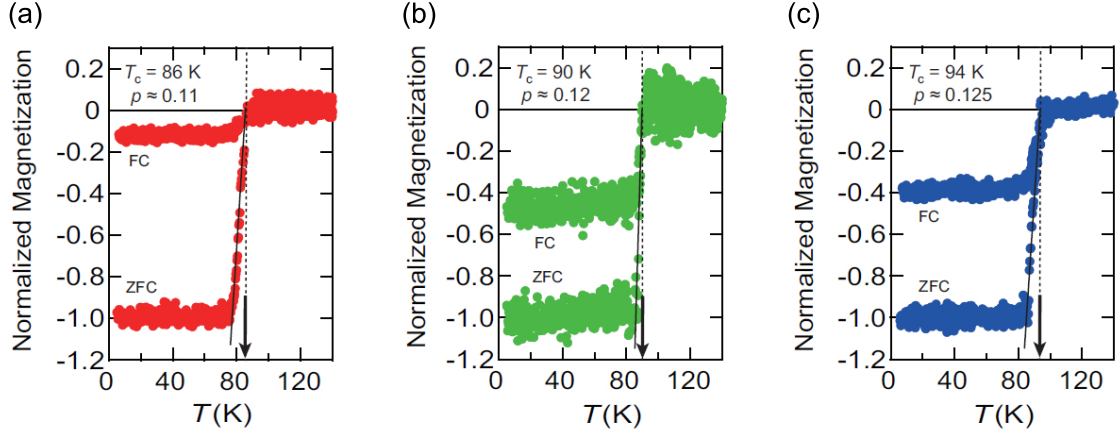| Hole concentration	a (Å)	b (Å)	c (Å)
$p \approx 0.11$	3.887(2)	3.887(1)	9.523(6)
$p \approx 0.12$	3.893(0)	3.893(0)	9.532(0)
$p \approx 0.125$	3.883(2)	3.883(3)	9.530(5)

Figure 3.10: (a-c) Temperature dependence of the normalized magnetization $M(T)/M(5\,\mathrm{K})$ for $p \approx 0.11$, 0.125, and 0.12, respectively [187]. The magnetization was measured under field-cooling (FC) and zero-field-cooling (ZFC) conditions in a magnetic field of $10\,\mathrm{Oe}$ along the c-axis. The arrows indicate T_c determined by the onset of a diamagnetic signal.

of normal state magnetization. The arrows indicate the temperatures of the intersections, which are the definition of T_c. The transition temperatures T_c of the three crystals are $86\,\mathrm{K}$, $90\,\mathrm{K}$, and $94\,\mathrm{K}$, respectively. The hole concentration was estimated using a list of T_c and the concentration p in a previous study [189] as shown in figure 3.7. Though the hole concentration p is not a bijective function of T_c, we assumed that those crystals were underdoped since we observed higher T_c after annealing with higher oxygen pressure. The hole concentrations were $p \approx 0.11$, 0.12, and 0.125.

Determination of axis direction

Determination of the axis direction is indispensable for discussing the symmetry of the torque signal. After the in-plane torque measurements, we performed XRD measurements using a single X-ray diffractometer in the Institute for Solid State Physics at the University of Tokyo. The crystals were glued on a cantilever in the in-plane torque measurements. Later, we performed XRD measurements without removing them from the cantilever. The crystals were tetragonal within the error of measurements. The lattice constants are listed in table 3.2. The lattice constants do not necessarily correspond to those in figure 3.7, since oxygens are removed from crystal in air.

3.2.2 Out-of-plane magnetic anisotropy

The cuprates have large out-of-plane magnetic anisotropy because of the two-dimensionality. The anisotropy at room temperature is mainly caused by Van Vleck orbital susceptibility of the Cu^{2+} ions [219]. The additional anisotropy is induced by the superconducting fluctuation at lower temperatures. To investigate the anisotropy, we performed the out-of-plane magnetic torque measurements before the in-plane magnetic torque measurements. Figure 3.11(a) shows the sample alignment in the out-of-plane torque measurements. We applied the magnetic field of $4\,\mathrm{T}$. The orientation of the field is represented by the polar
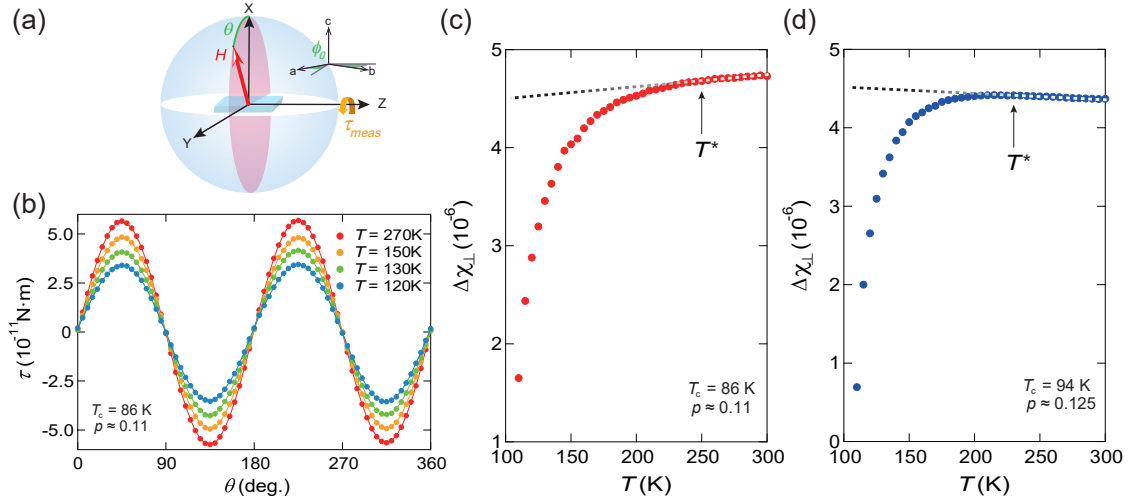
Figure 3.11: (a) The coordinate of the out-of-plane magnetic torque measurements. The magnetic field of 1.5 T rotates in the XY plane, and the field orientation is represented by the polar angle θ. YZ plane is parallel to the unidirectional motion of the cantilever. The orange arrow indicates a rotation that is detected by the cantilever. The Cu-O plane of a sample is aligned within the YZ plane. ϕ_0 is the offset angle of YZ axes from the ab axes. (b) Field-angle θ dependence of magnetic torque $\tau_\perp$ at 270, 150, 130, 120 K with the magnetic field of 4 T for the sample $p \approx 0.11$ [187]. (c,d) The out-of-plane anisotropy of magnetic susceptibility $\Delta\chi_\perp$ is plotted as a function of temperature for $p \approx 0.11$ and $p \approx 0.125$, respectively [187]. The dotted line is a linear fit of $\Delta\chi_\perp$ at $T > 250$ K. T^* is the pseudogap temperature determined by the in-plane magnetic torque measurements.

angle θ. The magnetic field rotates in the XY plane, which is parallel to the unidirectional motion of the cantilever. Thus, the cantilever detects the rotation around the Z-axis. The sample was mounted so that the ab-plane could be parallel to the YZ plane. As shown in figure 3.11(b), magnetic torque $\tau_\perp$ shows two-fold sinusoidal oscillation as a function of the field angle θ. $\tau_\perp$ is well fitted by $\propto \sin 2\theta$. θ dependence of $\tau_\perp$ is derived from the inner product of magnetic torque $\boldsymbol{\tau} = \mu_0 V \boldsymbol{M} \times \boldsymbol{H}$ and the unit vector of Z-axis $\boldsymbol{e}_Z = (-\sin\phi_0, \cos\phi_0, 0)$. Here ϕ_0 is the difference between Y/Z axis and a/b axis as shown in figure 3.11.

$$\tau_\perp = \frac{1}{2}\mu_0 H^2 V \Delta\chi_\perp \sin 2\theta \tag{3.1}$$

$$\Delta\chi_\perp = \chi_{cc} - \left(\frac{\chi_{aa} + \chi_{bb}}{2} + \frac{\chi_{aa} - \chi_{bb}}{2}\cos 2\phi_0 + \chi_{ab}\sin 2\phi_0\right) \tag{3.2}$$

At each temperature, we estimated $\Delta\chi_\perp$ by the fit of $\tau_\perp(\theta)$ with equation 3.1. Figures 3.11 (c,d) show the temperature dependence of $\Delta\chi_\perp$ for $p \approx 0.11$ and 0.125. The dotted lines are the linear fits of $\Delta\chi_\perp$ for $T > 250$ K. $\Delta\chi_\perp$ deviates from the linear lines at the temperature consistent with T^*, which is the pseudogap temperature determined by the in-plane magnetic torque measurements. Such a behavior is also reported in a torque study of YBa$_2$Cu$_3$O$_{7-x}$ [94]. The decrease of $\Delta\chi_\perp$ in the pseudogap state comes from the decrease of the magnetic susceptibility χ_{aa}, χ_{cc} because of the decrease of the density of states [220]. Such temperature dependence of the magnetization is also reported in the powder sample of HgBa$_2$CuO$_{4+\delta}$ [221].
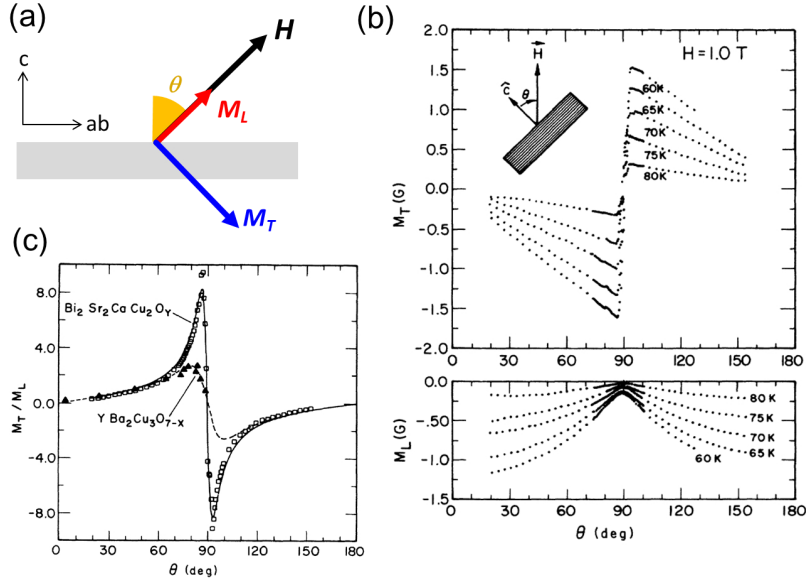
Figure 3.12: (a) The field direction and the induced magnetization in references [222, 223]. The gray rectangular represents a sample, and θ is the field angle from the c-axis. $\boldsymbol{M_L}$ is a longitudinal magnetization parallel to a magnetic field $\boldsymbol{H}$ and $\boldsymbol{M_T}$ is a transverse one. (b) Field-angle dependence of M_T and M_L of Bi-2212 ($T_c = 85$ K) with a magnetic field of 1.0 T at 60, 65, 70, 75, and 80 K [222]. (c) Field-angle dependence of M_T/M_L of Bi-2212 ($T_c = 85$ K) and YBCO ($T_c = 90$ K) with a magnetic field of 1.0 T at 70 K [222]. Solid and dotted lines are fitting functions of M_T/M_L using 3D anisotropic London theory.

3.2.3 Misalignment detection

A piezo resistor of the torque sensor detects unidirectionally constrained motion of the micro-cantilever. The signal includes only the in-plane magnetic torque τ_c when a crystal is precisely mounted so that the cantilever motion can be parallel to the ab plane. However, the crystals were too small to align the crystal direction precisely to the cantilever. Also, the crystal facets were off the high-symmetry direction. The unpreventable misalignment mixes the other torque components τ_a, τ_b in the detected signal. In the case of Hg1201, slight misalignment obscures a signal of the in-plane anisotropy, since the out-of-plane anisotropy is roughly ten times larger than the in-plane anisotropy. Only the solution is applying magnetic field precisely within the CuO$_2$ plane because $H_c = 0$ results in $\tau_a = \tau_b = 0$ (equation 2.12).

The cuprates have large out-of-plane magnetic anisotropy in the superconducting state. By measuring the out-of-plane anisotropy, we can detect an inclination angle of the ab plane. The previous studies of the magnetization report the out-of-plane anisotropy of the superconducting diamagnetism in Bi2212, YBCO, and Tl$_2$Ba$_2$Ca$_2$Cu$_3$O$_{10}$ (Tl-2223) [222, 223]. They measured longitudinal magnetization $\boldsymbol{M_L}$ and transverse one $\boldsymbol{M_T}$ simultaneously as shown in figures 3.12, by using a SQUID equipped with a pair of orthogonal pick-up coils. Figure 3.12(b) is field-angle dependence of M_T and M_L of Bi-2212 ($T_c = 85$ K) with a magnetic field of 1.0 T at 60, 65, 70, 75, and 80 K. M_T is symmetric about $\theta = 90°$, whereas M_L is antisymmetric. M_T is finite due to the anisotropic effective mass arising from the layered structure of the cuprates. In isotropic superconductors,

$M_T = 0$ because current flows within a plane perpendicular to a vortex. On the other hand, the current flows in a canted plane to the vortex in an anisotropic superconductor because the kinetic energy decreases by the current flow along a direction of smaller effective mass. The current flow produces the transverse magnetization when the field angle tilts from the crystal axes. M_T and M_L in an anisotropic superconductor ($m_1 = m_2 \neq m_3$) are formulated by the anisotropic generalization of the London equations [224]:

$$M_L(\theta) = -\frac{\phi_0}{32\pi^2\lambda(T)^2} \ln \frac{(H_{c2}\beta)_\theta}{H} \times \sqrt{m_1 \sin^2\theta + m_3 \cos^2\theta} \tag{3.3}$$

$$M_T(\theta) = \frac{\phi_0}{32\pi^2\lambda(T)^2} \ln \frac{(H_{c2}\beta)_\theta}{H} \times \frac{m_3 - m_1}{\sqrt{m_1 \sin^2\theta + m_3 \cos^2\theta}} \sin\theta \cos\theta \tag{3.4}$$

Here λ is the geometric average penetration depth, ϕ_0 is the superconducting flux quantum, H_{c2} is the upper critical field, and β is a factor coming from an integral cutoff. m_1 and m_3 are respectively the in-plane and the out-of-plane effective mass. M_T/M_L is a useful quantity to estimate the anisotropy of the effective mass m_3/m_1.

$$\frac{M_T}{M_L} = \left(\frac{m_3}{m_1} - 1\right) \frac{\sin\theta \cos\theta}{\sin^2\theta + (m_3/m_1)\cos^2\theta} \tag{3.5}$$

Figure 3.12(a) demonstrates a rough consistency between the experimental M_T/M_L and equation 3.5. The markers represent the field-angle dependence of M_T/M_L in Bi2212 ($T_c = 85\,\mathrm{K}$) and YBCO ($T_c = 90\,\mathrm{K}$). Solid and dotted lines are fitting functions of M_T/M_L using equation 3.5. The fitting coefficient m_3/m_1 is 280 ± 20 in Bi2212, and 30 ± 5 in YBCO. The deviation around $\theta = 90°$ in Bi-2212 comes from the quasi-two-dimensionality of the superconductivity. The dimensionality of the superconductivity is discussed in a recent study of Tl2223 [223]. Tl2223 has three layers of the CuO_2 plane in the unit cell and shows zero resistivity at $125\,\mathrm{K}$ [225]. M_T and M_L of Tl2223 were measured at $100\,\mathrm{K}$ and $110\,\mathrm{K}$ with a magnetic field of $1\,\mathrm{T}$. M_T/M_L is well fitted by the quasi-2D model [226], whereas the 3D model fails around $\theta = 90°$ as well as the case of Bi2212. The important point here is that M_T is antisymmetric about $\theta = 90°$ in both 2D and 3D models.

Since $\boldsymbol{\tau} \propto \boldsymbol{M} \times \boldsymbol{H}$, only the antisymmetric $\boldsymbol{M}_T$ contributes to the magnetic torque. Therefore, the field-angle dependence of the torque is also antisymmetric about $\theta = 90°$. Figure 3.13(a) shows the sample alignment in the magnetic torque measurements for the misalignment detection. The XY plane is parallel to a plane of unidirectionally constrained motion of the cantilever. Thus, the signal detects only the rotation around the Z-axis. The misalignment is an inclination of the CuO_2 plane (red ellipse) to the XY plane. The orientation of the magnetic field is represented in polar coordinates with azimuthal angle Φ and polar angle Θ. Figure 3.13(b) shows Θ dependence of the magnetic torque τ at $80\,\mathrm{K}$ with the field of $1.5\,\mathrm{T}$ for the sample $p \approx 0.11$. An antisymmetric function fits Θ dependence of τ remarkably well. The arrows indicate the antisymmetric point Θ_{ab}, at which the field crosses the CuO_2 plane of the sample. Θ dependence of the torque was measured by changing Φ in increments of $10°$. As plotted in figure 3.13(c), Θ_{ab} collapses on a sine curve $\sim \Theta_{ab}^0 \sin(\Phi + \Phi_0)$, which is represented by solid lines. We used the fitting coefficients, Θ_{ab}^0 and Φ_0, for applying the field within the CuO_2 plane in the in-plane magnetic torque measurements. The measurements for the misalignment detection were performed for all the samples $p \approx 0.11$, 0.12, 0.125 before performing the in-plane
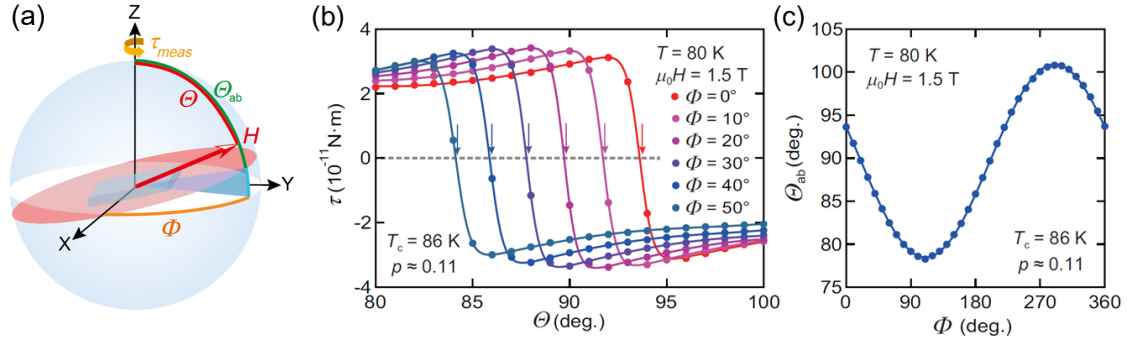
Figure 3.13: (a) The sample alignment and the field orientation in the misalignment detection [187]. The XY plane is parallel to the cantilever motion. The red ellipse represents the CuO_2 plane of the sample. Φ and Θ are the azimuthal and polar angles of the magnetic field. Θ_{ab} is an angle at which the field crosses the CuO_2 plane. (b) Field angle dependence of the magnetic torque τ at 80 K with a magnetic field of 1.5 T for the sample $p \approx 0.11$ [187]. Θ dependence of the torque is plotted for $\Phi = 0°, 10°, 20°, 30°, 40°$, and $50°$. The solid lines are the fits with an antisymmetric function. The arrows indicate polar angles Θ_{ab}, which is an antisymmetric point of the fitting function. (c) Θ_{ab} is plotted as a function of Φ [187]. The solid line is a fitted sinusoidal curve.

torque measurements. We cooled down the sample just below T_c, performed the torque measurements for the misalignment detection, and measured the temperature dependence of the in-plane magnetic anisotropy by increasing the temperature.

3.2.4 In-plane magnetic anisotropy

We performed the in-plane magnetic torque measurements on $p \approx 0.11$, 0.12, and 0.125. As sown in figure 3.14(a), we precisely applied the magnetic field of 4 T within the *ab*-plane, which was determined by the misalignment detection (section3.2.3). The field angle is represented by the azimuthal angle ϕ. The magnetic torque is $\boldsymbol{\tau} = (0, 0, \tau_c)$ since $\tau_a = \tau_b = 0$ when $H_c = 0$. Due to the misalignment, the *c*-axis of the sample is inclined with respect to the rotation axis of the cantilever (Z-axis). Therefore, detected torque signal τ_{meas} is the inner product of the torque $\boldsymbol{\tau}$ and the unit vector along the Z-axis $\boldsymbol{e}_Z$; $\tau_{meas} = \boldsymbol{\tau} \cdot \boldsymbol{e}_Z$. τ_c is calculated by $\tau_{meas}/\sin\Theta_{ab}^0$, where Θ_{ab}^0 is the inclination angle of the sample. We fitted τ_c with $\sum_{n=0}^{8} A_n \sin 2n\pi(\phi - \phi_0)/360$. Only the term $n = 2$, two-fold oscillation as a function of ϕ, is finite for all the samples above 100 K. The finite two-fold oscillation was observed up to room temperature, where we expect the strange metal state according to the phase diagram. However, Hg1201 has the four-fold rotational symmetry about the *c*-axis, which prohibits the two-fold oscillation in the normal state. Near the room temperature, the amplitude and the phase of the two-fold oscillation were independent of temperature. The phase was away from the high symmetry direction and random among the samples. Therefore, we regarded the two-fold oscillation as extrinsic signals τ_{ext}, which can arise from the anisotropic magnetoresistance of piezo resistors. We
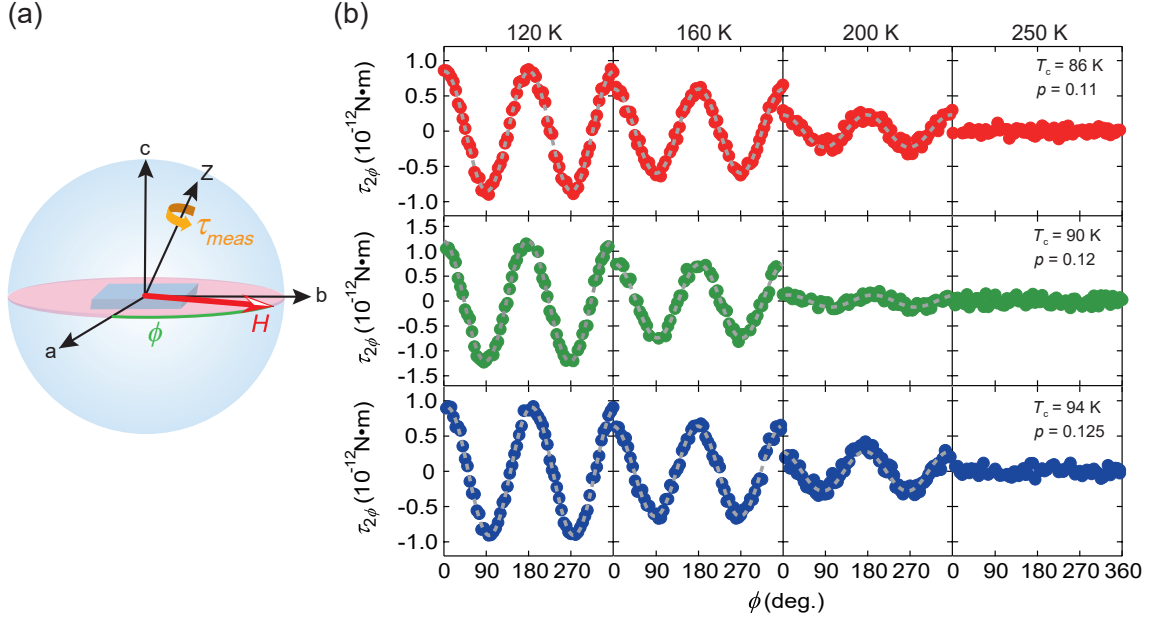
Figure 3.14: (a) The sample alignment and the field orientation in the in-plane magnetic torque measurements. The magnetic field of 4 T was precisely applied within the ab-plane. The cantilever detects a rotation around the Z-axis, which is inclined with respect to the c-axis of the sample. The rotation angle of the magnetic field is represented by the azimuthal angle ϕ. (b) The intrinsic two-fold oscillation $\tau_{2\phi}$ at 120, 160, 200, and 250 K for $p \approx 0.11$, 0.12, and 0.125 [187]. The dotted lines are the fits with a two-fold sinusoidal curve.
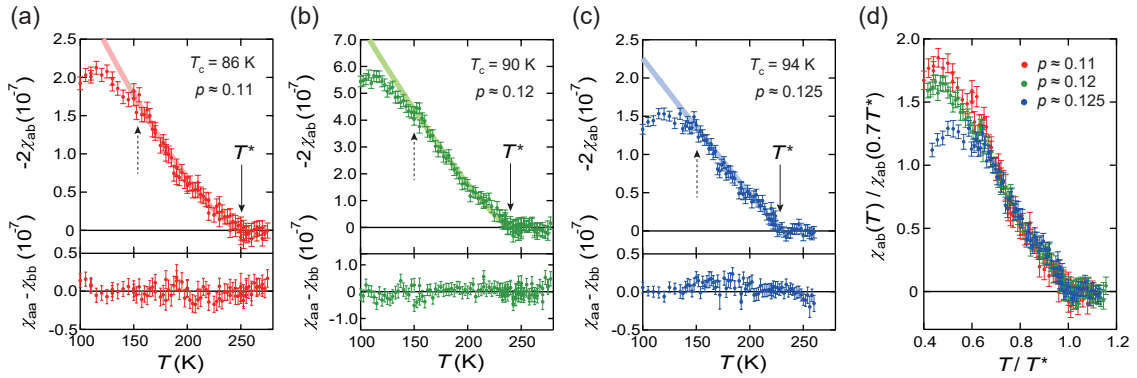
Figure 3.15: (a) Temperature dependence of $-2\chi_{ab}$ and $\chi_{aa} - \chi_{bb}$ for $p \approx 0.11$, (b) 0.12, and (c) 0.125 [187]. The nonzero χ_{ab} appears below T^* (solid arrows). $-2\chi_{ab}$ deviates from the power-law behavior $\propto (T^* - T)^\alpha$ ($1.0 < \alpha < 1.3$) (thick solid lines) at T' (dotted arrows). (d) The normalized susceptibility $\chi_{ab}(T)/\chi_{ab}(0.7T^*)$ is plotted as a function of the normalized temperature T/T^* [187].

extracted the intrinsic two-fold oscillation $\tau_{2\phi}$.

$$\tau_{2\phi} \equiv \tau_c - \tau_{ext} - \sum_{n=0}^{8,n\neq2} A_n \sin 2n\pi(\phi - \phi_0)/360 \qquad (3.6)$$

$\tau_{2\phi}$ is plotted as a function of the field angle ϕ in figure 3.14(b) for $p \approx 0.11$, 0.12, 0.125. $\tau \equiv \tau_c - \tau_{ext}$ is shown in figure 5.1 of appendix. At 250 K, all the samples do not show any intrinsic two-fold oscillations. On the other hand, the intrinsic two-fold oscillation appears at 200 K. The amplitude of the oscillation develops by decreasing the temperature, whereas the phase is temperature independent. $\tau_{2\phi} \propto \cos 2\phi$ for all the samples at 200 K, 160 K, and 120 K.

To estimate the anisotropy in the susceptibility, we fitted $\tau_{2\phi}$ with equation 2.12. The fits are represented by gray dotted lines in figure 3.14(b). Since $\tau_{2\phi} \propto \cos 2\phi$ for all the samples, $\chi_{aa} - \chi_{bb} = 0$ and $\chi_{ab} \neq 0$. Nonzero χ_{ab} indicates the in-plane magnetic anisotropy. We performed the measurements at very close temperature intervals to investigate the temperature dependence of the in-plane magnetic anisotropy. $-2\chi_{ab}$ and $\chi_{aa} - \chi_{bb}$ are plotted in figures 3.15(a-c). Both $-2\chi_{ab}$ and $\chi_{aa} - \chi_{bb}$ are almost zero at the room temperature. Whereas $\chi_{aa} - \chi_{bb} \doteq 0$ down to 100 K, $-2\chi_{ab}$ increases below T^*. $T^* = 250$ K, 240 K, and 230 K for $p \approx 0.11$, 0.12, and 0.125, respectively. To analyze the temperature dependence, we fitted $-2\chi_{ab}$ with a power-law function $-2\chi_{ab} \propto (T^* - T)^\alpha$ near T^*. The fitting curves are shown with thick solid curves in figures 3.15(a–c). The exponent α is $1.0 < \alpha < 1.3$ in the three samples. Below 150 K, $-2\chi_{ab}$ deviates from the power law. The onset temperature of the deviation T' is indicated by dotted arrows in the figures. $T' = 155$ K, 150 K, and 150 K for $p \approx 0.11$, 0.12, and 0.125, respectively. To see the universality of the temperature dependence, the normalized susceptibility $\chi_{ab}(T)/\chi_{ab}(0.7T^*)$ is plotted as a function of the normalized temperature T/T^* in figure 3.15(d). The normalized susceptibility of all the samples collapses on a single super linear curve above $\sim T'$.

3.2.5 Phase transition and symmetry breaking

Near the room temperature, the intrinsic magnetic torque is independent of the field-angle ϕ, since the crystal has the four-fold rotational symmetry about the c-axis. On the other hand, the finite two-fold oscillation $\tau_{2\phi}$ appears below T^*, indicating that the rotational symmetry about the c-axis is reduced from C_4 to C_2. Therefore, the pseudogap state of Hg1201 breaks the rotational symmetry but preserves the translational symmetry. Such an order is called a nematic order. To discuss the ordering mechanism, it is important to determine the order parameter symmetry.

The magnetic toque directly probes the order parameter symmetry, since the torque is the field angular derivative of the free energy F; $\tau_c = -\partial F/\partial \phi$. Here we consider coupling terms between the order parameter and the magnetic field. Table 5.3 is the character table of the crystal symmetry D_{4h}, and table 5.4 is a list of linear and quadratic basis functions of the D_{4h} point group. When $\boldsymbol{H} = (\cos\phi, \sin\phi, 0)$, the quadratic ones induces two-fold oscillations of the torque as a function of ϕ. Among the quadratic functions in table 5.4, only $H_x H_y = \frac{1}{2}\sin 2\phi$ gives $\tau_{2\phi} \propto \cos 2\phi$, which is classified in B_{2g}. Since the order parameter couples with the basis function of the same symmetry, the order parameter
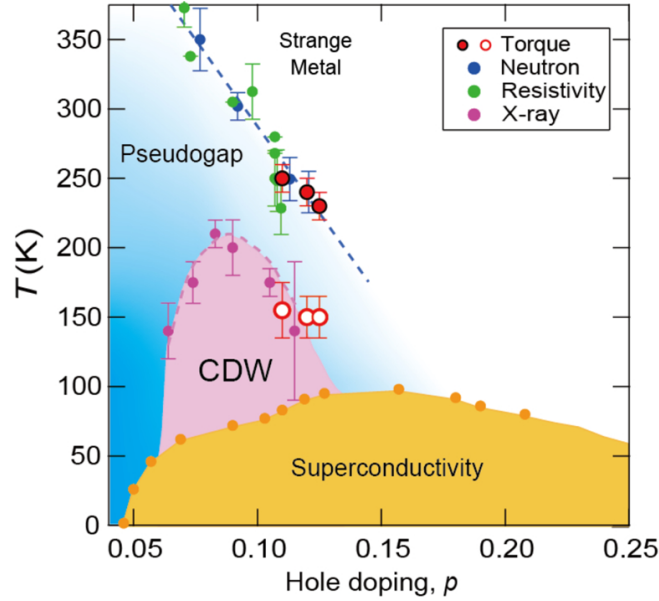
Figure 3.16: The phase diagram of HgBa$_2$CuO$_4$ [187]. The superconducting dome (yellow area) is determined by the onset temperatures of the superconducting diamagnetic response (orange circles) [189]. The pseudogap onset temperatures are determined by resistivity measurements [19] (green circles) and neutron scattering measurements (blue circles) [84, 190]. The CDW onset temperatures are determined by X-ray measurements (purple circles) [73, 191]. The red filled and open circles are T^* and T', respectively, which are determined in the torque measurements.

symmetry is also B_{2g}. The leading order in the free energy is

$$F = a\Omega_{B_{2g}} H_x H_y + \cdots \tag{3.7}$$

a is a coupling constant. $\Omega_{B_{2g}}$ is the nematic order parameter that has B_{2g} symmetry.

Since $\Omega_{B_{2g}} \propto \chi_{ab}$, the kink at T^* indicates an occurrence of the second-order thermodynamic phase transition. T^* is plotted with red filled circles in the phase diagram (figure 3.16). T^* corresponds to the pseudogap onset temperatures determined by the resistivity measurements [19] and also corresponds to the onset temperatures of $\boldsymbol{q} = 0$ magnetic order observed in the neutron scattering [84, 190]. The correspondence indicates that the thermodynamic nematic phase transition occurs simultaneously with the occurrence of the pseudogap formation and the time-reversal symmetry breaking.

Temperature dependence of the order parameter $\propto (T_c - T)^\alpha$ near the transition temperature T_c is universal in the same universality class. For example, the critical exponent is $\alpha = 1/2$ in the mean-field class. On the other hand, χ_{ab} of Hg1201 exhibits the super linear temperature dependence just below T^*. One possibility is that $\Omega_{B_{2g}}$ is not the order parameter but the higher-order of E_g or E_u, as discussed in a study on Cd$_2$Re$_2$O$_7$ [182]. Table 5.5 is the direct product table of the irreducible representations in the D_{4h} point group. Only the direct products of E_g or E_u may have B_{2g} symmetry. However, the elastoresistance measurements on (Pb,Bi)$_2$Sr$_2$CaCu$_2$O$_{8+\delta}$ revealed that the order parameter is the nematic type [227]. Thus, we expect that the order parameter symmetry in Hg1201 is also the nematic type, not E_g or E_u. Another possibility is the broadening
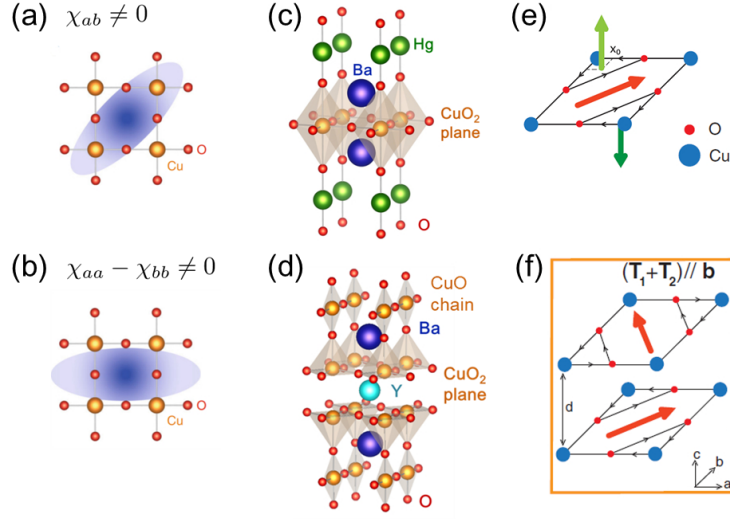
Figure 3.17: (a) Schematics of the magnetic anisotropy $\chi_{ab} \neq 0$ and (b) $\chi_{aa} - \chi_{bb} \neq 0$. (c) The crystal structure of HgBa$_2$CuO$_{4+\delta}$ (Hg1201) and (d) YBa$_2$Cu$_3$O$_{7-\delta}$ (YBCO). (e) The pattern of loop currents which has been mostly discussed and (f) the pattern proposed in YBCO [82]. The red arrows represent the loop current order parameter defined in each CuO$_2$ layer.

of the transition by the external field. Since the magnetic torque is proportional to the square of the field, the torque measurements do not have a high resolution at small fields. The zero-field limit should be investigated by other probes. It is also proposed that the phase transition is associated with physics beyond the Landau paradigm [228].

Inside the pseudogap state, χ_{ab} is suppressed below T'. T' is also plotted in figure 3.16 with red open circles. T' is roughly consistent with CDW onset temperatures. The consistency suggests the competing relation between CDW and the nematic order.

3.2.6   Orientation of the nematic order parameter

A nematic order was previously suggested in the pseudogap phase of YBCO by the torque measurements [94]. In YBCO, $\chi_{aa} - \chi_{bb} \neq 0$ and $\chi_{ab} = 0$, indicating that the nematic order parameter orients toward the Cu-O bonding direction as shown in figure 3.17(b). The nematic order does not break the crystal symmetry, since YBCO is orthorhombic D_{2d}, which has only C_2 rotational symmetry about the c-axis. The nematic orientation in YBCO is tilted by 45° to that in Hg1201 (figure 3.17a).

The difference in the nematic orientation may result from the difference in the crystal structure as shown in figure (c,d). First, the CuO$_2$ square lattice of YBCO is not perfectly square and is a little elongated along the b-axis, whereas the CuO$_2$ square lattice of Hg1201 is perfectly square. Second, YBCO has two adjacent CuO$_2$ square lattices in the unit cell, which may interact with each other. On the other hand, Hg1201 has a single CuO$_2$ square lattice in the unit cell. Third, YBCO has the CuO chains along the b-axis, but Hg1201 does not. In YBCO, the excess oxygen is doped in the CuO chain, elongating the crystal structure to the chain direction, and the hole carriers are doped in the CuO$_2$ plane by the charge transfer from the chain to the plane [229, 230].
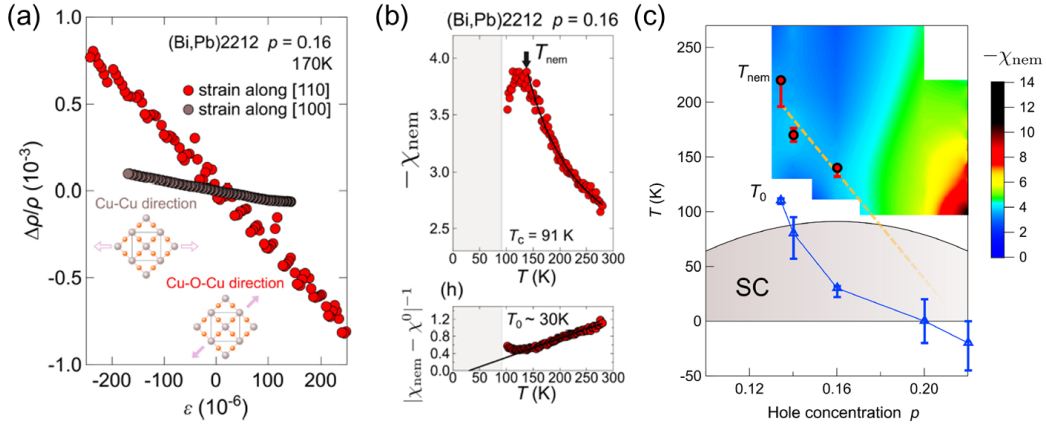
Figure 3.18: Elastoresistance measurements on (Bi,Pb)2212 [227]. (a) The change in the resistivity $\Delta\rho/\rho$ is plotted as a function of strain ϵ along [110] (red circles) and [100] (brown circles) for $p = 0.16$. (b) The nematic susceptibility χ_{nem} and the inverse susceptibility are plotted as a function of temperatures for $p = 0.16$. T_{nem} marks the temperature at which χ_{nem} deviates from the fitting curve, and T_0 marks the temperature at which the linear extrapolation of the inverse susceptibility crosses the horizontal axis. (c) T_{nem} and T_0 are plotted as a function of the hole concentration p.

The bond-directional anisotropy in the pseudogap state of YBCO is also observed in the spin-polarized neutron scattering [82]. The study reports that the intensity of the spin-flipped scattering is different between the Bragg peaks, $\boldsymbol{Q} = (1, 0, 0)$ and $(0, 1, 0)$, which indicates the magnetic anisotropy along the Cu-O bonding direction. The magnetic scattering has been associated with loop current orders [86]. In the mostly discussed pattern of loop currents, the order parameter orients toward the diagonal direction as shown in figure 3.17(e). If the nematic orientation is different by 90° between two adjacent CuO$_2$ layers as shown in figure 3.17(f), the bond-directional magnetic anisotropy can be probed in the neutron measurements. One may expect that such a pattern of loop currents can explain the difference of the nematic order parameter orientation between single-layered Hg1201 and double-layered YBCO. However, the nematic order is even-parity, which is inconsistent with the odd-parity loop current order. Further studies are required to conclude if those two orders have the same origin or independently coexist.

3.3 Even-parity nematic order

The nematicity is also studied in the pseudogap state of Bi2212. In this compound, the intra-unit-cell nematicity along the Cu-O bonding direction has been reported by STM/STS measurements in the superconducting state [58, 95, 96]. Recently, the strong coupling between the nematicity and the strain was observed in the pseudogap state of Bi$_{2-x}$Pb$_x$Sr$_2$CaCu$_2$O$_{8+\delta}$ ((Bi,Pb)2212) [227, 231]. The Pb substitution in the Bi site suppresses the super-modulations of BiO planes along the Cu-Cu bonding direction. The modulation makes the crystal orthorhombic. As the orthorhombicity can affect the orientation of the order parameter, (Bi,Pb)2212 was used for the measurements.

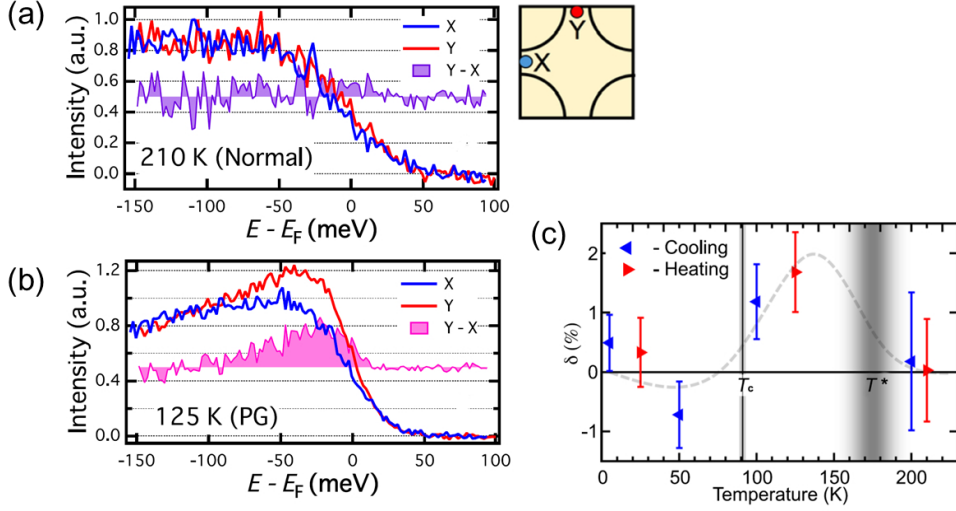Figure 3.18(a) shows the change of the resistivity $\Delta\rho/\rho$ as a function of the uniaxial

Figure 3.19: ARPES on (Bi,Pb)-2212 under the strain along the Cu-O bonding direction [231]. (a) The energy distribution curves at $210\,\mathrm{K}$ and (b) $125\,\mathrm{K}$. The red and blue lines represent the curves at $\boldsymbol{k} = (-\pi, 0)$ (X) and $\boldsymbol{k} = (0, \pi)$ (Y). The difference, $Y - X$, is plotted with purple/pink curves. (c) The anisotropy parameter δ is plotted as a function of temperature. The dotted gray line is a guide to the eye.

strain ϵ, when the strain is applied along the Cu-O-Cu direction (red circles) and the diagonal direction (brown circles) for $p = 0.16$. The resistivity changes more sensitively to the strain along the Cu-O bonding direction, indicating the nematicity along the Cu-O bonding direction is more significant than the Cu-Cu direction. The nematic susceptibility χ_{nem} is defined by $\chi_{nem} \equiv d\eta/d\epsilon$ ($\eta = \Delta\rho/\rho$). In figure 3.18(b), χ_{nem} and the inverse susceptibility $|\chi_{nem} - \chi^0|^{-1}$ are plotted as a function of temperature. The solid line in the upper panel is the fit by $\chi_{nem} = \chi^0 + C/(T - T_0)$. T_{nem} marks the temperature where the susceptibility deviates from the Curie-Weiss curve, and T_0 marks the linear extrapolation of the inverse susceptibility crosses the horizontal axis. In figure 3.18(c), T_{nem} and T_0 are plotted as a function of the hole concentration p. T_{nem} corresponds to the pseudogap temperature determined by other experiments [83, 232–234]. This indicates that the nematic transition occurs at the pseudogap temperature, and the nematic order parameter linearly couples with the strain. The results suggest that the nematic order in the pseudogap state is also even-parity and time-reversal invariant since the strain is even-parity and time-reversal invariant.

The coupling between the nematicity and the strain is also demonstrated by ARPES under the uniaxial strain along the Cu-O bonding direction [231]. Figure 3.19(a) shows the energy distribution curves at $210\,\mathrm{K}$. The red and blue lines represent the curves taken around $\boldsymbol{k} = (-\pi, 0)$ (X) and $\boldsymbol{k} = (0, \pi)$ (Y). The difference between the two curves, $X - Y$, is plotted with a purple line. The difference is absent at $210\,\mathrm{K}$, where the system is in the strange metal state. On the other hand, the finite difference appears at $125\,\mathrm{K}$, where the system is in the pseudogap state. In the constant energy surface near the Fermi level, a slightly anisotropic Fermi surface was observed in the pseudogap state. These results indicate that the anisotropy of the electronic state couples with the strain. The Fermi surface was fitted with the single-band tight-binding model using the anisotropy parameter

δ. δ is the anisotropy in the hopping parameters along the Cu-O bonding direction. Figure 3.19(c) shows the temperature dependence of δ. δ is $\sim 1\%$ in the pseudogap state. On the other hand, δ is strongly suppressed in the superconducting state. They propose that the suppression indicates a competing relation between the pseudogap state and the superconducting state. However, it is not clear if the anisotropy is suppressed due to the superconductivity or the CDW.

The even-parity nematic order is different from loop current orders, which have been discussed in the pseudogap of the cuprates [86, 202]. In the loop current order, a pair of clockwise and anti-clockwise loop currents induces staggered orbital moments within the unit cell. The inversion and time-reversal symmetries are broken in the loop current orders, which prohibit the linear coupling between the order parameter and the strain. Therefore, the observation of the coupling between the nematicity and the strain [227, 231] suggests that the even-parity nematic order coexists with a loop current order.

The most important issue in the high-T_c cuprate superconductors is the relation between the pseudogap phase and the superconducting phase. In the phase diagram, the linear extrapolation of T^* has an end point inside the superconducting dome, suggesting the quantum critical point (QCP) inside the superconducting phase. The presence of the QCP is also suggested by experiments in the superconducting phase [235]. The mechanisms of various unconventional superconductivity have been associated with the large fluctuations arising from a QCP located inside the superconducting phase. Therefore, the mechanism of the high-T_c superconductivity in the cuprates has been also associated with the pseudogap QCP. The presence of strong fluctuations arising from the QCP is suggested in a strange metal state, which locates just above the QCP in the phase diagram. The strange metal state exhibits non-Fermi-liquid behavior such as T-linear resistivity [19, 109], which may result from the strong fluctuations of the QCP. Furthermore, the elastoresistance measurements [227] suggest the strong nematic fluctuations in the strange metal state. As shown in figure 3.18(c), the nematic susceptibility is enhanced near the QCP, suggesting the presence of strong nematic fluctuations. However, it is unclear how the $\boldsymbol{q} = 0$ type fluctuations cause the pseudogap opening and the T-linear resistivity.

The vestigial nematicity is an idea that relates the $\boldsymbol{q} = 0$ nematicity to $\boldsymbol{q} \neq 0$ fluctuations. Recently, it is reported that the characteristic energies of the intra-unit-cell nematicity and the CDW are comparable [96]. This suggests that the nematicity and the CDW originate in an identical electronic state. Some theories propose that the stripe CDW order can survive as a $\boldsymbol{q} = 0$ nematic order under quenched disorder [99–101]. The survived $\boldsymbol{q} = 0$ state is called vestigial nematicity. Thus, a highly disordered density wave can open a partial gap in the Fermi surface, but the long-range CDW is destroyed by disorder, resulting in the $\boldsymbol{q} = 0$ nematicity.

Chapter 4

Bond directional anapole order in a spin-orbit coupled Mott insulator $\mathrm{Sr_2(Ir_{1-x}Rh_x)O_4}$

A spin-orbit assisted Mott insulator $\mathrm{Sr_2IrO_4}$ exhibits various electronic states by chemical doping or substitution. The substitution of Rh at the site of Ir suppresses the Mott insulating phase. In $\mathrm{Sr_2Ir_{1-x}Rh_xO_4}$, the hidden order state appears in the vicinity of the Mott insulating phase. Various symmetries are broken in the hidden order phase, which is associated with the pseudogap phase of the high-T_c cuprate. This chapter first summarizes the effect of Rh substitution on the $\mathrm{Sr_2IrO_4}$ and then reviews experiments on symmetry breaking in the hidden order state. The main discussion in this chapter is the magnetic torque measurements on $\mathrm{Sr_2Ir_{1-x}Rh_xO_4}$. The magnetic torque measurements have provided the first thermodynamic evidence for the phase transition at the hidden order onset temperature and revealed that the hidden order breaks the rotational symmetry. The detailed discussion determines the symmetry of the order parameter, which is consistent with the loop current order proposed in the cuprate. At the end of this chapter, a possible pattern of loop currents in the hidden order is discussed.

4.1 Phase diagram of $\mathrm{Sr_2Ir_{1-x}Rh_xO_4}$

4.1.1 Effect of Rh substitution

Substitution of Rh at the Ir sites mainly has two impacts on the electronic state of $\mathrm{Sr_2IrO_4}$. One is the reduction of spin-orbit interaction, and the other is the change of the carrier concentration. Due to the complexity of the substitution effect, various ground states appear by the substitution such as canted antiferromagnetic orders and a reentrant insulating state.

$\mathrm{Sr_2RhO_4}$ is a compound in which the Ir in $\mathrm{Sr_2IrO_4}$ is fully substituted by Rh. The compound has the isostructure of $\mathrm{Sr_2IrO_4}$, and is classified in the same space group $I4_1/acd$. The $\mathrm{RhO_6}$ octahedra of $\mathrm{Sr_2RhO_4}$ are tilted so that they rotate $9.6 - 9.7°$ about the c-axis, whereas the $\mathrm{IrO_6}$ octahedra of $\mathrm{Sr_2IrO_4}$ rotate $11 - 12°$. In contrast to $\mathrm{Sr_2IrO_4}$, which is a spin-orbit assisted Mott insulator, $\mathrm{Sr_2RhO_4}$ is metallic and paramag-
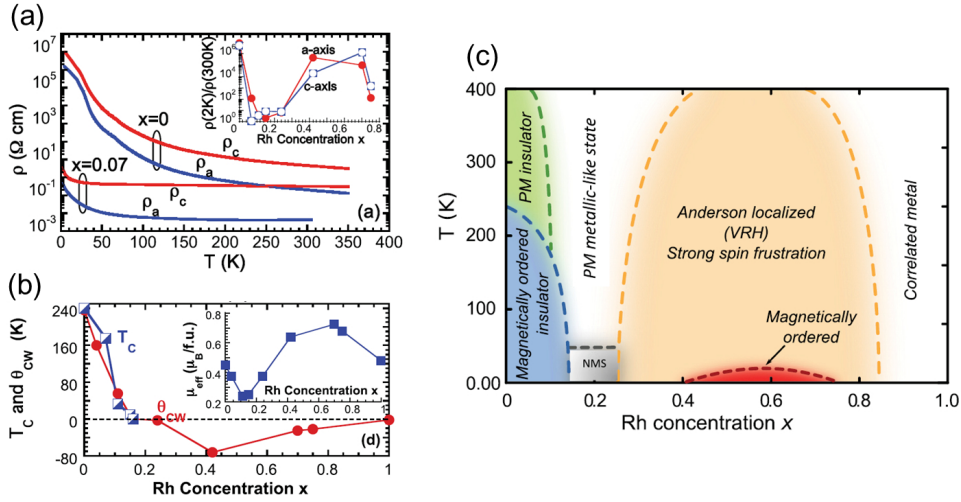
Figure 4.1: (a) Temperature dependence of resistivity along the a-axis ρ_a and that along the c-axis ρ_c for $x = 0$ and $x = 0.07$ [158]. In the inset, $\rho(2\,\mathrm{K})/\rho(300\,\mathrm{K})$ is plotted as a function of Rh concentration x. (b) The magnetic transition temperature T_C and the Curie-Weiss temperature Θ_{CW} are plotted as a function of the Rh concentration x in the main panel and as a function of the effective moment μ_{eff} in the inset [158]. (c) The phase diagram of $Sr_2Ir_{1-x}Rh_xO_4$ [158].

netic [115, 116]. $4d$ electrons of Rh have weaker spin-orbit interaction $\sim 0.16\,\mathrm{eV}$ [158] than that of Ir $5d$ electrons. The substitution reduces the splitting between the $J_{eff} = 1/2$ and $J_{eff} = 3/2$ bands. Those bands are more evenly filled by the five $4d$ electrons as calculated by local density approximation [119]. The large Kadowaki-Woods ratio suggests that Sr_2RhO_4 is a strongly correlated metal, rather than normal metal. Kadowaki-Woods ratio is $\sim 11\,\mu\Omega\mathrm{cm\,mol^2K^2J^{-2}}$ [116], which is larger than that of transition metals $\sim 0.4\,\mu\Omega\mathrm{cm\,mol^2K^2J^{-2}}$ [236]. Also, calculation by a dynamical mean-field theory found that Sr_2RhO_4 is close to Mott transition [119].

In the intermediate substitution regime between Sr_2IrO_4 and Sr_2RhO_4, various electronic states appear in the phase diagram. Figure 4.1(c) shows the phase diagram of $Sr_2Ir_{1-x}Rh_xO_4$ determined in reference [158]. As shown in figure 4.1(a), 7% Rh substitution reduces both the in-plane and out-of-plane resistivity. The reduction of the resistivity is explained by several mechanisms, such as the effective hole doping [157] or the impurity band [160]. The change from the Mott insulator Sr_2IrO_4 to the correlated metal Sr_2RhO_4 is not a simple Mott transition or a crossover. In the inset of figure 4.1(a), $\rho(2\,\mathrm{K})/\rho(300\,\mathrm{K})$ is plotted as a function of Rh concentration x. $\rho(2\,\mathrm{K})/\rho(300\,\mathrm{K})$ is reduced by the slight rhodium substitution and enhanced again by increasing the Rh concentration to $x \sim 0.4$. Reference [158] points out that the enhancement of the resistivity is possibly caused by the Anderson localization due to the Ir/Rh site disorder. The disorder scattering may result from a mismatch of the energy levels or a mismatch of the octahedral rotations. However, it is unclear how the Anderson localization occurs in the material which is far from the perfect two-dimensional metal. On the other hand, detailed X-ray absorption spectroscopy suggests that the reduction of carrier concentration causes the reentrant insulating state [161]. In figure 4.1(b), the magnetic transition temperature T_C and the
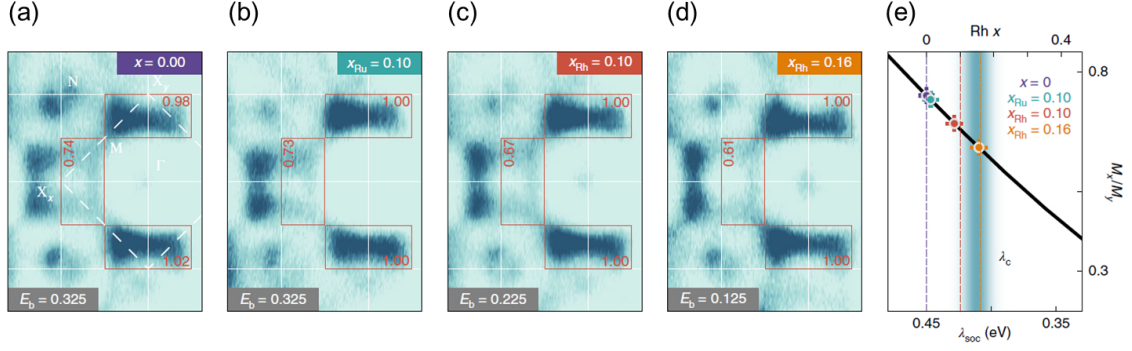
Figure 4.2: ARPES study on $Sr_2Ir_{1-x}Ru_xO_4$ and $Sr_2Ir_{1-x}Rh_xO_4$ using σ-polarized light [237]. (a-d) The constant energy maps were taken at energy such that the size of the pocket around X is the same for all concentrations: (a) Sr_2IrO_4, (b) $Sr_2Ir_{0.9}Ru_{0.1}O_4$, (c) $Sr_2Ir_{0.9}Rh_{0.1}O_4$, (d) $Sr_2Ir_{0.84}Ru_{0.16}O_4$. (e) M_x^σ / M_y^σ is the ratio of matrix element at the X_x point to that at X_y. The black solid line is the DFT calculation. The colored markers are experimental values determined by dividing the integrated intensity of the red box in (a-d) around X_x point by that around X_y point.

Curie-Weiss temperature Θ_{CW} are plotted as a function of Rh concentration x. The magnetic order is fully suppressed at $x \sim 0.17$, below which the Curie-Weiss temperature becomes negative. Even though $\Theta_{CW} \sim -72\,K$ at $x \sim 0.4$, the magnetic order doesn't appear down to 0.3 K. Below 0.3 K, the anomalous peak is observed in the heat capacity, indicating the magnetic transition. The discrepancy between Θ_{CW} and the transition temperature at $x \sim 0.4$ suggests the strong frustration such as the competition between antiferromagnetic and ferromagnetic interactions. However, the magnetic order is not well experimentally investigated.

Reduction of spin-orbit coupling

The Rh substitution reduces the spin-orbit interaction. In contrast to the large spin-orbit interaction of $5d$ Ir $\sim 0.4\,eV$, the spin-orbit interaction of $4d$ Rh or Ru is small $\sim 0.19\,eV$. The recent ARPES study [237] demonstrated the reduction of the spin-orbit interaction, using σ-polarized light. Dipole selection rules allow the transitions from only certain orbitals, enabling to probe the orbital mixing by the spin-orbit coupling. In the experimental scattering plane, d_{xz} is an even state, which is only observable with π polarization. On the other hand, d_{xy} and d_{yz} are odd states, which are only observable with σ polarization. Since the spin-orbit coupling mixes these three states into linear combinations (J_{eff} states), the ratio of even/odd states is used to quantify the strength of the spin-orbit interaction. Figures 4.2 show the constant energy maps for (a) Sr_2IrO_4, (b) $Sr_2Ir_{0.9}Ru_{0.1}O_4$, (c) $Sr_2Ir_{0.9}Rh_{0.1}O_4$, and (d) $Sr_2Ir_{0.84}Ru_{0.16}O_4$, respectively. The maps were taken at energy so that the size of the pocket around X is the same for all the samples. The intensity around X_x point sensitively changes by Rh/Ru substitution. To estimate the strength of the spin-orbit interaction, the relation between the matrix elements and the strength of the spin-orbit interaction is calculated by tight-binding calculation. To handle the Rh substitution, a tight-binding Hamiltonian for the unit-cell including a single Ir site was
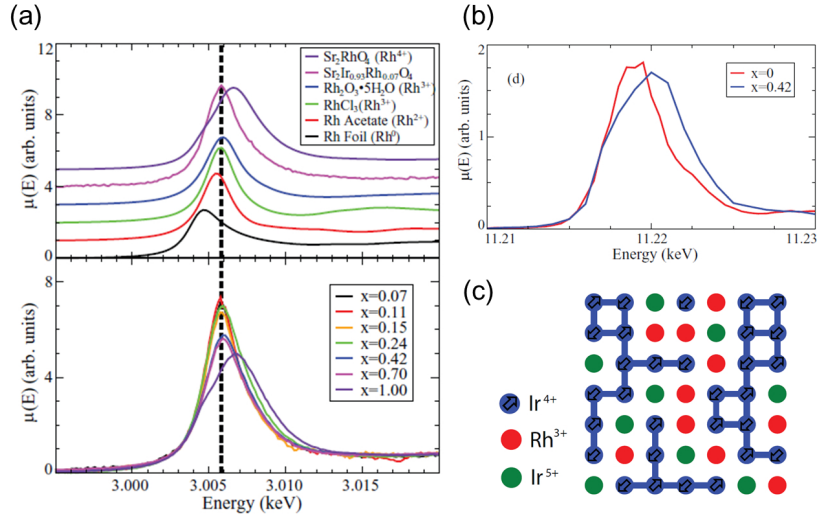
Figure 4.3: X-ray absorption spectroscopy study on $Sr_2Ir_{1-x}Rh_xO_4$ [157]. (a) X-ray absorption spectra at Rh L_3 edge and (b) at Ir L_3 edge. (c) A schematic of ionic states in $Sr_2Ir_{1-x}Rh_xO_4$ at low substitution level. Rh^{3+} and Ir^{5+} are non-magnetic.

expanded to a 64 site supercell in which several sites were randomly substituted with an impurity atom. The resulting spectral function was averaged over 200 random configurations of impurity atoms. The calculated results are plotted with a black line in figure 4.2(e). Here M_x^σ is the matrix element at X_x point and M_y^σ is that at X_y point. λ_{SOC} is the strength of spin-orbit coupling, which is estimated by the band splitting between J_{eff} states. The calculation suggests that λ_{SOC} linearly reduces with Rh substitution, as shown in the upper horizontal axis. The experimental values of M_x^σ/M_y^σ were determined by the integrated intensity of the area shown with the red box at X points. They are plotted with colored markers on the black solid line in figure 4.2(e). The horizontal positions of the markers are consistent with the nominal Rh concentrations of the samples, indicating experimental values of M_x^σ/M_y^σ are consistent with the calculation. The measurements have revealed that the Rh substitution reduces the spin-orbit interaction as calculated. However, the reduction does not explain the phase diagram of $Sr_2Ir_{1-x}Rh_xO_4$, especially the reentrant insulating state. The other effect of Rh substitution, hole doping, plays an important role.

Effective hole doping

The Rh ions in Sr_2RhO_4 adopt Rh^{4+} state. If Ir^{4+} is substituted by Rh^{4+}, the Rh substitution doesn't change the carrier concentration. However, the X-ray absorption spectroscopy study reported the presence of Rh^{3+} state in a wide range of Rh concentration $0.07 \leqq x \leqq 0.70$ [157]. The upper panel of figure 4.3(a) shows the X-ray absorption spectra at Rh L_3 edge ($p_{3/2} \rightarrow 4d$) for $x = 0.07$ and reference samples. The peak position of $x = 0.07$ coincides with that of $Rh_2O_3 \cdot 5H_2O$ and $RhCl_3$, in which the oxidation state of Rh is 3+. The other reference materials have a peak at different energies since the oxidation states are different. The results indicate that Rh ions in $x = 0.07$ adopt Rh^{3+} state rather than Rh^{4+} state. Rh^{3+} changes a vicinal Ir^{4+} to Ir^{5+} to preserve the charge
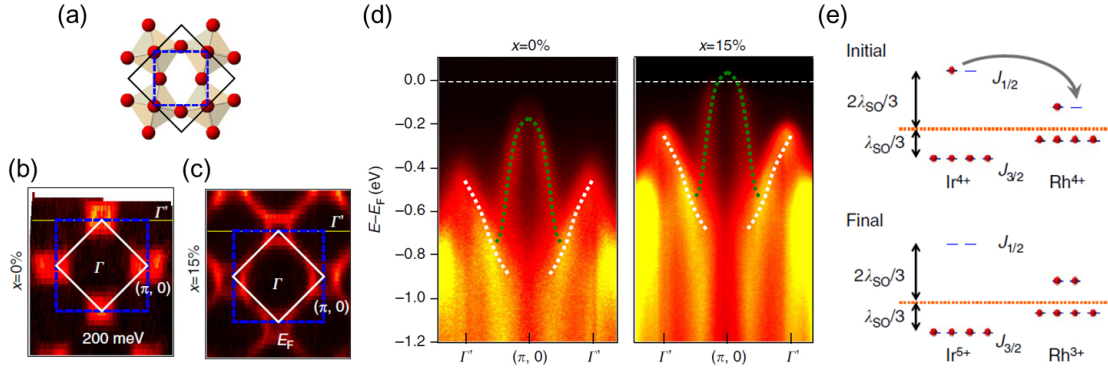
Figure 4.4: ARPES study on $Sr_2Ir_{1-x}Rh_xO_4$ [159]. (a) The IrO_2 plane of Sr_2IrO_4. The blue dotted line indicates the unit cell including a single Ir atom. The black line indicates the unit cell including two Ir atoms. (b) The constant energy surface of $x = 0$ at $200\,meV$. The blue dashed line is the Brillouin zone defined with the unit cell including a single Ir atom. (c) The constant energy surface of $x = 0.15$ at the Fermi level. (d) ARPES energy-momentum intensity for $x = 0, 0.15$ plots along $\Gamma' - (0, \pi) - \Gamma'$, which is marked by yellow lines in (b,c). (e) The simple atomic schematic of hole doping.

neutrality. Therefore, the Rh substitution also causes the shift in the peak at Ir L_3 edge ($p_{3/2} \to 5d$) as shown in figure 4.3(b). The lower panel of figure 4.3(a) shows the spectra at rhodium L_3 edge for $0.07 \leqq x \leqq 1.00$. Only the peak of $x = 1.00$ is different from the others since Rh ions are Rh^{4+} state in Sr_2RhO_4. On the other hand, the other samples, $0.07 \leqq x \leqq 0.70$, have the peak at the same energy as reference materials of Rh^{3+}. This indicates that Rh^{3+} state is dominant even at $x > 0.5$. However, all Ir ions turn into Ir^{5+} at $x > 0.5$, and there are not enough Ir ions to balance the electronic charge. Therefore, Rh^{3+} state coexists with Rh^{4+} state in the heavily substituted regime. Indeed, the peak width of $x = 0.42$ and 0.70 is significantly increased compared to $0.07 \leqq x \leqq 0.24$. The later study of X-ray absorption spectroscopy estimates the hole concentration in detail [161]. The hole concentration marks a peak at $x \sim 0.2$ and decreases by further substitution. This is consistent with the hole concentration estimated in the ARPES study [238]. This thesis focuses on the slight substitution regime, $0 \leqq x \leqq 0.12$, where Rh^{3+} states are dominant.

In the slight substitution regime $0 \leqq x \leqq 0.15$, the development of hole Fermi surface has been reported by angle-resolved photoemission (ARPES) [159]. Figure 4.4(b) is the constant energy surface of $x = 0$ at $200\,meV$. The blue dotted line is the Brillouin zone, which is defined by the unit cell indicated by the blue dashed line in figure 4.4(a). The unit cell includes a single Ir atom in the same way as that of the cuprates. However, in Sr_2IrO_4, the octahedral distortion folds the Brillouin zone into the two Ir Brillouin zone (white line). The spectral weight at $(\pi, 0)$ is the hole pocket, at which the hole-like dispersion was observed in the energy-momentum intensity plots along $\Gamma' - (0, \pi) - \Gamma'$ as shown with the dotted green line in figure 4.4(c). The top of the hole band reaches the Fermi level when $x = 0.15$, resulting in the square hole surface at $(0, \pi)$ as shown in figure 4.4(c). Those observations are consistent with the effective hole doping scenario that Rh^{3+} changes neighboring Ir^{4+} to Ir^{5+}. The ARPES study proposed how such ionic

states appear in the slight substitution regime by the simple atomic picture. Since the spin-orbit splitting of the Ir J_{eff} orbitals is much larger than the Rh one, the energy level of the Ir $J_{eff} = 1/2$ orbital can be higher than that of Rh as shown in figure 4.4(e). An electron in the $J_{eff} = 1/2$ orbital of Ir^{4+} drops to the orbital of neighboring Rh^{4+}, resulting in Rh^{3+} and Ir^{5+} states. However, the argument is based on the very simple atomic picture. To understand the ionic states, we need more studies on a model including the finite bandwidth and the Coulomb repulsion.

The ARPES study suggests that the possibility of a pseudogap opening as observed in the cuprates. In electron-doped cuprates, an electron pocket appears near $(\pi, 0)$. By increasing the carrier concentration, electron pockets evolve into a large hole-like Fermi surface centering around (π, π) [239, 240]. At low doping levels, the Fermi surface is absent around $(\pi/2, \pi/2)$, which is regarded as a pseudogap opening. In $Sr_2Ir_{1-x}Rh_xO_4$, the spectral weight around $(\pi, 0)$ seems to come from a square hole pocket, but reference [159] points out that it may consist of four Fermi arcs. Fermi arcs perpendicular to the $\Gamma - (\pi, 0)$ direction are a part of Fermi surface centered around the Γ point, while those parallel to the $\Gamma - (\pi, 0)$ direction are a part of the folded Fermi surface centered around the Γ' point. They reported that the energy-distribution curves are different between non-folded Fermi arcs and the folded ones. The later ARPES study [238] also reported the lack of density of states at E_F, but they did not observe any difference between the folded and the non-folded sheets. Further investigation is required for understanding the pseudogap in $Sr_2Ir_{1-x}Rh_xO_4$.

4.1.2   Magnetic orders

Figure 4.5(a) shows the phase diagram of $Sr_2Ir_{1-x}Rh_xO_4$ for the slight substitution regime, $0 \leqq x \leqq 0.25$. The black squares indicate the Néel transition temperatures, T_{N1} and T_{N2}, determined by the magnetization measurements [158]. T_{N1} marks an appearance of the net ferromagnetic moment. T_{N2} marks a dramatic increase of magnetization below T_{N1}. The red squares indicate T_{N1} and T_{N2} determined by resonant magnetic X-ray scattering measurements [157]. Figure 4.5(b) shows the temperature dependence of the $(0, 1, 21)$ magnetic Bragg peak intensity at Ir L_3 edge for $x = 0.07$ and 0.11. T_{N1} marks the temperature at which the magnetic Bragg peak appears. T_{N2} marks the temperature below which the peak intensity dramatically increases. The T_{N1} and T_{N2} determined by the X-ray scattering are consistent with those determined by the magnetization. Also, the temperature dependence of the peak intensity closely tracks that of the bulk magnetization. Figure 4.5(c) shows the momentum scan through the $(0, 1, 21)$ peak of $x = 0.07$. The peak width at $T_{N2} < T < T_{N1}$ is broader than that below T_{N2}, indicating the shorter correlation length. The full width half maximum Γ_{obs} represents a convolution of the intrinsic peak width Γ_{int} and the instrumental resolution function Γ_{res}. The intrinsic peak width is inversely proportional to the magnetic correlation length through the relation $\xi = d/\pi\Gamma_{int}$. The broader peak width indicates the shorter correlation length. The weak intensity and the shorter correlation length at $T_{N2} < T < T_{N1}$ suggest that the magnetic order is a short-range order at $T_{N2} < T < T_{N1}$ and a long-range order below T_{N2}. The estimated in-plane correlation length is $\xi_{ab} \sim 1500\,\text{Å}$ for $x = 0.07$ and $\xi_{ab} \sim 1400\,\text{Å}$ for $x = 0.11$. They are substantially longer than the average distance between Rh atoms ($\sim 95\,\text{Å}$ and
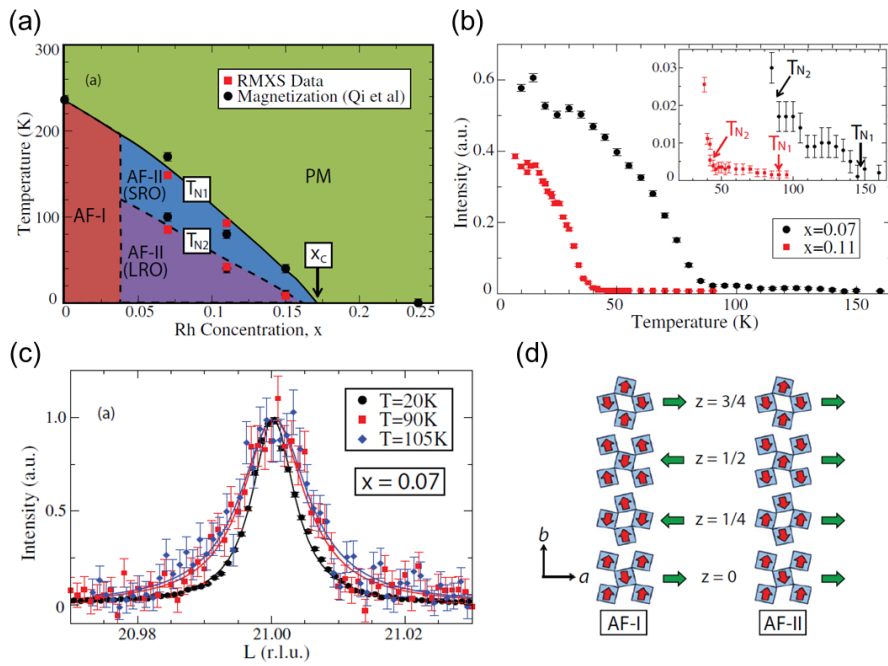
Figure 4.5: Resonant magnetic x-ray scattering measurements [157]. (a) Phase diagram for $0 \leqq x \leqq 0.25$. (b) Temperature dependence of the $(0, 1, 21)$ magnetic Bragg peak intensity measured at the iridium L_3 edge for $x = 0.07$ and 0.11. (c) Reciprocal space scans through the $(0, 1, 21)$ magnetic Bragg peak of $x = 0.07$ at 20, 90, 105 K. (d) Schematics of magnetic order in AF-I and AF-II. The green arrows represent the net magnetic moment of each Ir-O layer.

$60\,\text{Å}$, respectively). The detailed measurements of the magnetic structure factor and the azimuthal angle dependence determined the spin configuration, which is different between $x = 0$ and $x = 0.07$. They are labeled by AF-I and AF-II. As shown in figure 4.5(d), each IrO_2 layer has a finite net moment. While the net moment cancels among layers in AF-I at zero field, it doesn't cancel in AF-II. The magnetic orders are fully suppressed at $x_c \sim 0.17$.

In both AF-I and AF-II, dispersive magnon-dispersion was observed at $10\,\text{K}$ in resonant inelastic X-ray scattering measurements [241]. The magnon mode hardens with increasing hole carrier concentration at $x < 0.17$, which has been also observed in electron-doped cuprates [242, 243]. The similarity in the spin dynamics may result from the reversal of electron-hole asymmetry between doped iridates and cuprates.

The suppression of the antiferromagnetic order is not likely due to the collapse of $J_{eff} = 1/2$ state by the Rh substitution. Resonant magnetic X-ray scattering measurements were also performed on $Sr_2Ir_{1-x}Rh_xO_4$. As well as Sr_2IrO_4 [114], the magnetic peak intensity at iridium L_3 edge is > 200 times as large as the intensity at L_2 edge in $x = 0.07$ and 0.11 [157]. It suggests $J_{eff} = 1/2$ state is robust against the rhodium substitution. However, several theoretical calculations point out that the magnetic intensity at the L_2 edge may vanish regardless of the t_{2g} splitting when Ir^{4+} magnetic moments are aligned within the ab-plane [126, 244]. The case of Mn substitution provides the evidence for $J_{eff} = 1/2$ state because the Ir^{4+} magnetic moments align perpendicular to the IrO_2 plane in $Sr_2Ir_{1-x}Mn_xO_4$. The magnetic intensity at L_2 edge also vanishes in this material [245]. The $3d$ Mn substitution reduces the spin-orbit interaction much more than Rh substitution. Although the interpretation of the resonant X-ray scattering data is controversial, the analogy with Mn substitution suggests that $Sr_2Ir_{1-x}Rh_xO_4$ also has a $J_{eff} = 1/2$ state in the slight substitution regime. The robustness of $J_{eff} = 1/2$ state is also proposed theoretically by LDA+U calculation [160].

The disorder of octahedral rotation is also unlikely to drive the suppression of the magnetic order. While the IrO_6 octahedra rotate about the c-axis by $11 - 12°$ in Sr_2IrO_4, the RhO_6 octahedra rotate by $9.6 - 9.7°$ in Sr_2RhO_4. The mismatch of the rotation can induce disorder in $Sr_2Ir_{1-x}Rh_xO_4$. To estimate the disorder, the $(1, 2, 21)$ superlattice Bragg peak was investigated by the high-resolution non-resonant X-ray diffraction measurements [157]. Compared to the isostructural Sr_2RuO_4 or La_2CuO_4, the octahedral rotation in Sr_2IrO_4 extends the unit cell by $\sqrt{2} \times \sqrt{2}$ in the ab-plane and doubles it along the c-axis. The $(1, 2, 21)$ superlattice peak arises due to the octahedral rotation, the width of which provides the correlation length associated with the octahedral rotation. The width of the superlattice Bragg peak $(1, 2, 21)$ is essentially the same as that of the structural Bragg peak $(0, 0, 24)$ in both $x = 0$ and $x = 0.24$. On the other hand, the superlattice Bragg peak becomes significantly broader than the Bragg peak in $x = 0.42$, indicating reduced octahedral correlation length and increased rotational disorder. This suggests that the rotational disorder is not significant at $x \leqq 0.24$.

Another explanation is provided by a percolation theory. The site percolation well explains the magnetism in a doped cuprate $La_2Cu_{1-x}(ZnMg)_xO_4$ [246]. Given that $Sr_2Ir_{1-x}Rh_xO_4$ can be described by a local moment picture, the spin-only percolation threshold is $x_p = 0.407$ [157]. The substitution of Ir^{4+} by Rh^{3+} ions introduces two non-magnetic ions, Ir^{5+} and Rh^{3+}. Thus, the percolation threshold should be compared with
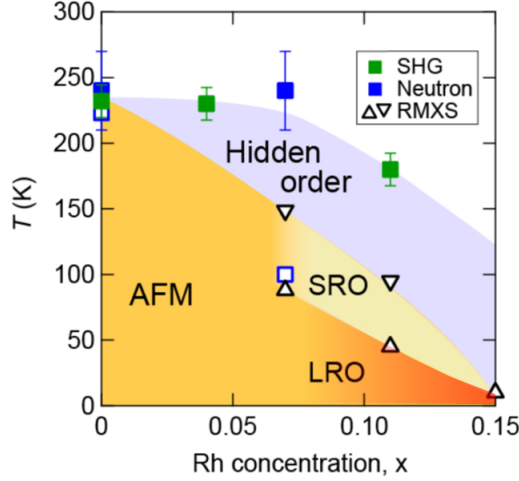
Figure 4.6: Phase diagram of $Sr_2Ir_{1-x}Rh_xO_4$ ($0 \leqq x \leqq 0.15$). The yellow area is antiferromagnetic order whose onset temperatures (marked with triangles) are determined by resonant magnetic X-ray scattering measurementsv [241]. Dark and pale yellow areas are respectively long-range and short-range magnetic orders. The blue area is a hidden order phase that breaks inversion and time-reversal symmetries. The onset temperatures of inversion symmetry breaking were determined by second harmonic generation measurements [123], marked with green square. The onset temperatures of time-reversal symmetry breaking were determined by spin-polarized neutron scattering measurements [162], marked with blue squares.

$2x_c \sim 0.34$. It is pointed out in reference [157] that the slight overestimation of x_p may come from the strong entanglement of the spin and orbital degrees of freedom.

4.1.3 Hidden order

$Sr_2Ir_{1-x}Rh_xO_4$ has recently attracted attention after the inversion and time-reversal symmetry breakings were observed in the vicinity of the antiferromagnetic order. Magnetic orders which break those symmetries have been observed in systems with strong spin-orbit coupling. However, in $Sr_2Ir_{1-x}Rh_xO_4$, those symmetry breakings were also observed outside the antiferromagnetic phase of $Sr_2Ir_{1-x}Rh_xO_4$. No previous studies report the presence of magnetic orders in the region. A charge order which breaks those symmetries has not been revealed in any systems.

Figure 4.6 is the phase diagram of $Sr_2Ir_{1-x}Rh_xO_4$ ($0 \leqq x \leqq 0.15$). The dark and pale yellow areas are respectively the long-range and short-range antiferromagnetic phases. The onset temperatures of the antiferromagnetic orders are marked with downward triangles, at which the magnetic Bragg peak appears in resonant magnetic X-ray measurements [241]. The upward triangles indicate the boundary between the regions of long-range and short-range magnetic orders, at which the magnetic Bragg peak intensity abruptly increases. The green squares represent the onset temperatures of inversion symmetry breaking observed in optical SHG measurements [123]. The blue squares represent the onset temperatures of time-reversal symmetry breaking observed in spin-polarized neutron scattering [162]. Those symmetries are broken well above the Néel temperatures when $x > 0$. The region
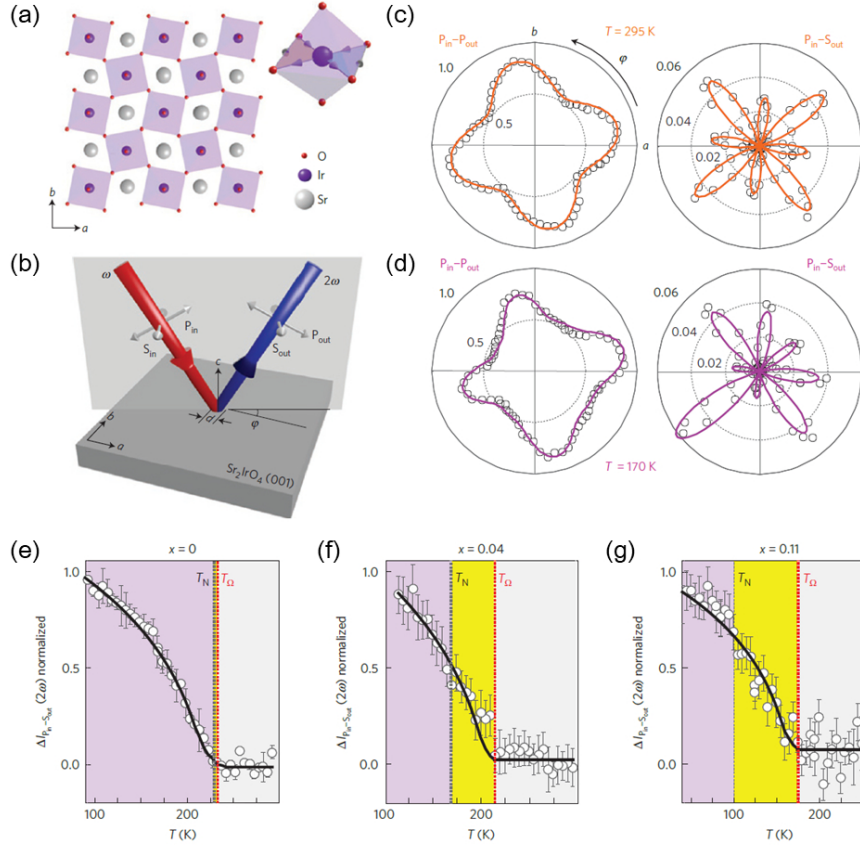
Figure 4.7: Optical SHG study on $Sr_2Ir_{1-x}Rh_xO_4$ [123]. (a) Top view of the Ir-O plane. The a and b axes are defined along Ir-Sr-Ir direction, not along Ir-O-Ir direction. (b) Measurement setup. S(P) represents the polarization perpendicular (parallel) to the scattering plane. The spot size d is $< 100\,\mu$m. ϕ is an azimuthal angle between the a-axis and the scattering plane. (c,d) The ϕ dependence of SHG reflection P_{out} and S_{out} for $x = 0$ at (c) 295 K and (d) 170 K. (e-g) Temperature dependence of SHG intensity $S_{out}(T) - S_{out}(RT)$ at $\phi = 78°$ in (e) $x = 0$, (f) $x = 0.04$, (g) $x = 0.11$. T_Ω is the onset temperature of finite S_{out} intensity. T_N is antiferromagnetic transition temperature determined by magnetization measurements.

between the Néel temperature and the onset temperature of those symmetry breakings is called the hidden order. Here we review the two measurements, which demonstrate those symmetry breakings.

The hidden order was firstly suggested by the optical second-harmonic generation (SHG) measurements [123]. SHG is sensitive to inversion symmetry breaking because the leading-order electric dipole contribution to SHG is a third-rank susceptibility tensor, which is allowed only in a system without inversion symmetry. They performed a rotational anisotropy SHG experiment to discuss the rotational symmetry together. The measurement setup is shown in figure 4.7(b). ϕ is an azimuthal angle between the scattering plane and the a-axis. The incident beam was polarized parallel to the scattering plane, which is labeled by P_{in}. The reflected SHG beam was analyzed in both polarizations, parallel and perpendicular to the scattering plane. The polarizations are labeled by

P_{out} and S_{out}, respectively. Figure 4.7(c) shows the ϕ dependence of the SHG intensity at 295 K, which is consistent with the previous study [113]. As the crystal has tetragonal symmetry, both P_{out} and S_{out} exhibit the four-fold rotational symmetry. The peaks and valleys of the patterns are away from the high symmetry directions of the crystal. The patterns are inconsistent with the symmetry of D_{4h}, which has the C_2 rotational symmetry around the a, b axes and the diagonal direction. The neutron study [122] points out that the crystal violates the glide symmetries, which results in the symmetry reduction from $I4_1/acd$ to $I4_1/a$ (from D_{4h} to C_{4h} in the point group). The SHG study [113] proposes that the symmetry reduction originates in the different octahedral distortion between an octahedron rotating clockwise and the other anticlockwise.

On the other hand, the patterns at 170 K violate the C_4 rotational symmetry about the c-axis as shown in figure 4.7(d). The rotational symmetry is reduced down to C_1, which violates the inversion symmetry. Depending on the spot position, four types of the pattern were observed, which rotate by 90° each other. The domain size is $\sim 100\,\mu$m. The results indicate that the inversion symmetry is spontaneously broken at 170 K. Figure 4.7(e) shows the temperature dependence of $S_{out}(T) - S_{out}(RT)$ at $\phi = 78°$. T_Ω indicates the onset temperature of finite intensity. T_Ω is comparable to T_N, which is the Néel temperature determined by the magnetization measurements. On the other hand, T_Ω is much higher than T_N in $x = 0.04$ and $x = 0.11$. Those results suggest that there exists a charge order which breaks inversion and rotational symmetry at $T_N < T < T_\Omega$. The charge order is called the hidden order. However, the results do not provide the bulk evidence for those symmetry breakings, since the SHG signal includes the surface contribution, which is hardly indistinguishable from the bulk one. The bulk evidence for the symmetry breaking is necessary for determining the order parameter symmetry. It should be also studied why the mirror plane in the patterns is away from the high symmetric direction.

The SHG response in the hidden order is similar to that in the pseudogap state of the cuprates. The symmetry reduction is associated with loop current orders. In the cuprates, the loop current scenario has attracted attention after the experimental observation of the intra-unit-cell magnetic order. The similarities between Sr_2IrO_4 and the cuprates motivate the investigation of the intra-unit-cell magnetic order in $Sr_2Ir_{1-x}Rh_xO_4$.

Two years later the SHG study, the spin-polarized neutron study [162] reported the intra-unit-cell magnetic order in the hidden order as observed in the pseudogap phase of the cuprates. The spin-polarized neutron scattering is a powerful probe of magnetic scattering. Nuclei cannot flip the neutron spin but magnetic moments can. The appearance of magnetic order can induce the difference between spin-flipped scattering and non-spin-flipped scattering. As shown in figure 4.8(a,b), the Bragg peak $\boldsymbol{Q} = (1, 1, 2)$ was investigated because it corresponds to the $(1, 0, 2)$ peak of cuprates, at which the intra-unit-cell magnetic order was observed. The polarization is $\boldsymbol{P} \parallel \boldsymbol{Q}$ so that the full magnetic scattering can appear in the spin-flipped channel in the polarization geometry [203].

Figure 4.8(c) shows the temperature dependence of the spin-flipped scattering intensity I_{SF} and the background I_{NSF}/FR_0 for $x = 0$. The background signal comes from the polarization leakage due to the imperfect polarization of the incident beam. The polarization leakage ratio $1/FR_0$ was determined by the I_{SF}/I_{NSF} ratio in $(2, 2, 0)$ Bragg peak, where the magnetic scattering was small enough and the spectrometer geometry was kept similar to $\boldsymbol{Q} = (1, 1, 2)$. I_{SF} deviates from the background below $T_{mag} \sim 240 \pm 30$ K. T_{mag} is com-
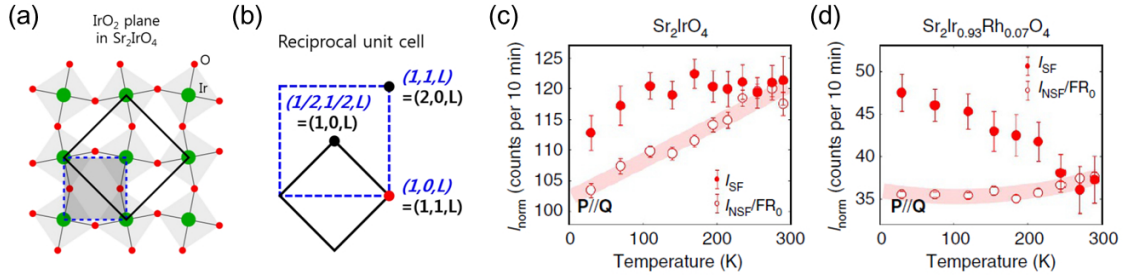
Figure 4.8: Spin-polarized neutron scattering measurements on $Sr_2Ir_{1-x}Rh_xO_4$ [162]. (a, b) The crystal structure and the reciprocal unit cell of Sr_2IrO_4 (black solid line) and the cuprates (blue dashed line). (c,e) Temperature dependence of the spin-flipped intensity I_{SF} (filled circles) and the background I_{NSF}/FR_0 (open circles) at the $\boldsymbol{Q} = (1, 1, 2)$ Bragg peak for (c) $x = 0$ and (e) $x = 0.07$. The polarization $\boldsymbol{P}$ is parallel to the scattering vector $\boldsymbol{Q}$.

parable to the Néel transition temperature $T_N = 232\,\text{K}$. T_N was determined by the onset temperature of the magnetic Bragg peak $(1, 0, 2)$. The deviation of I_{SF} from the background is also observed in $x = 0.07$. However, the onset temperature $T_{mag} \sim 240 \pm 30\,\text{K}$ is much higher than $T_N \sim 100\,\text{K}$. At $T_N < T < T_{mag}$, the magnetic scattering appears on $\boldsymbol{Q} = (1, 1, 2)$ but no additional peak appears other than the nuclear Bragg peaks. The results indicate that the intra-unit-cell magnetic order exists at $T_N < T < T_{mag}$. T_{mag} is roughly consistent with T_Ω in the SHG study [123] as shown in figure 4.6. They suggest that the hidden order breaks inversion, rotational, and time-reversal symmetry without violating the translational symmetry.

The nature of the hidden order is still elusive. Although the previous studies suggest the presence of the hidden order phase, they still lack the thermodynamic evidence for the phase transition. Furthermore, the inversion and rotational symmetry breakings are observed only by the surface probe. It is important to observe those symmetry breakings with the bulk thermodynamic quantities.

4.2 Magnetic torque measurement of $Sr_2Ir_{1-x}Rh_xO_4$

To study the phase transition of the hidden order and reveal the order parameter symmetry, we have performed field-angle resolved magnetic torque measurements on $Sr_2Ir_{1-x}Rh_xO_4$. Since the magnetic torque is a thermodynamic quantity sensitively probing the magnetic anisotropy, it has probed a small magnetic anisotropy arising from a hidden order phase transition accompanied by rotational symmetry breaking.

4.2.1 Sample preparation

Crystal growth

Single crystals of $Sr_2Ir_{1-x}Rh_xO_4$ were prepared by Gang Cao in the University of Colorado Boulder, using flux techniques. The crystals were grown in Pt crucibles from off-stoichiometric quantities of IrO_2, RhO_2, $SrCO_3$ and $SrCl2$ [141, 159]. We obtained small
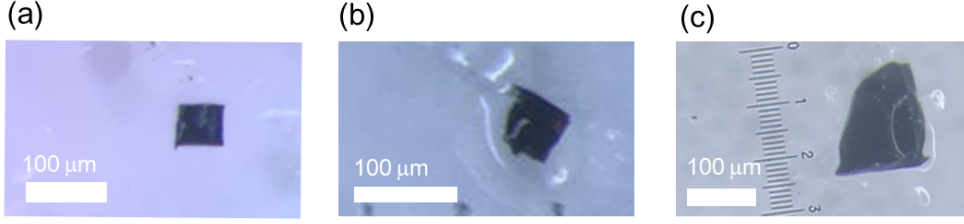
Figure 4.9: Photos of crystals used in magnetic torque measurements. (a) $x = 0$, (b) $x = 0.048$, (c) $x = 0.095$.

Table 4.1: Volume of crystals used for torque measurements.

Rh concentration	Volume
$x = 0$	$2.5 \times 10^{-14}\,\mathrm{m^3}$
$x = 0.048$	$7.2 \times 10^{-14}\,\mathrm{m^3}$
$x = 0.095$	$2.7 \times 10^{-13}\,\mathrm{m^3}$

flakes during the ultrasonic cleaning process of a large single crystal and used them in magnetic torque measurements. Figures 4.9(a-c) are photos of single crystals with various substitution levels, which were used for magnetic torque measurements. The sample volume is listed in table 4.1. We did not perform the XRD measurements on those crystals but on $x = 0.076$. The crystal was tetragonal within the error of 0.15%.

Determination of T_N

To determine the Néel temperature, we performed magnetization measurements, using Quantum Design's MPMS3 system. Crystals used for magnetization measurements were obtained from the same batch as crystals used for the torque measurements. The crystal size of $x = 0$, 0.048, and 0.095 is respectively $\sim 1 \times 0.5 \times 0.15\,\mathrm{mm}$, $\sim 1.7 \times 0.4 \times 0.15\,\mathrm{mm}$, and $\sim 1.4 \times 0.5 \times 0.1\,\mathrm{mm}$ Figures 4.10(a–c) represent the temperature dependence of the magnetization under the in-plane field of 0.1, 0.2, and 0.3 T. The solid and dotted lines represent field-cool and zero-field-cool, respectively. For all the samples, large magnetization appears as a result of a long-range magnetic ordering. The onset temperatures T_N^M are consistent with the previous studies [158, 241]. T_N^M=250 K, 170 K, and 70 K for $x = 0$, 0.048, and 0.095. The magnetization curves are dependent on the field size in $x = 0$ because the magnetic structure changes by the weak field [114]; the net moment of each IrO_2 layer is polarized by the field. It should be also noted that T_N^M of $x = 0.095$ is roughly consistent with the Néel transition temperature predicted from the phase diagram in reference [241]. The short-range order sets in at a higher temperature than T_N^M in $x = 0.095$.

Determination of the axis direction

The crystal axes were determined by the magnetic torque measurements in the antiferromagnetic phase. The previous study on Sr_2IrO_4 revealed the torque response in the antiferromagnetic phase [247]. In the study, the torque was measured at 215 K, which
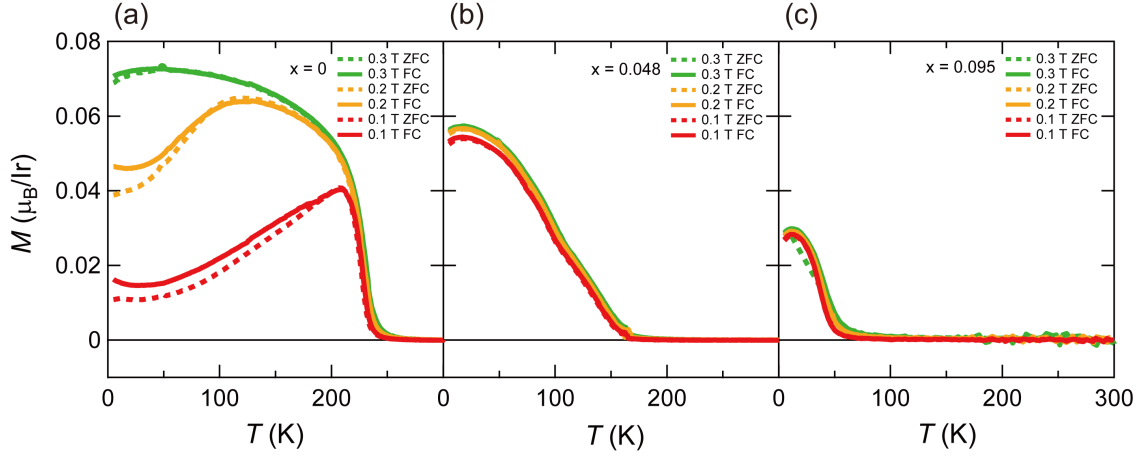
Figure 4.10: (a–c) Temperature dependence of the magnetization for $x = 0$, 0.048, and 0.095, respectively. The dotted and solid lines respectively represent magnetization measured in zero field cool and field cool state. The magnetic field was applied perpendicular to the c-axis.
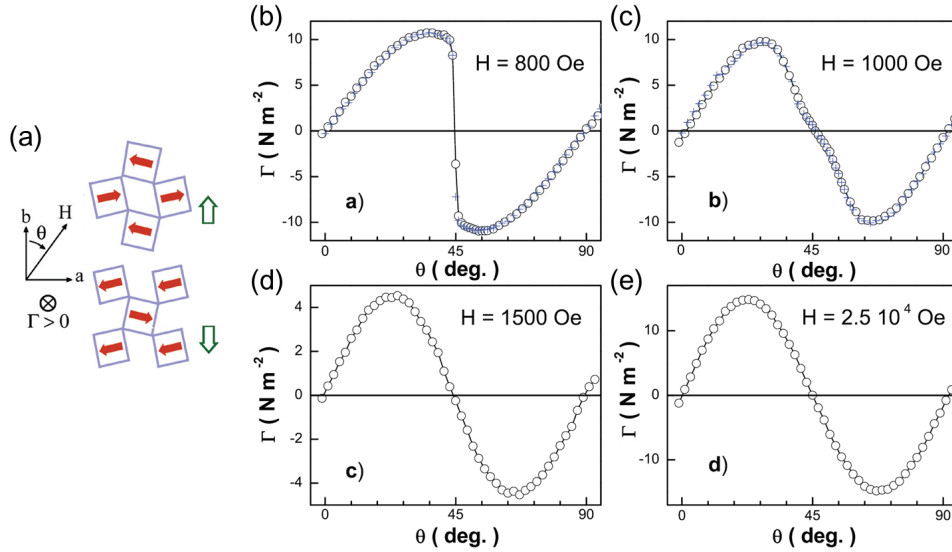

Figure 4.11: The in-plane torque measurements in the antiferromagnetic phase of Sr_2IrO_4 [247]. (a) The configuration of the magnetic moments in the antiferromagnetic phase. The red arrows represent the spin configuration in the antiferromagnetic order of Sr_2IrO_4. The green arrows are the net moment of each layer. The torque Γ, which is the rotation around the c-axis, was measured. (b–e) The field-angle dependence of the torque Γ at 215 K under the field of 800, 1000, 1500, and 2.5×10^4 Oe. The field was applied within the ab-plane. θ is the field-angle from the b-axis.

is sufficiently below the Néel transition temperature. Figure 4.11(a) shows the magnetic moment configuration in the antiferromagnetic phase. The red arrows represent magnetic moments localized on Ir sites, and the green arrows are the net moments of each layer. The magnetic field was applied within the ab-plane. The combination of the in-plane magnetic moments and the in-plane field induces the torque along the c-axis. Figures 4.11(b–e) show the field-angle θ dependence of the magnetic torque Γ. θ is the azimuthal angle from the b-axis. The torque is periodic as a function of θ with a period of 90°. At low fields, $H < 1000$ Oe, the torque jumps around 45 degrees. On the other hand, the torque curves are almost sinusoidal at higher fields, $H > 1000$ Oe. The torque signal reflects the spin-flop transition; the antiferromagnetic domains flop to a configuration in which the net moments are parallel to the field. Under the sufficiently large field, the antiferromagnetic domains nearly rigidly follow the applied field and the torque signal is very close to sinusoidal. To describe the four-fold sinusoidal torque curves, reference [248] provides the phenomenological expression of the free energy F_s, consisting of a magnetocrystalline anisotropy term and a Zeeman term.

$$F_s = \sum_{l=1,2} -K_4 \cos(4 \arccos(\boldsymbol{m}_l \cdot \boldsymbol{a})) - \boldsymbol{m}_l \cdot \boldsymbol{B} \tag{4.1}$$

The former term locks the net moment of each layer $\boldsymbol{m}_l$ along the axis direction $\boldsymbol{a}$. $l = 1, 2$ labels the adjacent two layers. The microscopic origin of the momentum locking is discussed in reference [124]. The F_s provides four-fold sinusoidal torque curves. However, the interlayer coupling of the net moment, $F_i = J_\perp \boldsymbol{m}_1 \cdot \boldsymbol{m}_2$, is also necessary for capturing the torque signal in the entire field range.

In the torque measurements on $Sr_2Ir_{1-x}Rh_xO_4$, we determined the axis direction by the magnetic torque in the antiferromagnetic phase. We applied the in-plane field of 4 T, which is much larger than the critical field to flop the antiferromagnetic domains. Therefore, the magnetic torque arising from the antiferromagnetic order is to be perfectly sinusoidal as a function of the field angle: $\propto \sin(4 \cdot 2\pi\phi/360)$. Here ϕ is the azimuthal angle from the a-axis. The torque curves were firstly fitted with $\sum_{n=0}^{8} A_{n\phi} \sin(2n\pi(\phi' - \phi'_n)/360)$. $A_{n\phi}$ and ϕ'_n are the fitting coefficients. ϕ' is the azimuthal angle of the magnetic field in the measurement setup. Below T_N, the amplitude of the four-fold sinusoidal curve $A_{4\phi}$ increased, and its phase ϕ'_4 saturated to ϕ'^0_4; $\phi'_4 \to \phi'^0_4 (T \to 0)$. According to reference [247], ϕ'^0_4 corresponds to the a-axis direction. Then we redefined the axis direction so that $\phi_4 \sim 0$ at sufficiently low temperatures; $\phi \equiv \phi' - \phi'^0_4$, $\phi_n \equiv \phi'_n - \phi'^0_4$.

4.2.2 In-plane magnetic anisotropy

The field-angle dependence of magnetic torque was measured on $x = 0$, $x = 0.048$, and $x = 0.095$. The sample alignment and the field orientation are shown in figure 4.12(a). Since the crystals were obtained by the ultrasonic cleaning, their shape was plate-like and their largest facet was parallel to the ab-plane. Due to such a crystal geometry, we mounted the crystal on a cantilever with very small misalignment. Here we assumed the rotation axis of the cantilever was parallel to the c-axis of the crystal. The magnetic field was applied within the ab-plane. ϕ is the field angle from the a-axis, the direction of which was determined by the four-fold sinusoidal torque curves in a sufficiently low temperature, which is typically below 40 K (section 4.2.1).
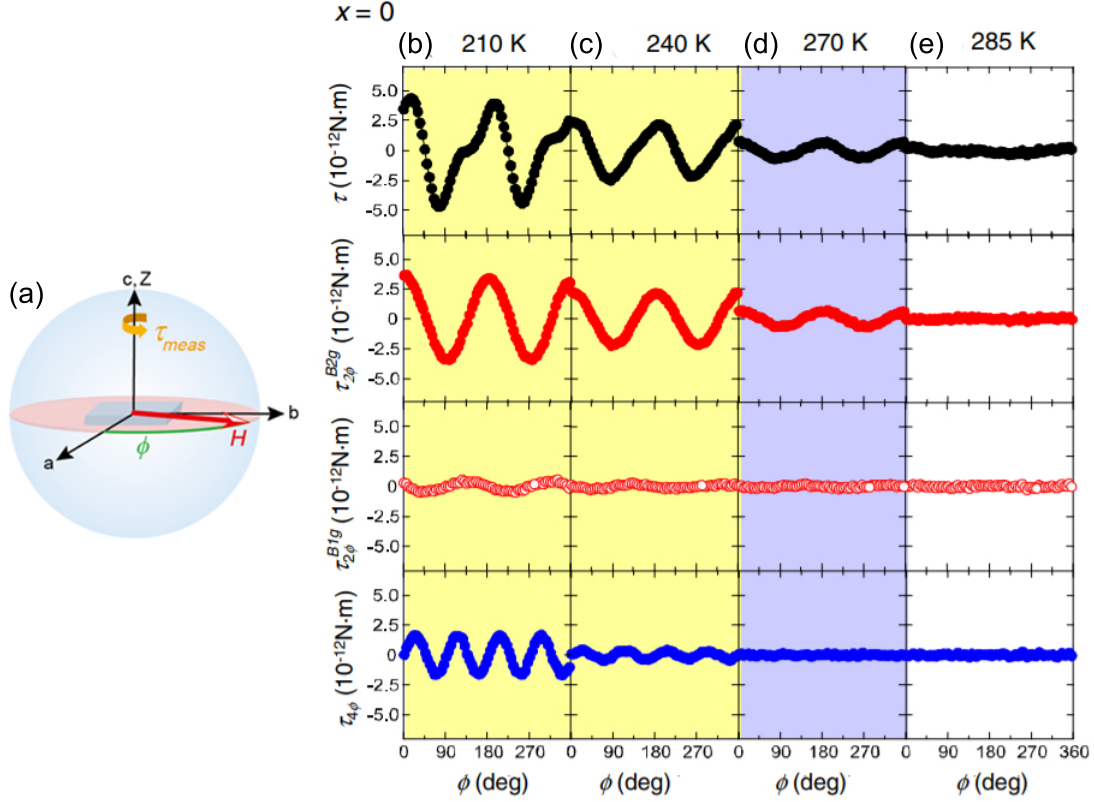
Figure 4.12: (a) The sample alignment and the field orientation in the torque measurements on $Sr_2Ir_{1-x}Rh_xO_4$. The magnetic field of $4\,T$ was applied within the ab-plane. ϕ is the field angle from the a-axis. We assumed $c \parallel Z$ since the largest facet ($\parallel ab$) of crystal was aligned normal to the Z-axis. The torque measurements and the Fourier analysis were performed on $x = 0$ at (b) $210\,K$, (c) $240\,K$, (d) $270\,K$, and (e) $285\,K$ [249]. The intrinsic magnetic torque τ, the two-fold sinusoidal components $\tau_{2\phi}^{B2g}$, $\tau_{2\phi}^{B1g}$, and the four-fold sinusoidal component $\tau_{4\phi}$ are plotted as a function of the field-angle ϕ.

As discussed in section 2.3, the raw torque signal τ_{raw} exhibits two-fold oscillation as a function of the field-angle ϕ even at room temperature. This is the extrinsic signal, τ_{ext}, possibly arising from the anisotropic magnetoresistance of the piezo resistors because any two-fold oscillations are not allowed in a tetragonal system. We determined the extrinsic signal $\tau_{ext} = A_{ext} \sin(4\pi(\phi - \phi_{ext})/360)$ by averaging the two-fold oscillation near the room temperature. Near the room temperature, ϕ_{ext} was temperature-independent. ϕ_{ext} was different among cantilevers and away from the high-symmetry direction of the crystal. A_{ext} was also nearly temperature independent, but some cantilevers exhibit a slight temperature drift of A_{ext} as discussed in section 2.3. The former case was in $x = 0$ and $x = 0.095$, and the latter case occurred in $x = 0.048$. To determine the temperature dependence of A_{ext} in $x = 0.048$, A_{ext} was fitted with a linear function of temperature near the room temperature. The intrinsic magnetic torque τ was calculated by $\tau \equiv \tau_{raw} - \tau_{ext}$.

The intrinsic magnetic torque of $x = 0$ is plotted as a function of the field-angle ϕ in Figures 4.12(b–e). Since the misalignment was negligible, $\tau \approx \tau_c$. As shown in figure 4.12(e), τ is isotropic at $285\,K$. On the other hand, two-fold oscillations appear in τ at 270,
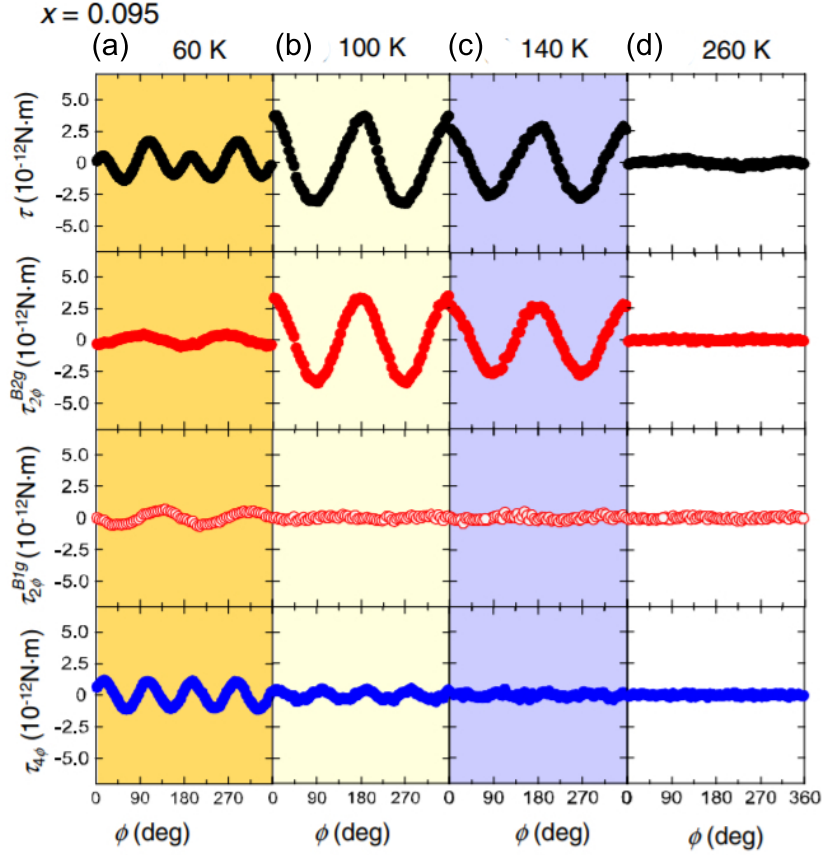
Figure 4.13: The torque measurements and the Fourier analysis are performed on $x = 0.095$ at (a) 60 K, (b) 100 K, (c) 140 K, and (d) 260 K [249]. The field-angle dependence of magnetic torque under the in-plane field of 4 T. The magnetic torque τ, the two-fold sinusoidal components $\tau_{2\phi}^{B2g}$, $\tau_{2\phi}^{B1g}$, and the four-fold sinusoidal component $\tau_{4\phi}$ are plotted as a function of the field-angle ϕ.

240, and 210 K, as shown in figures 4.12(b–d). The appearance of the two-fold oscillation indicates the symmetry reduction from C_4 to C_2. In the antiferromagnetic phase, at 240 and 210 K, τ exhibits distortion from perfect sinusoidal curves. The distortion arises from the in-plane four-fold oscillations due to the development of the long-range magnetic order [247].

We performed Fourier analysis on τ to separate the two-fold oscillation and the four-fold oscillation. τ was fitted with $\sum_{n=0}^{8} A_{n\phi} \sin(2n\pi(\phi + \phi_n)/360)$. In a range of measured temperature, 10–300 K, only the Fourier components $n = 2, 4$ were finite. The other components were negligibly small. The two-fold sinusoidal component $\tau_{2\phi}$ was extracted.

$$\tau_{2\phi} = \tau - \sum_{n=0, n\neq 2}^{8} A_{n\phi} \sin(2n\pi(\phi + \phi_n)/360) \tag{4.2}$$

$\tau_{2\phi}$ were again fitted with $A_{2\phi}^{B2g} \cos(4\pi\phi/360) + A_{2\phi}^{B1g} \sin(4\pi\phi/360)$. They are respectively labeled with B_{1g} and B_{2g}, which are irreducible representations of D_{4h} group. As shown in table 5.3, among the irreducible representations, only B_{1g}, B_{2g}, B_{1u}, and B_{2u} have the in-plane C_2 symmetry. The basis functions are listed in table 5.4. The quadratic terms
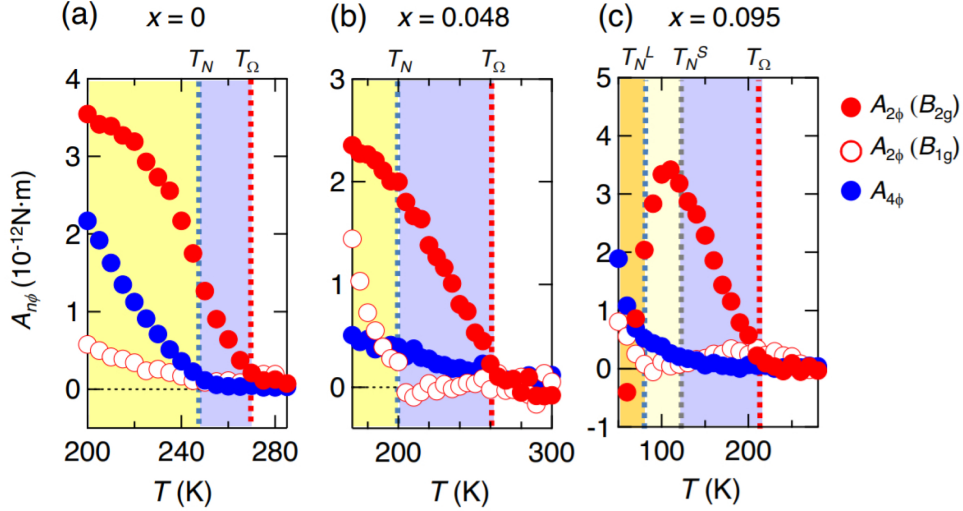
Figure 4.14: $A_{n\phi}$ are plotted as a function of temperature for (a) $x = 0$, (b) $x = 0.048$, (c) $x = 0.095$ [249]. The amplitudes of the two-fold sinusoidal components, $A_{2\phi}^{B2g}$ and $A_{2\phi}^{B1g}$, are plotted with the red filled and open circles, respectively. The amplitude of the four-fold sinusoidal components, $A_{4\phi}$, is plotted with the blue circles. The red dotted lines indicate the onset temperature of finite $A_{2\phi}^{B2g}$ T_Ω. The blue dotted lines indicate T_N or T_N^L, which is the onset temperature of finite $A_{2\phi}^{B1g}$. The gray dotted line indicates T_N^S, below which the short-range magnetic order is expected in the phase diagram (Figure 4.16). The sign of $A_{2\phi}^{B1g}$ is inversed only in (c).

of magnetic field in the free energy can cause the two-fold oscillation in magnetic torque. When $H_z = 0$, the quadratic functions are only $H_x^2 - H_y^2$ in B_{1g} and H_xH_y in B_{2g}.

Figure 4.12(b–e) shows the two-fold sinusoidal components, $\tau_{2\phi}^{B2g}$ and $\tau_{2\phi}^{B1g}$, and the four-fold sinusoidal components $\tau_{4\phi}$. Their definitions are,

$$\tau_{2\phi}^{B2g} \equiv \tau_{2\phi} - A_{2\phi}^{B1g} \sin(2\pi\phi/360) \tag{4.3}$$

$$\tau_{2\phi}^{B1g} \equiv \tau_{2\phi} - A_{2\phi}^{B2g} \sin(2\pi\phi/360) \tag{4.4}$$

$$\tau_{4\phi} \equiv \tau - \sum_{n=0,n\neq4}^{8} A_{n\phi} \sin(2n\pi(\phi + \phi_n)/360) \tag{4.5}$$

The analysis demonstrates that the two-fold oscillations are governed by B_{2g} component, $\tau_{2\phi}^{B2g}$, at 270 K, indicating $\chi_{aa} = \chi_{bb}$ and $\chi_{ab} \neq 0$ (Equation 2.12). At 240 K and 210 K, $\tau_{2\phi}^{B2g}$ develops largely. In addition to the large B_{2g} component, the two-fold oscillations include a small B_{1g} component. The B_{1g} component possibly arises from the development of the magnetic order. However, we cannot exclude the possibility that the assumption for the temperature dependence of τ_{ext} fails at low temperatures. At 240 K and 210 K, $\tau_{4\phi}$ develops, which is consistent with the previous study in the antiferromagnetic region [247]. The same measurements and analyses were also performed at other temperatures. $A_{2\phi}^{B2g}$, $A_{2\phi}^{B1g}$, and $A_{4\phi}$ are plotted as a function of temperature in figure 4.14(a) with the red filled, red open, and blue filled circles, respectively. The red dotted line indicates T_Ω, which is defined as the onset temperature of the finite B_{2g} component. The blue dotted
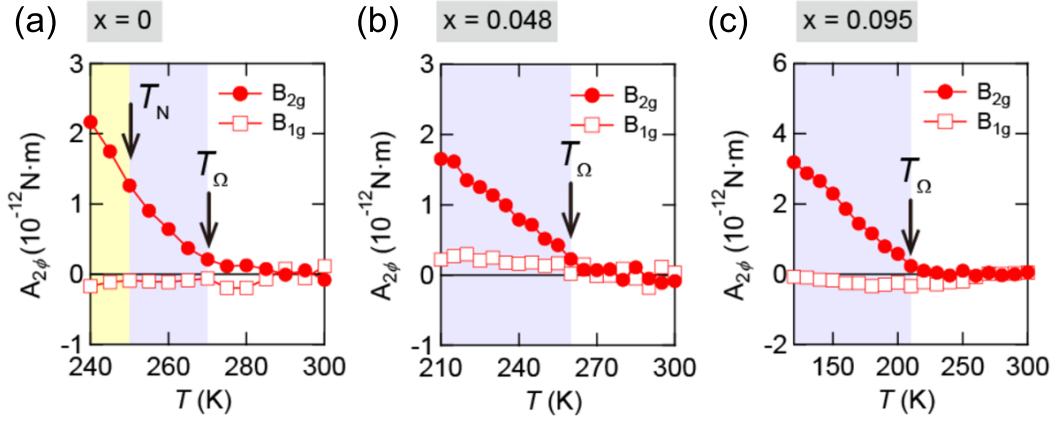
Figure 4.15: Temperature dependence of $A_{2\phi}^{B2g}$ and $A_{2\phi}^{B1g}$ are plotted as a function of temperature in a narrow range of temperature around T_Ω for (a) $x = 0$, (b) $x = 0.048$, (c) $x = 0.095$.

line indicates T_N, which is defined as the onset temperature of finite B_{1g} and four-fold components. T_N is consistent with the Néel transition temperature in large single crystal, T_N^M.

As shown in figures 4.13(a–d) and 4.14(b,c), the measurements were also performed on $x = 0.048$ and $x = 0.095$. In the same way as $x = 0$, B_{2g} component develops below T_Ω in both samples. In $x = 0.048$, $A_{4\phi}$ is also finite below T_Ω. We just point out that $x = 0.048$ is the intermediate substitution between AF-I and AF-II [241]. The magnetic order has not been well investigated yet between $x = 0$ and $x = 0.07$. To elucidate the origin of the four-fold component, further studies are required in the substitution range. The dotted blue line in figure 4.14(b) indicates T_N, which is the onset temperature of a very large B_{1g} component appears. Whereas B_{1g} component is much smaller than B_{2g} one in $x = 0$, the large B_{1g} component appears with a clear kink at T_N in $x = 0.048$. It seems that the intrinsic B_{1g} component appears below T_N. T_N is slightly higher than the Néel transition temperature $T_N^M \approx 170$ K, which was determined by the magnetization measurements on the large single crystal. The crystal used for the torque measurements was obtained from the same batch as the crystal used for the magnetization measurements. However, the Rh concentration can be inhomogeneous within the batch. A large B_{1g} component was also observed in $x = 0.095$ below $T_N^L \approx 80$ K, which is close to $T_N^M \approx 70$ K. The four-fold component also appears above T_N^L in $x = 0.095$. The dotted gray line in figure 4.14(c) indicates T_N^S, at which the occurrence of the sort-range magnetic order is expected from the phase diagram. T_N^S is roughly consistent with the onset temperature of the finite four-fold component.

4.2.3 Phase transition and rotational symmetry breaking

$A_{2\phi}^{B2g}$ and $A_{2\phi}^{B1g}$ are plotted in a narrow range of temperature around T_Ω in figures 4.15(a–c). In the area shaded with purple color, only the B_{2g} component is finite, indicating $\chi_{ab} \neq 0$. Nonzero $\chi_{ab} \neq 0$ in a tetragonal system indicates that the four-fold rotational symmetry about the c-axis is broken. This is universally observed in all three samples with
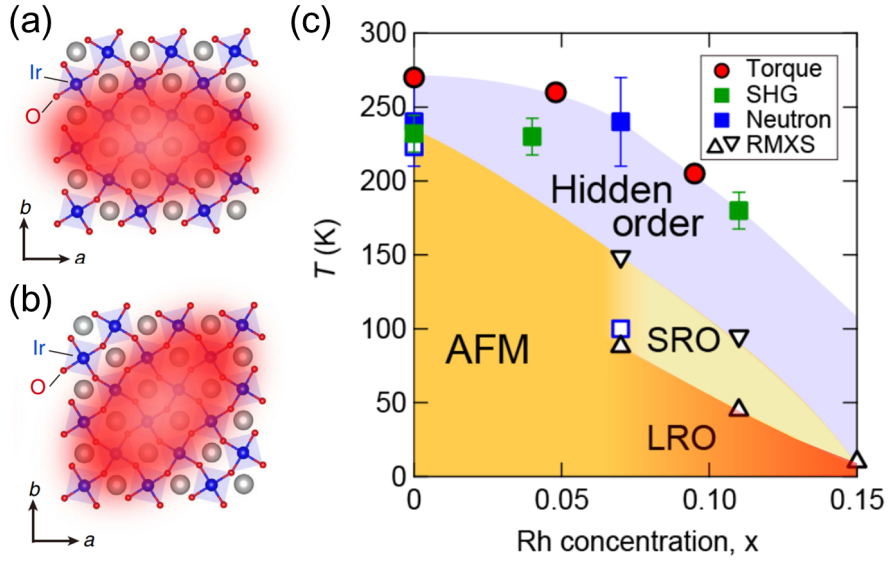
Figure 4.16: (a) The schematic of magnetic anisotropy when $\chi_{aa} - \chi_{bb} \neq 0$, and (b) when $\chi_{ab} \neq 0$ [249]. (c) The phase diagram of $Sr_2Ir_{1-x}Rh_xO_4$ ($0 \leq x \leq 0.15$). Red circles are T_Ω determined in the torque measurements. Downward/upward triangles represent the onset temperatures of short-/long-range magnetic orders [241]. Green/blue squares indicate the onset temperatures of inversion/time-reversal symmetry breaking [123, 162].

different Rh substitution levels. As shown in figure 4.16(b), $\chi_{ab} \neq 0$ indicates the magnetic anisotropy along the axis direction, which is the Ir-O-Ir bonding direction. The onset temperatures of the finite B_{2g} component, T_Ω, are plotted in the phase diagram (Figure 4.16c). In the phase diagram, we also plotted the onset temperatures of time-reversal and inversion symmetry breaking. They are roughly consistent with T_Ω. The consistency suggests that the hidden order breaks at least three symmetries: time-reversal, inversion, and rotation.

In $x = 0$, the onset temperature of rotational symmetry breaking T_Ω is slightly higher than the onset temperature of inversion and time-reversal symmetry breaking, which are consistent with the Néel transition temperature [123, 162]. One possible scenario for the discrepancy is that rotational symmetry breaking occurs at a higher temperature than the other symmetry breaking. Also, we cannot exclude the possibility that the onset temperature of the hidden order is enhanced by the magnetic field. As the torque signal is proportional to H^2, we cannot determine T_Ω at the zero-filed limit. Sample dependences should be also pointed out here. The Néel transition temperature of our $x = 0$ sample, $T_N \approx T_N^M \approx 250\,K$, is a little higher than the Néel transition temperature reported in previous studies $\sim 240\,K$ [123, 162, 241].

In general, the temperature dependence of the order parameter provides important information on the order and its phase transition. For all three samples, we observed the universal temperature dependence of the magnetic anisotropy $\chi_{ab} \propto |T - T_\Omega|$. This is distinctly different from the temperature dependence in the mean-field regime; $|T - T_c|^\beta$ ($\beta = 0.5$).

4.3   Nematic susceptibility

Nematic orders have been observed in high-T_c cuprate superconductors and iron-based superconductors by the torque measurements [94, 181, 250]. Those families exhibit a clear anomaly in the temperature dependence of nematic susceptibility around the nematic transition point [227, 251]. The nematic susceptibility is defined by $\chi_{nem} \equiv d[(\Delta R/R)_{xx} - (\Delta R/R)_{yy}]/d[\epsilon_{xx} - \epsilon_{yy}]$. Reference [251] discusses that the anisotropy of resistivity provides a direct measure of the nematic order parameter since the resistivity is generally determined by both the electronic structure and the scattering. An orbital-nematic ordering leads to an anisotropy of electronic structure, and a spin-nematic ordering leads to an anisotropy of electron scattering.

Kousuke Ishida, Yuta Mizukami, and Takasada Shibauchi in the University of Tokyo performed the elastoresistance measurements to probe the nematic transition. The sample of $x = 0.12$ was used for the measurements because the previous studies on the cuprates or iron-based superconductors report that the anomaly in the nematic susceptibility is prominent around the nematic quantum critical point [227, 251]. The endpoint of the hidden order transition would reach around or beyond $x = 0.15$, at which the antiferromagnetic order is suppressed. The samples were glued on a piezo stack. The strain was applied to the sample by the deformation of the piezo, which was controlled by applying a voltage. To apply two types of the in-plane uniaxial strain, $\epsilon_{xx} - \epsilon_{yy} \perp [100]$ and $\perp [110]$, two samples are glued on the piezo as shown in figures 4.17.

In figures 4.17(a–d), $(\Delta R/R)_{xx}$ and $(\Delta R/R)_{yy}$ are plotted as a function of strain, which was measured by the strain gauge attached to the piezo. The strain was applied along [100] direction of the crystal in (a,b) and along [110] direction in (c,d). For all the samples, a linear relation between $(\Delta R/R)_{xx}$ and ϵ_{xx} was observed in a wide range of temperatures. The nematic susceptibility χ_{nem} is plotted as a function of temperature in figures 4.17(e,f). Under the strain along both directions, [100] and [110], χ_{nem} does not exhibit any anomaly around 150 K, at which the hidden order transition is expected from the phase diagram. The divergent behavior below 50 K may result from the development of the long-range magnetic order. The absence of anomaly in the nematic susceptibility suggests that the nematic order in the hidden order is different from nematic orders which were previously observed in unconventional superconductors [227, 251]. Therefore, the torque measurements and the elastoresistance measurements suggest a peculiar hidden order parameter that directly couples with the magnetic field but does not with the strain. We can understand those experimental results by assuming an odd-parity order.

4.4   Bond-directional anapole order

4.4.1   An odd parity order

The SHG study reported that the hidden order breaks the inversion symmetry [123]. Therefore, we consider the order parameter symmetry which breaks both the inversion and rotational symmetries. The order parameter symmetry is represented by irreducible representations of D_{4h} point group which break both the inversion and rotational symmetries. The irreducible representations are listed in table 5.3. The table indicates that
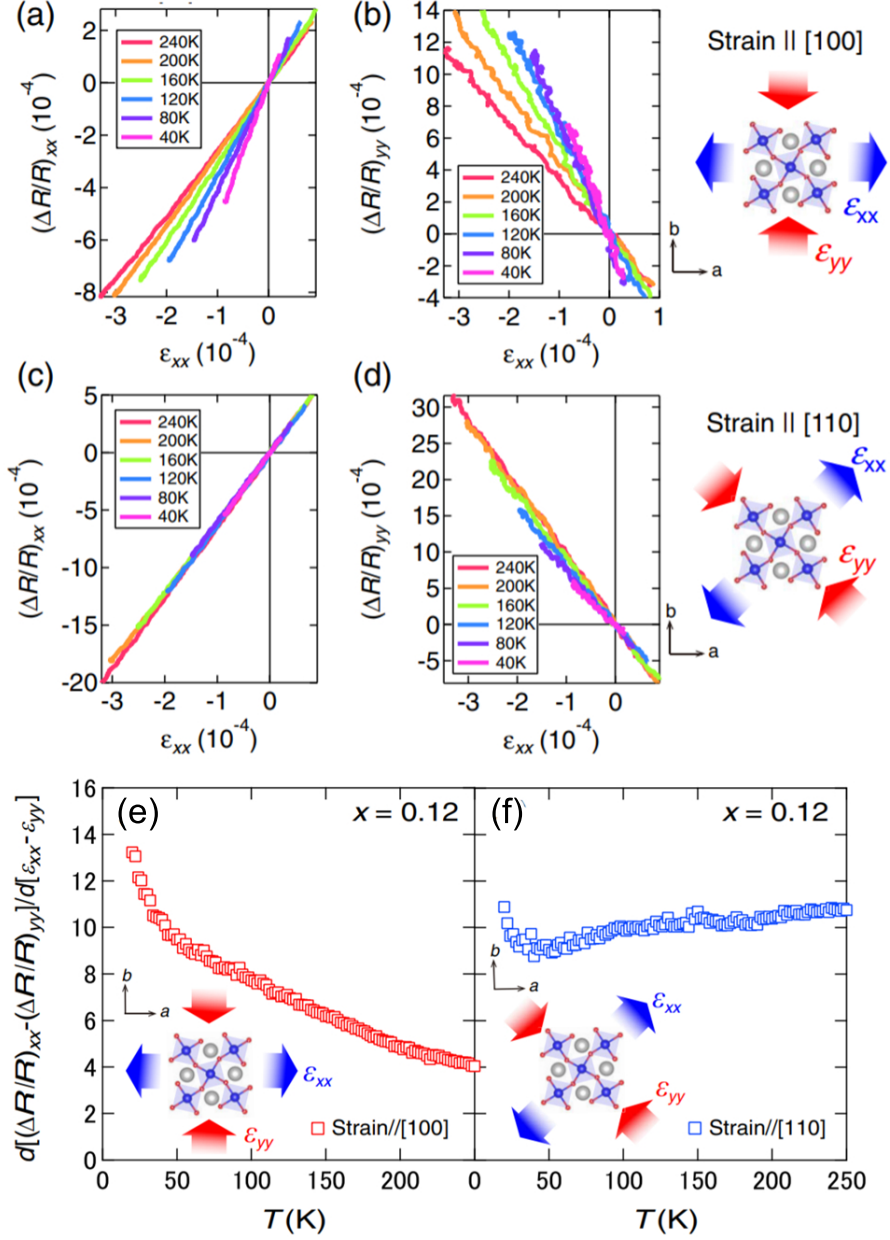
Figure 4.17: (a–d) The displacement of resistance $\Delta R/R$ is plotted as a function of the strain along [100] direction, ϵ_{xx} [249]. The strain $\epsilon_{xx} - \epsilon_{yy}$ was applied along [100] direction in (a,b) and along [110] direction in (c,d). The resistance was measured along [100] in (a,c) and along [110] in (b,d). (e,f) The nematic susceptibility, $d[(\Delta R/R)_{xx} - (\Delta R/R)_{yy}]/d[\epsilon_{xx} - \epsilon_{yy}]$, is plotted as a function of temperature [249]. The strain, $\epsilon_{xx} - \epsilon_{yy}$, was applied along [100] direction in (e) and along [110] direction in (f).

B_{1u}, B_{2u}, and E_u break both symmetries. To explain the results of the torque measurements, the order parameter has to couple with quadratic functions of magnetic field: $H_x H_y \propto \sin 2\phi$. In this section, the unit of ϕ is the radian. Basis functions of D_{4h} are listed in table 5.4. B_{1u} and B_{2u} do not have linear or quadratic functions, but E_u has degenerated linear functions: (x, y). Thus, the order parameter symmetry is E_u type since the quadratic function of (x, y) can couple with $H_x H_y$.

To describe the hidden order phase transition, the free energy is constructed to be invariant under the crystal symmetry operation. Therefore, the order parameter can couple with the quantity of the same irreducible representation. The direct products of D_{4h} are listed in table 5.5. The crystal symmetry, A_{1g}, appears only in the diagonal items of the table. The odd-parity order parameters, (Ω_x, Ω_y), cannot linearly couple with the even-parity strain. The leading order is a coupling between the strain and the quadratic function of the order parameter.

$$F_{strain} = a_0 \Omega_x \Omega_y \epsilon_{xy} + a_1 (\Omega_x^2 - \Omega_y^2)(\epsilon_{xx} - \epsilon_{yy}) + \cdots \qquad (4.6)$$

a_0 and a_1 are the coupling constants. The strain couples with the square of the order parameter. The fluctuations of the order parameter do not provide large energy gain in F_{strain}, compared to the case of the even-parity order parameter, which linearly couples with the strain. Thus, the nematic susceptibility is insensitive to the transition of the odd-parity order. The absence of anomaly in the nematic susceptibility provides evidence for the odd-parity order.

To discuss the results of the torque measurements, we consider the coupling terms with the magnetic field. As the magnetic field is even-parity as well as the strain, the field has to couple with the square of the order parameter. However, the square of the order parameter cannot linearly couple with the field, because the square of the order parameter is even under the time-reversal operation, but the field is odd. The leading order of the coupling terms is

$$F_{mag} = b_0 \Omega_x \Omega_y B_x B_y + b_1 (\Omega_x^2 - \Omega_y^2)(B_x^2 - B_y^2) + \cdots \qquad (4.7)$$

b_0 and b_1 are the coupling constants. The magnetic torque by the coupling term is,

$$\tau = -\frac{\partial F_{mag}}{\partial \phi} = \frac{b_0}{2} \Omega_x \Omega_y B^2 \cos 2\phi + 2 b_1 (\Omega_x^2 - \Omega_y^2) B^2 \sin 2\phi + \cdots \qquad (4.8)$$

The former term is consistent with the torque measurements: $\tau_{2\phi} \approx A_{2\phi}^{B2g} \cos 2\phi$. $A_{2\phi}^{B2g}$ is proportional to $\Omega_x \Omega_y$. The linear temperature dependence, $A_{2\phi}^{B2g} \propto |T - T_\Omega|$, indicates that the order parameter has square root temperature dependence; $\Omega \propto \sqrt{T - T_\Omega}$. This temperature dependence is consistent with the mean field.

4.4.2   Loop current orders

In the hidden order of $Sr_2 Ir_{1-x} Rh_x O_4$, the symmetry of the order parameter is determined: E_u and time-reversal odd. A charge order with such symmetries has been only proposed by C. M. Varma [86, 87, 202, 252], which is called "loop current order". The order was firstly proposed for understanding the time-reversal symmetry breaking in the pseudogap
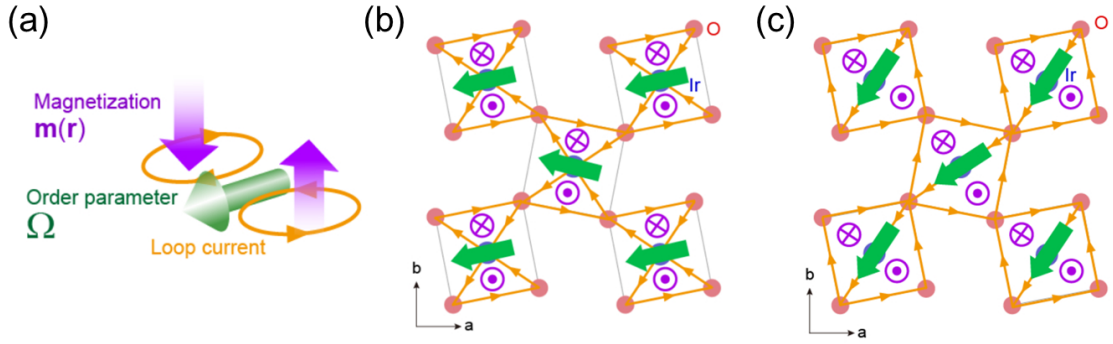
Figure 4.18: (a) The schematics of the loop current order. The yellow lines represent the loop current flowing between the atoms. The purple arrows represent the magnetization $\boldsymbol{m}(\boldsymbol{r})$ induced by the loop currents. The green arrows represent the order parameter $\boldsymbol{\Omega}$. (b) The patterns of loop currents in which the order parameter is parallel to the axis direction and (c) the diagonal direction. The green arrows represent the anapole moment induced by loop currents within the unit cell.

state of high-T_c cuprate superconductors. Recently, the order has been also discussed in the hidden order of $Sr_2Ir_{1-x}Rh_xO_4$ [123, 162].

The order is characterized by the loop current flowing between atoms as shown in figure 4.18. The clockwise and anti-clockwise loop currents (yellow lines) flow within the unit cell and induce the magnetization $\boldsymbol{m}(\boldsymbol{r})$ which is represented by the purple arrows. The order parameter $\boldsymbol{\Omega}$ is defined by the magnetization; $\boldsymbol{\Omega} = \int \boldsymbol{r} \times \boldsymbol{m}(\boldsymbol{r}) d^3r$. Theoretical studies on the loop current order are based on the microscopic $d - p$ model, which is the Hubbard model consisting of three orbitals: Cu d-orbital and oxygen p_x, p_y-orbitals. The model is reasonable for the cuprates because the hole-doped charge-transfer insulator has the oxygen band at the Fermi level. Furthermore, the cuprates have a large hybridization between Cu d- and O p-orbitals. Sr_2IrO_4 has an analogous crystal and electronic structure of the cuprates. However, the oxygen bands are well below the Fermi level, and the hybridization between Ir $J_{eff} = 1/2$ and O p is much weaker than the cuprates. Furthermore, the energy of the spin-orbit interaction is comparable to that of the Coulomb repulsion in Sr_2IrO_4, but the model does not include the spin-orbit interaction. The impact of the spin-orbit interaction on the loop current order is to be investigated.

4.4.3 An anapole order

The loop current order has the same symmetry as the ferro-toroidal orders, which have been observed in magnets [253–258]. The toroidal order is characterized by the toroidal moment, which is shown in figure 4.19(a). The toroidal moment $\boldsymbol{\Omega}_T$ is defined by the electron spins $\boldsymbol{s}$; $\boldsymbol{\Omega}_T = \sum_i \boldsymbol{r}_i \times \boldsymbol{s}_i$. The sum is taken within the unit cell. In the ferro-toroidal orders, the toroidal moments are finite and align toward one direction such as spins in a ferromagnetic order. On the other hand, the loop current order parameter is defined by the magnetization $\boldsymbol{m}(\boldsymbol{r})$, which is induced by loop currents as shown in figure 4.19(b); $\boldsymbol{\Omega} = \int \boldsymbol{r} \times \boldsymbol{m}(\boldsymbol{r}) d^3r$. $\boldsymbol{\Omega}$ is called "anapole", which was firstly introduced in the physics of elementary particles [259].
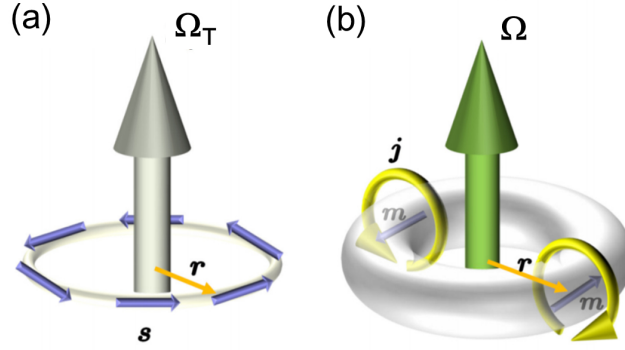
Figure 4.19: (a) The schematic of toroidal moment $\boldsymbol{\Omega}_T$ (gray arrow), which is defined by the loop of electron spins $\boldsymbol{s}$ (blue arrows) [249]. (b) The schematic of anapole moment $\boldsymbol{\Omega}$ (green arrow), which is defined by the loop currents (yellow arrows) and induced magnetization $\boldsymbol{m}$ (blue arrows) [249].

Various patterns of loop currents have been discussed in the cuprates, including patterns in which the order parameter tilted from the ab-plane [205]. Figure 4.18 shows a pattern of loop currents which is mostly studied on the cuprates. The pattern is also discussed in the hidden order of $Sr_2Ir_{1-x}Rh_xO_4$ [123, 162]. Anapole moments (green arrows) are defined within each octahedron. The anapole moments align toward the axis direction, which is along the bond between the nearest oxygens. Thus, the loop current order is a ferro-type anapole order. As shown in equation 4.8, $\chi_{aa} \neq \chi_{bb}$ and $\chi_{ab} \neq 0$ are proportional to the square of the other parameter. Therefore, the symmetry of them is higher than the order parameter. In the pattern of figure 4.18(b), the order parameter has the C_2 rotational symmetry about the axis. On the other hand, the observed magnetic anisotropy is $\chi_{ab} \neq 0$, which does not have the C_2 rotational symmetry about the axes. The pattern is inconsistent with the results of the torque measurements. Here we propose a pattern of the loop currents which is consistent with $\chi_{ab} \neq 0$ as shown in figure 4.18(c). The anapole moments align toward the diagonal direction, which is the Ir-O bonding direction. We call the order the bond-directional anapole order.

The order parameter breaks both the inversion (P) and the time-reversal (T) symmetries but does not break the PT symmetry. The symmetry is the same as the electric current, suggesting the anapole order can couple with the electric current. This suggests that the hidden order may cause non-reciprocal transport. The photogalvanic effect is also proposed [260].

Chapter 5

Conclusion

By performing the magnetic torque measurements, we have revealed novel quantum phases accompanied by rotational symmetry breaking in two strongly correlated systems: a high-T_c cuprate superconductor $HgBa_2CuO_{4+\delta}$ and a spin-orbit assisted Mott insulator $Sr_2Ir_{1-x}Rh_xO_4$. In both systems, the low-energy excitations are mapped onto a single-band Hubbard model on a 2D square lattice, in which many electronic orders are competing due to the strong correlation effect. To probe a thermodynamic phase transition accompanied by rotational symmetry breaking, we performed the magnetic torque measurements on both systems.

The first study revealed rotational symmetry breaking in the pseudogap state of a hole-doped cuprate $HgBa_2CuO_{4+\delta}$. This is the first observation of a thermodynamic phase transition accompanied by spontaneous rotational symmetry breaking at the pseudogap onset temperature. The detailed analysis revealed that the order parameter is B_{2g} type, which is 45° apart from the B_{1g}-type nematic order which was previously proposed in $YBa_2Cu_3O_{6+\delta}$. The finding indicates that the B_{2g}-type nematic ordering occurs simultaneously with the pseudogap opening. Furthermore, a competing relationship with the nematic order and the CDW order is suggested by the suppression of the in-plane magnetic anisotropy below the CDW onset temperature.

The second study revealed rotational symmetry breaking in the hidden order phase of $Sr_2Ir_{1-x}Rh_xO_4$. The torque measurements revealed the symmetry reduction to B_{2g} in the hidden order phase. In contrast to conventional nematic orders, the nematic susceptibility does not show any anomaly, indicating that the order parameter does not have a linear coupling with a strain. These observations are consistent with an odd parity order parameter, which cannot have a linear coupling with an even parity quantity such as magnetic field or strain. The comprehensive discussion concludes the order parameter symmetry E_u. Since the time-reversal symmetry breaking was also reported in the hidden order phase, the hidden order is an exotic charge order breaking many symmetries; inversion, rotation, and time-reversal. Although an order with such symmetries is previously known in magnets as a toroidal order, this is the first discovery of a charge order. A proposed microscopic mechanism for those symmetry breakings is a loop current order, in which nano-size loop current flows between atoms and induced local magnetization characterizes the order parameter. The symmetry of the torque response proposes a pattern of loop current that is different from previously proposed ones. We name the order after an

electromagnetic moment found in certain atomic nuclei; anapole.

Appendix

Table 5.1: Character table of the O_h point group

O_h	E	$8C_3$	$6C_2$	$6C_4$	$3C_2 = (C_4)^2$	i	$6S_4$	$8S_6$	$3\sigma_h$	$6\sigma_d$
A_{1g}	1	1	1	1	1	1	1	1	1	1
A_{2g}	1	1	-1	-1	1	1	-1	1	1	-1
E_g	2	-1	0	0	2	2	0	-1	2	0
T_{1g}	3	0	-1	1	-1	3	1	0	-1	-1
T_{2g}	3	0	1	-1	-1	3	-1	0	-1	1
A_{1u}	1	1	1	1	1	-1	-1	-1	-1	-1
A_{2u}	1	1	-1	-1	1	-1	1	-1	-1	1
E_u	2	-1	0	0	2	2-	0	1	-2	0
T_{1u}	3	0	-1	1	-1	-3	-1	0	1	1
T_{2u}	3	0	1	-1	-1	-3	1	0	1	-1

Table 5.2: Quadratic and quartic basis functions of the O_h point group

O_h	quadratic $f_2(x,y,z)$	quartic $f_4(x,y,z)$
A_{1g}	$x^2 + y^2 + z^2$	$x^4 + y^4 + z^4$
A_{2g}		
E_g	$2z^2 - x^2 - y^2, x^2 - y^2$	$z^4 - y^4, 2z^4 - x^4 - y^4$
T_{1g}		$xy(x^2 - y^2), xz(x^2 - z^2), yz(y^2 - z^2)$
T_{2g}	xz, yz, xy	x^2yz, xy^2z, xyz^2

Table 5.3: Character table of the D_{4h} point group

D_{4h}	E	$2C_4$	C_2	$2C_2'$	$2C_2''$	i	$2S_4$	σ_h	$2\sigma_v$	$2\sigma_d$
A_{1g}	1	1	1	1	1	1	1	1	1	1
A_{2g}	1	1	1	-1	-1	1	1	1	-1	-1
B_{1g}	1	-1	1	1	-1	1	-1	1	1	-1
B_{2g}	1	-1	1	-1	1	1	-1	1	-1	1
E_g	2	0	-2	0	0	2	0	-2	0	0
A_{1u}	1	1	1	1	1	-1	-1	-1	-1	-1
A_{2u}	1	1	1	-1	-1	-1	-1	-1	1	1
B_{1u}	1	-1	1	1	-1	-1	1	-1	-1	1
B_{2u}	1	-1	1	-1	1	-1	1	-1	1	-1
E_u	2	0	-2	0	0	-2	0	2	0	0

Table 5.4: Linear and quadratic basis functions of the D_{4h} point group

D_{4h}	linear	quadratic
A_{1g}		$x^2 + y^2, z^2$
A_{2g}		
B_{1g}		$x^2 - y^2$
B_{2g}		xy
E_g		xz, yz
A_{1u}		
A_{2u}	z	
B_{1u}		
B_{2u}		
E_u	x, y	

Table 5.5: Direct product table of the D_{4h} point group

D_{4h}	A_{1g}	A_{2g}	B_{1g}	B_{2g}	E_g	A_{1u}	A_{2u}	B_{1u}	B_{2u}	E_u
A_{1g}	A_{1g}	A_{2g}	B_{1g}	B_{2g}	E_g	A_{1u}	A_{2u}	B_{1u}	B_{2u}	E_u
A_{2g}	A_{2g}	A_{1g}	B_{2g}	B_{1g}	E_g	A_{2u}	A_{1u}	B_{2u}	B_{1u}	E_u
B_{1g}	B_{1g}	B_{2g}	A_{1g}	A_{2g}	E_g	B_{1u}	B_{2u}	A_{1u}	A_{2u}	E_u
B_{2g}	B_{2g}	B_{1g}	A_{2g}	A_{1g}	E_g	B_{2u}	B_{1u}	A_{2u}	A_{1u}	E_u
E_g	E_g	E_g	E_g	E_g	$A_{1g} \oplus A_{2g}$ $\oplus B_{1g} \oplus B_{2g}$	E_u	E_u	E_u	E_u	$A_{1u} \oplus A_{2u}$ $\oplus B_{1u} \oplus B_{2u}$
A_{1u}	A_{1u}	A_{2u}	B_{1u}	B_{2u}	E_u	A_{1g}	A_{2g}	B_{1g}	B_{2g}	E_g
A_{2u}	A_{2u}	A_{1u}	B_{2u}	B_{1u}	E_u	A_{2g}	A_{1g}	B_{2g}	B_{1g}	E_g
B_{1u}	B_{1u}	B_{2u}	A_{1u}	A_{2u}	E_u	B_{1g}	B_{2g}	A_{1g}	A_{2g}	E_g
B_{2u}	B_{2u}	B_{1u}	A_{2u}	A_{1u}	E_u	B_{2g}	B_{1g}	A_{2g}	A_{1g}	E_g
E_u	E_u	E_u	E_u	E_u	$A_{1u} \oplus A_{2u}$ $\oplus B_{1u} \oplus B_{2u}$	E_g	E_g	E_g	E_g	$A_{1g} \oplus A_{2g}$ $\oplus B_{1g} \oplus B_{2g}$
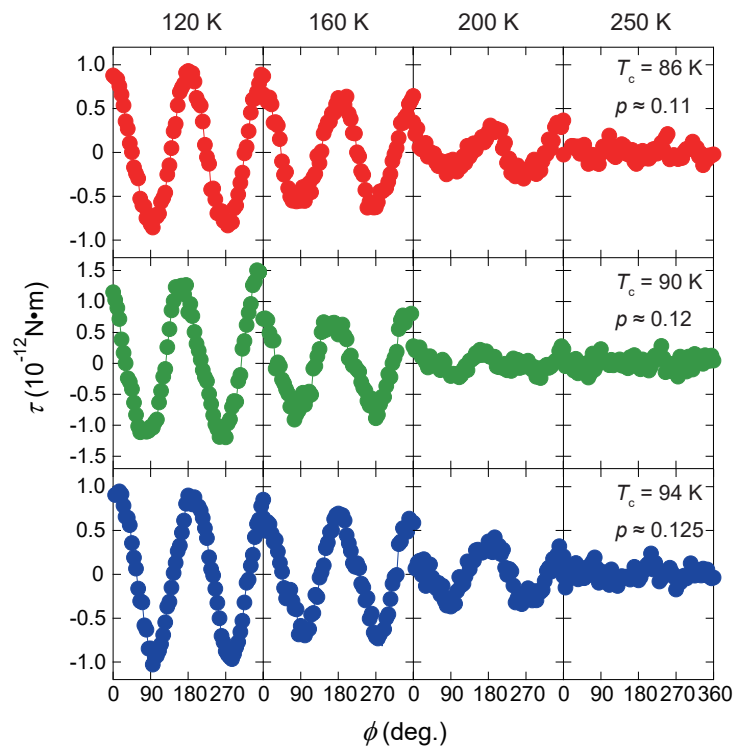
Figure 5.1: Magnetic torque of $Hg_2BaCuO_{4+\delta}$ with the in-plane magnetic field. $\tau \equiv \tau_c - \tau_{ext}$ is plotted as a function of ϕ for $p \approx 0.11$, 0.12, and 0.125.

Bibliography

[1] E. Fradkin, S. A. Kivelson, M. J. Lawler, J. P. Eisenstein and A. P. Mackenzie, "Nematic Fermi Fluids in Condensed Matter Physics", *Annual Review of Condensed Matter Physics* **1**, 153 (2010).

[2] I. J. Pomeranchuk, "On the stability of a Fermi liquid", *Sov. Phys. JETP* **8**, 361 (1958).

[3] V. Oganesyan, S. A. Kivelson and E. Fradkin, "Quantum theory of a nematic fermi fluid", *Phys. Rev. B* **64**, 195109 (2001).

[4] C. J. Halboth and W. Metzner, "d-Wave Superconductivity and Pomeranchuk Instability in the Two-Dimensional Hubbard Model", *Phys. Rev. Lett.* **85**, 5162 (2000).

[5] V. Hankevych, I. Grote and F. Wegner, "Pomeranchuk and other instabilities in the $t-t'$ Hubbard model at the Van Hove filling", *Phys. Rev. B* **66**, 094516 (2002).

[6] H.-Y. Kee, E. H. Kim and C.-H. Chung, "Signatures of an electronic nematic phase at the isotropic-nematic phase transition", *Phys. Rev. B* **68**, 245109 (2003).

[7] E. Fradkin and S. A. Kivelson, "Liquid-crystal phases of quantum Hall systems", *Phys. Rev. B* **59**, 8065 (1999).

[8] S. A. Kivelson, E. Fradkin and V. J. Emery, "Electronic liquid-crystal phases of a doped Mott insulator", *Nature* **393**, 550 (1998).

[9] E. Berg, E. Fradkin and S. A. Kivelson, "Charge-4e superconductivity from pair-density-wave order in certain high-temperature superconductors", *Nature Physics* **5**, 830 (2009).

[10] K. Sun, B. M. Fregoso, M. J. Lawler and E. Fradkin, "Fluctuating stripes in strongly correlated electron systems and the nematic-smectic quantum phase transition", *Phys. Rev. B* **78**, 085124 (2008).

[11] L. Radzihovsky and A. Vishwanath, "Quantum Liquid Crystals in an Imbalanced Fermi Gas: Fluctuations and Fractional Vortices in Larkin-Ovchinnikov States", *Phys. Rev. Lett.* **103**, 010404 (2009).

[12] J. Zaanen, Z. Nussinov and S. Mukhin, "Duality in 2+1D quantum elasticity: superconductivity and quantum nematic order", *Annals of Physics* **310**, 181 (2004).

[13] B. Keimer, S. A. Kivelson, M. R. Norman, S. Uchida and J. Zaanen, "From quantum matter to high-temperature superconductivity in copper oxides", *Nature* **518**, 179 (2015).

[14] P. A. Lee, N. Nagaosa and X.-G. Wen, "Doping a Mott insulator: Physics of high-temperature superconductivity", *Rev. Mod. Phys.* **78**, 17 (2006).

[15] J. Bertinshaw, Y. Kim, G. Khaliullin and B. Kim, "Square lattice iridates", *Annual Review of Condensed Matter Physics* **10**, 315 (2019).

[16] M. Platé, J. D. F. Mottershead, I. S. Elfimov, D. C. Peets, R. Liang, D. A. Bonn, W. N. Hardy, S. Chiuzbaian, M. Falub, M. Shi, L. Patthey and A. Damascelli, "Fermi surface and quasiparticle excitations of overdoped $Tl_2Ba_2CuO_{6+\delta}$", *Phys. Rev. Lett.* **95**, 077001 (2005).

[17] J. G. Bednorz and K. A. Müller, "Possible highT_c superconductivity in the Ba-La-Cu-O system", *Zeitschrift für Physik B Condensed Matter* **64**, 189 (1986).

[18] J. Bardeen, L. N. Cooper and J. R. Schrieffer, "Theory of superconductivity", *Physical review* **108**, 1175 (1957).

[19] N. Barišić, M. K. Chan, Y. Li, G. Yu, X. Zhao, M. Dressel, A. Smontara and M. Greven, "Universal sheet resistance and revised phase diagram of the cuprate high-temperature superconductors", *Proceedings of the National Academy of Sciences* **110**, 12235 (2013).

[20] H. A. Jahn and E. Teller, "Stability of polyatomic molecules in degenerate electronic states-I-Orbital degeneracy", *Proceedings of the Royal Society of London. Series A-Mathematical and Physical Sciences* **161**, 220 (1937).

[21] E. Pavarini, I. Dasgupta, T. Saha-Dasgupta, O. Jepsen and O. K. Andersen, "Band-Structure Trend in Hole-Doped Cuprates and Correlation with T_cmax", *Phys. Rev. Lett.* **87**, 047003 (2001).

[22] C. T. Shih, T. K. Lee, R. Eder, C.-Y. Mou and Y. C. Chen, "Enhancement of Pairing Correlation by t' in the Two-Dimensional Extended $t - J$ Model", *Phys. Rev. Lett.* **92**, 227002 (2004).

[23] N. F. Mott, "The Basis of the Electron Theory of Metals, with Special Reference to the Transition Metals", *Proceedings of the Physical Society. Section A* **62**, 416 (1949).

[24] X. Y. Zhang, M. J. Rozenberg and G. Kotliar, "Mott transition in the $d = \infty$ Hubbard model at zero temperature", *Phys. Rev. Lett.* **70**, 1666 (1993).

[25] J. P. Falck, A. Levy, M. A. Kastner and R. J. Birgeneau, "Charge-transfer spectrum and its temperature dependence in La_2CuO_4", *Phys. Rev. Lett.* **69**, 1109 (1992).

[26] A. Fujimori, E. Takayama-Muromachi, Y. Uchida and B. Okai, "Spectroscopic evidence for strongly correlated electronic states in La-Sr-Cu and Y-Ba-Cu oxides", *Phys. Rev. B* **35**, 8814 (1987).

[27] S. Peli, S. Dal Conte, R. Comin, N. Nembrini, A. Ronchi, P. Abrami, F. Banfi, G. Ferrini, D. Brida, S. Lupi *et al.*, "Mottness at finite doping and charge instabilities in cuprates", *Nature physics* **13**, 806 (2017).

[28] J. Zaanen, G. A. Sawatzky and J. W. Allen, "Band gaps and electronic structure of transition-metal compounds", *Phys. Rev. Lett.* **55**, 418 (1985).

[29] D. Vaknin, S. K. Sinha, D. E. Moncton, D. C. Johnston, J. M. Newsam, C. R. Safinya and H. E. King, "Antiferromagnetism in La_2CuO_{4-y}", *Phys. Rev. Lett.* **58**, 2802 (1987).

[30] S. Chakravarty, B. I. Halperin and D. R. Nelson, "Low-temperature behavior of two-dimensional quantum antiferromagnets", *Phys. Rev. Lett.* **60**, 1057 (1988).

[31] P. E. Sulewski, P. A. Fleury, K. B. Lyons, S.-W. Cheong and Z. Fisk, "Light scattering from quantum spin fluctuations in R_2CuO_4 (R =La, Nd, Sm)", *Phys. Rev. B* **41**, 225 (1990).

[32] K. M. Shen, F. Ronning, D. H. Lu, F. Baumberger, N. J. C. Ingle, W. S. Lee, W. Meevasana, Y. Kohsaka, M. Azuma, M. Takano, H. Takagi and Z.-X. Shen, "Nodal Quasiparticles and Antinodal Charge Ordering in $Ca_{2-x}Na_xCuO_2Cl_2$", *Science* **307**, 901 (2005).

[33] D. A. Wollman, D. J. Van Harlingen, W. C. Lee, D. M. Ginsberg and A. J. Leggett, "Experimental determination of the superconducting pairing state in YBCO from the phase coherence of YBCO-Pb dc SQUIDs", *Phys. Rev. Lett.* **71**, 2134 (1993).

[34] C. C. Tsuei and J. R. Kirtley, "Pairing symmetry in cuprate superconductors", *Rev. Mod. Phys.* **72**, 969 (2000).

[35] J. E. Hoffman, K. McElroy, D.-H. Lee, K. M. Lang, H. Eisaki, S. Uchida and J. C. Davis, "Imaging quasiparticle interference in $Bi_2Sr_2 CaCu_2O_{8+\delta}$", *Science* **297**, 1148 (2002).

[36] D. J. Scalapino, E. Loh and J. E. Hirsch, "d-wave pairing near a spin-density-wave instability", *Phys. Rev. B* **34**, 8190 (1986).

[37] K. Miyake, S. Schmitt-Rink and C. M. Varma, "Spin-fluctuation-mediated even-parity pairing in heavy-fermion superconductors", *Phys. Rev. B* **34**, 6554 (1986).

[38] M. T. Béal-Monod, C. Bourbonnais and V. J. Emery, "Possible superconductivity in nearly antiferromagnetic itinerant fermion systems", *Phys. Rev. B* **34**, 7716 (1986).

[39] T. Dahm, V. Hinkov, S. V. Borisenko, A. A. Kordyuk, V. B. Zabolotnyy, J. Fink, B. Büchner, D. Scalapino, W. Hanke and B. Keimer, "Strength of the spin-fluctuation-mediated pairing interaction in a high-temperature superconductor", *Nature Physics* **5**, 217 (2009).

[40] M. Le Tacon, G. Ghiringhelli, J. Chaloupka, M. M. Sala, V. Hinkov, M. W. Haverkort, M. Minola, M. Bakr, K. J. Zhou, S. Blanco-Canosa, C. Monney, Y. T. Song, G. L. Sun, C. T. Lin, G. M. De Luca, M. Salluzzo, G. Khaliullin, T. Schmitt and B. Braicovich, "Intense paramagnon excitations in a large family of high-temperature superconductors", *Nature Physics* **7**, 725 (2011).

[41] M. Dean, G. Dellea, R. S. Springell, F. Yakhou-Harris, K. Kummer, N. Brookes, X. Liu, Y. Sun, J. Strle, T. Schmitt *et al.*, "Persistence of magnetic excitations in $La_{2-x}Sr_xCuO_4$ from the undoped insulator to the heavily overdoped non-superconducting metal", *Nature materials* **12**, 1019 (2013).

[42] D. Reznik, L. Pintschovius, M. Ito, S. Iikubo, M. Sato, H. Goka, M. Fujita, K. Yamada, G. D. Gu and J. M. Tranquada, "Electron-phonon coupling reflecting dynamic charge inhomogeneity in copper oxide superconductors", *Nature* **440**, 1170 (2006).

[43] A. Lanzara, P. V. Bogdanov, X. J. Zhou, S. A. Kellar, D. L. Feng, E. D. Lu, T. Yoshida, H. Eisaki, A. Fujimori, K. Kishio, J. I. Shimoyama, T. Noda, S. Uchida, H. Z and S. Z. X, "Evidence for ubiquitous strong electron-phonon coupling in high-temperature superconductors", *Nature* **412**, 510 (2001).

[44] Y. Kohsaka, C. Taylor, P. Wahl, A. Schmidt, J. Lee, K. Fujita, J. Alldredge, K. McElroy, J. Lee, H. Eisaki, S. Uchida, D. H. Lee and J. C. Davis, "How Cooper pairs vanish approaching the Mott insulator in $Bi_2Sr_2CaCu_2O_{8+\delta}$", *Nature* **454**, 1072 (2008).

[45] Y. J. Uemura, G. M. Luke, B. J. Sternlieb, J. H. Brewer, J. F. Carolan, W. N. Hardy, R. Kadono, J. R. Kempton, R. F. Kiefl, S. R. Kreitzman, P. Mulhern, T. M. Riseman, D. L. Williams, B. X. Yang, S. Uchida, H. Takagi, J. Gopalakrishnan, A. W. Sleight, M. A. Subramanian, C. L. Chien *et al.*, "Universal correlations between T_c and $\frac{n_s}{m^*}$ (Carrier Density over Effective Mass) in High-T_c Cuprate Superconductors", *Phys. Rev. Lett.* **62**, 2317 (1989).

[46] V. J. Emery and S. A. Kivelson, "Importance of phase fluctuations in superconductors with small superfluid density", *Nature* **374**, 434 (1995).

[47] W. W. Warren, R. E. Walstedt, G. F. Brennert, R. J. Cava, R. Tycko, R. F. Bell and G. Dabbagh, "Cu spin dynamics and superconducting precursor effects in planes above t_c in $YBa_2Cu_3O_{6.7}$", *Phys. Rev. Lett.* **62**, 1193 (1989).

[48] H. Alloul, T. Ohno and P. Mendels, "^{89}y nmr evidence for a fermi-liquid behavior in $YBa_2Cu_3O_{6+x}$", *Phys. Rev. Lett.* **63**, 1700 (1989).

[49] C. C. Homes, T. Timusk, R. Liang, D. A. Bonn and W. N. Hardy, "Optical conductivity of c axis oriented $YBa_2Cu_3O_{6.70}$: Evidence for a pseudogap", *Phys. Rev. Lett.* **71**, 1645 (1993).

[50] B. Bucher, P. Steiner, J. Karpinski, E. Kaldis and P. Wachter, "Influence of the spin gap on the normal state transport in $YBa_2Cu_4O_8$", *Phys. Rev. Lett.* **70**, 2012 (1993).

[51] T. Ito, K. Takenaka and S. Uchida, "Systematic deviation from T-linear behavior in the in-plane resistivity of $YBa_2Cu_3O_{7-\delta}$: Evidence for dominant spin scattering", *Phys. Rev. Lett.* **70**, 3995 (1993).

[52] M. K. Chan, M. J. Veit, C. J. Dorow, Y. Ge, Y. Li, W. Tabis, Y. Tang, X. Zhao, N. Barišić and M. Greven, "In-Plane Magnetoresistance Obeys Kohler's Rule in the Pseudogap Phase of Cuprate Superconductors", *Phys. Rev. Lett.* **113**, 177005 (2014).

[53] H. Ding, T. Yokoya, J. C. Campuzano, T. Takahashi, M. Randeria, M. Norman, T. Mochiku, K. Kadowaki and J. Giapintzakis, "Spectroscopic evidence for a pseudogap in the normal state of underdoped high-T_c superconductors", *Nature* **382**, 51 (1996).

[54] M. R. Norman, H. Ding, M. Randeria, J. C. Campuzano, T. Yokoya, T. Takeuchi, T. Takahashi, T. Mochiku, K. Kadowaki, P. Guptasarma and D. G. Hinks, "Destruction of the fermi surface in underdoped high-T_c superconductors", *Nature* **392**, 157 (1998).

[55] D. S. Marshall, D. S. Dessau, A. G. Loeser, C.-H. Park, A. Y. Matsuura, J. N. Eckstein, I. Bozovic, P. Fournier, A. Kapitulnik, W. E. Spicer and Z.-X. Shen, "Unconventional Electronic Structure Evolution with Hole Doping in $Bi_2Sr_2CaCu_2O_{8+\delta}$: Angle-Resolved Photoemission Results", *Phys. Rev. Lett.* **76**, 4841 (1996).

[56] H.-B. Yang, J. D. Rameau, P. D. Johnson, T. Valla, A. Tsvelik and G. D. Gu, "Emergence of preformed cooper pairs from the doped mott insulating state in $Bi_2Sr_2\,CaCu_2O_{8+\delta}$", *Nature* **456**, 77 (2008).

[57] K. McElroy, R. W. Simmonds, J. E. Hoffman, D.-H. Lee, J. Orenstein, H. Eisaki, S. Uchida and J. C. Davis, "Relating atomic-scale electronic phenomena to wave-like quasiparticle states in superconducting $Bi_2Sr_2\,CaCu_2O_{8+\delta}$", *Nature* **422**, 592 (2003).

[58] K. Fujita, C. K. Kim, I. Lee, J. Lee, M. Hamidian, I. Firmo, S. Mukhopadhyay, H. Eisaki, S. Uchida, M. Lawler *et al.*, "Simultaneous transitions in cuprate momentum-space topology and electronic symmetry breaking", *Science* **344**, 612 (2014).

[59] J. Corson, R. Mallozzi, J. Orenstein, J. Eckstein and I. Bozovic, "Vanishing of phase coherence in underdoped $Bi_2Sr_2\,CaCu_2O_{8+\delta}$", *Nature* **398**, 221 (1999).

[60] A. Dubroka, M. Rössle, K. W. Kim, V. K. Malik, D. Munzar, D. N. Basov, A. A. Schafgans, S. J. Moon, C. T. Lin, D. Haug, V. Hinkov, B. Keimer, T. Wolf, J. G. Storey, J. L. Tallon and C. Bernhard, "Evidence of a Precursor Superconducting Phase at Temperatures as High as 180 K in RBa$_2$Cu$_3$O$_{7-\delta}$ (R =Y, Gd, E) Superconducting Crystals from Infrared Spectroscopy", *Phys. Rev. Lett.* **106**, 047006 (2011).

[61] S. Kaiser, C. R. Hunt, D. Nicoletti, W. Hu, I. Gierz, H. Y. Liu, M. Le Tacon, T. Loew, D. Haug, B. Keimer and A. Cavalleri, "Optically induced coherent transport far above T_c in underdoped YBa$_2$Cu$_3$O$_{6+\delta}$", *Phys. Rev. B* **89**, 184516 (2014).

[62] M. R. Norman, A. Kanigel, M. Randeria, U. Chatterjee and J. C. Campuzano, "Modeling the Fermi arc in underdoped cuprates", *Phys. Rev. B* **76**, 174501 (2007).

[63] T. J. Reber, N. C. Plumb, Z. Sun, Y. Cao, Q. Wang, K. McElroy, H. Iwasawa, M. Arita, J. S. Wen, Z. J. Xu, G. Gu, Y. Yoshida, H. Eisaki, Y. Aiura and D. S. Dessau, "The origin and non-quasiparticle nature of Fermi arcs in Bi$_2$Sr$_2$ CaCu$_2$O$_{8+\delta}$", *Nature Physics* **8**, 606 (2012).

[64] J. Lee, K. Fujita, A. R. Schmidt, C. K. Kim, H. Eisaki, S. Uchida and J. C. Davis, "Spectroscopic fingerprint of phase-incoherent superconductivity in the underdoped Bi$_2$Sr$_2$ CaCu$_2$O$_{8+\delta}$", *Science* **325**, 1099 (2009).

[65] J. Chang, E. Blackburn, A. Holmes, N. B. Christensen, J. Larsen, J. Mesot, R. Liang, D. Bonn, W. Hardy, A. Watenphul, M. v. Zimmermann, E. M. Forgan and H. S. M, "Direct observation of competition between superconductivity and charge density wave order in YBa$_2$Cu$_3$O$_{6.67}$", *Nature Physics* **8**, 871 (2012).

[66] R. Comin, R. Sutarto, E. H. da Silva Neto, L. Chauviere, R. Liang, W. N. Hardy, D. A. Bonn, F. He, G. A. Sawatzky and A. Damascelli, "Broken translational and rotational symmetry via charge stripe order in underdoped YBa$_2$Cu$_3$O$_{6+y}$", *Science* **347**, 1335 (2015).

[67] J. M. Tranquada, B. J. Sternlieb, J. D. Axe, Y. Nakamura and S. Uchida, "Evidence for stripe correlations of spins and holes in copper oxide superconductors", *Nature* **375**, 561 (1995).

[68] M. Arai, T. Nishijima, Y. Endoh, T. Egami, S. Tajima, K. Tomimoto, Y. Shiohara, M. Takahashi, A. Garrett and S. M. Bennington, "Incommensurate Spin Dynamics of Underdoped Superconductor YBa$_2$Cu$_3$O$_{6.7}$", *Phys. Rev. Lett.* **83**, 608 (1999).

[69] V. Hinkov, P. Bourges, S. Pailhes, Y. Sidis, A. Ivanov, C. Frost, T. Perring, C. Lin, D. Chen and B. Keimer, "Spin dynamics in the pseudogap state of a high-temperature superconductor", *Nature Physics* **3**, 780 (2007).

[70] E. H. da Silva Neto, P. Aynajian, A. Frano, R. Comin, E. Schierle, E. Weschke, A. Gyenis, J. Wen, J. Schneeloch, Z. Xu, S. Ono, G. Gu, M. L. Tacon and A. Yazdani, "Ubiquitous Interplay Between Charge Ordering and High-Temperature Superconductivity in Cuprates", *Science* **343**, 393 (2014).

[71] R. Comin, A. Frano, M. M. Yee, Y. Yoshida, H. Eisaki, E. Schierle, E. Weschke, R. Sutarto, F. He, A. Soumyanarayanan, Y. He, M. Le Tacon, I. S. Elfimov, J. E. Hoffman, G. A. Sawatzky, B. Keimer and A. Damascelli, "Charge order driven by Fermi-arc instability in $Bi_2Sr_{2-x}La_xCuO_{6+\delta}$", *Science* **343**, 390 (2014).

[72] T. Wu, H. Mayaffre, S. Krämer, M. Horvatić, C. Berthier, W. Hardy, R. Liang, D. Bonn and M.-H. Julien, "Magnetic-field-induced charge-stripe order in the high-temperature superconductor $YBa_2Cu_3O_y$", *Nature* **477**, 191 (2011).

[73] W. Tabis, Y. Li, M. Le Tacon, L. Braicovich, A. Kreyssig, M. Minola, G. Dellea, E. Weschke, M. Veit, M. Ramazanoglu *et al.*, "Charge order and its connection with Fermi-liquid charge transport in a pristine high-T_c cuprate", *Nature Communications* **5**, 5875 (2014).

[74] G. Ghiringhelli, M. Le Tacon, M. Minola, S. Blanco-Canosa, C. Mazzoli, N. Brookes, G. De Luca, A. Frano, D. Hawthorn, F. He *et al.*, "Long-range incommensurate charge fluctuations in (Y, Nd)$Ba_2Cu_3O_{6+x}$", *Science* **337**, 821 (2012).

[75] S. Blanco-Canosa, A. Frano, E. Schierle, J. Porras, T. Loew, M. Minola, M. Bluschke, E. Weschke, B. Keimer and M. Le Tacon, "Resonant x-ray scattering study of charge-density wave correlations in$YBa_2Cu_3O_{6+x}$", *Phys. Rev. B* **90**, 054513 (2014).

[76] N. Doiron-Leyraud, C. Proust, D. LeBoeuf, J. Levallois, J.-B. Bonnemaison, R. Liang, D. Bonn, W. Hardy and L. Taillefer, "Quantum oscillations and the fermi surface in an underdoped high-T_c superconductor", *Nature* **447**, 565 (2007).

[77] S. E. Sebastian, N. Harrison, F. Balakirev, M. Altarawneh, P. Goddard, R. Liang, D. Bonn, W. Hardy and G. Lonzarich, "Normal-state nodal electronic structure in underdoped high-T_c copper oxides", *Nature* **511**, 61 (2014).

[78] F. Laliberté, J. Chang, N. Doiron-Leyraud, E. Hassinger, R. Daou, M. Rondeau, B. Ramshaw, R. Liang, D. Bonn, W. Hardy *et al.*, "Fermi-surface reconstruction by stripe order in cuprate superconductors", *Nature Communications* **2**, 432 (2011).

[79] C. M. Varma, "Pseudogap and Fermi arcs in underdoped cuprates", *Phys. Rev. B* **99**, 224516 (2019).

[80] Y. Ando, K. Segawa, S. Komiya and A. N. Lavrov, "Electrical Resistivity Anisotropy from Self-Organized One Dimensionality in High-Temperature Superconductors", *Phys. Rev. Lett.* **88**, 137005 (2002).

[81] R. Daou, J. Chang, D. LeBoeuf, O. Cyr-Choiniere, F. Laliberté, N. Doiron-Leyraud, B. Ramshaw, R. Liang, D. Bonn, W. Hardy *et al.*, "Broken rotational symmetry in the pseudogap phase of a high-T_c superconductor", *Nature* **463**, 519 (2010).

[82] L. Mangin-Thro, Y. Li, Y. Sidis and P. Bourges, "$a - b$ Anisotropy of the Intra-Unit-Cell Magnetic Order in $YBa_2Cu_3O_{6.6}$", *Phys. Rev. Lett.* **118**, 097003 (2017).

[83] A. Kaminski, S. Rosenkranz, H. M. Fretwell, J. C. Campuzano, Z. Li, H. Raffy, W. G. Cullen, H. You, C. G. Olson, C. M. Varma *et al.*, "Spontaneous breaking of time-reversal symmetry in the pseudogap state of a high-T_c superconductor", *Nature* **416**, 610 (2002).

[84] Y. Li, V. Balédent, N. Barišić, Y. Cho, B. Fauqué, Y. Sidis, G. Yu, X. Zhao, P. Bourges and M. Greven, "Unusual magnetic order in the pseudogap region of the superconductor HgBa$_2$CuO$_{4+\delta}$", *Nature* **455**, 372 (2008).

[85] B. Fauqué, Y. Sidis, V. Hinkov, S. Pailhès, C. T. Lin, X. Chaud and P. Bourges, "Magnetic order in the pseudogap phase of high-T_C superconductors", *Phys. Rev. Lett.* **96**, 197001 (2006).

[86] M. E. Simon and C. M. Varma, "Detection and Implications of a Time-Reversal Breaking State in Underdoped Cuprates", *Phys. Rev. Lett.* **89**, 247003 (2002).

[87] C. M. Varma, "Theory of the pseudogap state of the cuprates", *Phys. Rev. B* **73**, 155113 (2006).

[88] L. Zhao, C. A. Belvin, R. Liang, D. A. Bonn, W. N. Hardy, N. P. Armitage and D. Hsieh, "A global inversion-symmetry-broken phase inside the pseudogap region of YBa$_2$Cu$_3$O$_y$", *Nature Physics* **13**, 250 (2017).

[89] A. de La Torre, K. Seyler, L. Zhao, S. Di Matteo, M. Scheurer, Y. Li, B. Yu, M. Greven, S. Sachdev, M. Norman *et al.*, "Mirror symmetry breaking in a model insulating cuprate", *Nature Physics* **17**, 777 (2021).

[90] O. Cyr-Choiniere, R. Daou, F. Laliberté, D. LeBoeuf, N. Doiron-Leyraud, J. Chang, J.-Q. Yan, J.-G. Cheng, J.-S. Zhou, J. B. Goodenough, S. Pyon, T. Takayama, H. Takagi, Y. Tanaka and L. Taillefer, "Enhancement of the Nernst effect by stripe order in a high-T_c superconductor", *Nature* **458**, 743 (2009).

[91] N. Doiron-Leyraud, S. Lepault, O. Cyr-Choinière, B. Vignolle, G. Grissonnanche, F. Laliberté, J. Chang, N. Baršić, M. K. Chan, L. Ji, X. Zhao, Y. Li, M. Greven, C. Proust and L. Taillefer, "Hall, Seebeck, and Nernst Coefficients of Underdoped HgBa$_2$CuO$_{4+\delta}$: Fermi-Surface Reconstruction in an Archetypal Cuprate Superconductor", *Phys. Rev. X* **3**, 021019 (2013).

[92] J. Chang, R. Daou, C. Proust, D. LeBoeuf, N. Doiron-Leyraud, F. Laliberté, B. Pingault, B. J. Ramshaw, R. Liang, D. A. Bonn, W. N. Hardy, H. Takagi, A. B. Antunes, I. Sheikin, K. Behnia and L. Taillefer, "Nernst and Seebeck Coefficients of the Cuprate Superconductor YBa$_2$Cu$_3$O$_{6.67}$: A Study of Fermi Surface Reconstruction", *Phys. Rev. Lett.* **104**, 057005 (2010).

[93] O. Cyr-Choinière, G. Grissonnanche, S. Badoux, J. Day, D. A. Bonn, W. N. Hardy, R. Liang, N. Doiron-Leyraud and L. Taillefer, "Two types of nematicity in the phase diagram of the cuprate superconductor YBa$_2$Cu$_3$O$_y$", *Phys. Rev. B* **92**, 224502 (2015).

[94] Y. Sato, S. Kasahara, H. Murayama, Y. Kasahara, E.-G. Moon, T. Nishizaki, T. Loew, J. Porras, B. Keimer, T. Shibauchi and Y. Matsuda, "Thermodynamic evidence for a nematic phase transition at the onset of the pseudogap in YBa$_2$Cu$_3$O$_y$", *Nature Physics* **13**, 1074 (2017).

[95] M. Lawler, K. Fujita, J. Lee, A. Schmidt, Y. Kohsaka, C. K. Kim, H. Eisaki, S. Uchida, J. Davis, J. Sethna *et al.*, "Intra-unit-cell electronic nematicity of the high-t_c copper-oxide pseudogap states", *Nature* **466**, 347 (2010).

[96] S. Mukhopadhyay, R. Sharma, C. K. Kim, S. D. Edkins, M. H. Hamidian, H. Eisaki, S.-i. Uchida, E.-A. Kim, M. J. Lawler, A. P. Mackenzie, J. C. S. Davis and K. Fujita, "Evidence for a vestigial nematic state in the cuprate pseudogap phase", *Proceedings of the National Academy of Sciences* **116**, 13249 (2019).

[97] I. Tomeno, T. Machi, K. Tai, N. Koshizuka, S. Kambe, A. Hayashi, Y. Ueda and H. Yasuoka, "Nmr study of spin dynamics at planar oxygen and copper sites in YBa$_2$Cu$_4$O$_8$", *Phys. Rev. B* **49**, 15327 (1994).

[98] W. Wang, J. Luo, C. Wang, J. Yang, Y. Kodama, R. Zhou and G.-Q. Zheng, "Microscopic evidence for the intra-unit-cell electronic nematicity inside the pseudogap phase in YBa$_2$Cu$_4$O$_8$", *SCIENCE CHINA Physics, Mechanics & Astronomy* **64**, 237413 (2021).

[99] S. A. Kivelson and S. Lederer, "Linking the pseudogap in the cuprates with local symmetry breaking: A commentary", *Proceedings of the National Academy of Sciences* **116**, 14395 (2019).

[100] L. Nie, G. Tarjus and S. A. Kivelson, "Quenched disorder and vestigial nematicity in the pseudogap regime of the cuprates", *Proceedings of the National Academy of Sciences* **111**, 7980 (2014).

[101] L. Nie, A. V. Maharaj, E. Fradkin and S. A. Kivelson, "Vestigial nematicity from spin and/or charge order in the cuprates", *Phys. Rev. B* **96**, 085142 (2017).

[102] J. Xia, E. Schemm, G. Deutscher, S. A. Kivelson, D. A. Bonn, W. N. Hardy, R. Liang, W. Siemons, G. Koster, M. M. Fejer and A. Kapitulnik, "Polar Kerr-Effect Measurements of the High-Temperature YBa$_2$Cu$_3$O$_{6+x}$ Superconductor: Evidence for Broken Symmetry near the Pseudogap Temperature", *Phys. Rev. Lett.* **100**, 127002 (2008).

[103] Q. Si and F. Steglich, "Heavy Fermions and Quantum Phase Transitions", *Science* **329**, 1161 (2010).

[104] H. v. Löhneysen, A. Rosch, M. Vojta and P. Wölfle, "Fermi-liquid instabilities at magnetic quantum phase transitions", *Rev. Mod. Phys.* **79**, 1015 (2007).

[105] T. Shibauchi, A. Carrington and Y. Matsuda, "A Quantum Critical Point Lying Beneath the Superconducting Dome in Iron Pnictides", *Annual Review of Condensed Matter Physics* **5**, 113 (2014).

[106] C. M. Varma, "Colloquium: Linear in temperature resistivity and associated mysteries including high temperature superconductivity", *Rev. Mod. Phys.* **92**, 031001 (2020).

[107] S. Martin, A. T. Fiory, R. M. Fleming, L. F. Schneemeyer and J. V. Waszczak, "Normal-state transport properties of $Bi_{2+x}Sr_{2-y}CuO_{6+\delta}$ crystals", *Phys. Rev. B* **41**, 846 (1990).

[108] C. M. Varma, P. B. Littlewood, S. Schmitt-Rink, E. Abrahams and A. E. Ruckenstein, "Phenomenology of the normal state of Cu-O high-temperature superconductors", *Phys. Rev. Lett.* **63**, 1996 (1989).

[109] A. Legros, S. Benhabib, W. Tabis, F. Laliberté, M. Dion, M. Lizaire, B. Vignolle, D. Vignolles, H. Raffy, Z. Li *et al.*, "Universal T-linear resistivity and Planckian dissipation in overdoped cuprates", *Nature Physics* **15**, 142 (2019).

[110] T. Valla, A. V. Fedorov, P. D. Johnson, B. O. Wells, S. L. Hulbert, Q. Li, G. D. Gu and N. Koshizuka, "Evidence for Quantum Critical Behavior in the Optimally Doped Cuprate $Bi_2Sr_2CaCu_2O_{8+\delta}$", *Science* **285**, 2110 (1999).

[111] D. v. d. Marel, H. Molegraaf, J. Zaanen, Z. Nussinov, F. Carbone, A. Damascelli, H. Eisaki, M. Greven, P. Kes and M. Li, "Quantum critical behaviour in a high-T_c superconductor", *Nature* **425**, 271 (2003).

[112] J. Zaanen, "Why the temperature is high", *Nature* **430**, 512 (2004).

[113] D. H. Torchinsky, H. Chu, L. Zhao, N. B. Perkins, Y. Sizyuk, T. Qi, G. Cao and D. Hsieh, "Structural Distortion-Induced Magnetoelastic Locking in Sr_2IrO_4 Revealed through Nonlinear Optical Harmonic Generation", *Phys. Rev. Lett.* **114**, 096404 (2015).

[114] B. J. Kim, H. Ohsumi, T. Komesu, S. Sakai, T. Morita, H. Takagi and T. Arima, "Phase-Sensitive Observation of a Spin-Orbital Mott State in Sr_2IrO_4", *Science* **323**, 1329 (2009).

[115] M. Subramanian, M. Crawford, R. Harlow, T. Ami, J. Fernandez-Baca, Z. Wang and D. Johnston, "Sr_2RhO_4 and Sr_2IrO_4: Structural and magnetic studies of 4d and 5d transition metal analogs of La_2CuO_4", *Physica C: Superconductivity* **235-240**, 743 (1994).

[116] R. S. Perry, F. Baumberger, L. Balicas, N. Kikugawa, N. J. C. Ingle, A. Rost, J. F. Mercure, Y. Maeno, Z. X. Shen and A. P. Mackenzie, "Sr_2RhO_4 : a new, clean correlated electron metal", *New Journal of Physics* **8**, 175 (2006).

[117] B. J. Kim, J. Yu, H. Koh, I. Nagai, S. I. Ikeda, S.-J. Oh and C. Kim, "Missing xy-Band Fermi Surface in $4d$ Transition-Metal Oxide Sr_2RhO_4: Effect of the Octahedra Rotation on the Electronic Structure", *Phys. Rev. Lett.* **97**, 106401 (2006).

[118] F. Baumberger, N. J. C. Ingle, W. Meevasana, K. M. Shen, D. H. Lu, R. S. Perry, A. P. Mackenzie, Z. Hussain, D. J. Singh and Z.-X. Shen, "Fermi Surface and Quasiparticle Excitations of Sr_2RhO_4", *Phys. Rev. Lett.* **96**, 246402 (2006).

[119] C. Martins, M. Aichhorn, L. Vaugier and S. Biermann, "Reduced Effective Spin-Orbital Degeneracy and Spin-Orbital Ordering in Paramagnetic Transition-Metal Oxides: Sr_2IrO_4 versus Sr_2RhO_4", *Phys. Rev. Lett.* **107**, 266404 (2011).

[120] B. J. Kim, H. Jin, S. J. Moon, J.-Y. Kim, B.-G. Park, C. S. Leem, J. Yu, T. W. Noh, C. Kim, S.-J. Oh, J.-H. Park, V. Durairaj, G. Cao and E. Rotenberg, "Novel $J_{eff} = 1/2$ Mott State Induced by Relativistic Spin-Orbit Coupling in Sr_2IrO_4", *Phys. Rev. Lett.* **101**, 076402 (2008).

[121] F. Wang and T. Senthil, "Twisted Hubbard Model for Sr_2IrO_4: Magnetism and Possible High Temperature Superconductivity", *Phys. Rev. Lett.* **106**, 136402 (2011).

[122] F. Ye, X. Wang, C. Hoffmann, J. Wang, S. Chi, M. Matsuda, B. C. Chakoumakos, J. A. Fernandez-Baca and G. Cao, "Structure symmetry determination and magnetic evolution in $Sr_2Ir_{1-x}Rh_xO_4$", *Phys. Rev. B* **92**, 201112 (2015).

[123] L. Zhao, D. H. Torchinsky, H. Chu, V. Ivanov, R. Lifshitz, R. Flint, T. Qi, G. Cao and D. Hsieh, "Evidence of an odd-parity hidden order in a spin-orbit coupled correlated iridate", *Nature Physics* **12**, 32 (2016).

[124] G. Jackeli and G. Khaliullin, "Mott Insulators in the Strong Spin-Orbit Coupling Limit: From Heisenberg to a Quantum Compass and Kitaev Models", *Phys. Rev. Lett.* **102**, 017205 (2009).

[125] V. Ilakovac, A. Louat, A. Nicolaou, J.-P. Rueff, Y. Joly and V. Brouet, "Oxygen states in La- and Rh-doped Sr_2IrO_4 probed by angle-resolved photoemission and O K-edge resonant inelastic x-ray scattering", *Phys. Rev. B* **99**, 035149 (2019).

[126] M. Moretti Sala, S. Boseggia, D. F. McMorrow and G. Monaco, "Resonant X-Ray Scattering and the $j_{eff} = 1/2$ Electronic Ground State in Iridate Perovskites", *Phys. Rev. Lett.* **112**, 026403 (2014).

[127] B. J. Kim and G. Khaliullin, "Resonant inelastic x-ray scattering operators for t_{2g} orbital systems", *Phys. Rev. B* **96**, 085108 (2017).

[128] S. Agrestini, C.-Y. Kuo, M. Moretti Sala, Z. Hu, D. Kasinathan, K.-T. Ko, P. Glatzel, M. Rossi, J.-D. Cafun, K. O. Kvashnina, A. Matsumoto, T. Takayama, H. Takagi, L. H. Tjeng and M. W. Haverkort, "Long-range interactions in the effective low-energy Hamiltonian of Sr_2IrO_4: A core-to-core resonant inelastic x-ray scattering study", *Phys. Rev. B* **95**, 205123 (2017).

[129] R. Arita, J. Kuneš, A. V. Kozhevnikov, A. G. Eguiluz and M. Imada, "Ab initio Studies on the Interplay between Spin-Orbit Interaction and Coulomb Correlation in Sr_2IrO_4 and Ba_2IrO_4", *Phys. Rev. Lett.* **108**, 086403 (2012).

[130] S. J. Moon, H. Jin, W. S. Choi, J. S. Lee, S. S. A. Seo, J. Yu, G. Cao, T. W. Noh and Y. S. Lee, "Temperature dependence of the electronic structure of the $j_{eff} = \frac{1}{2}$ mott insulator Sr_2IrO_4 studied by optical spectroscopy", *Phys. Rev. B* **80**, 195110 (2009).

[131] Q. Li, G. Cao, S. Okamoto, J. Yi, W. Lin, B. C. Sales, J. Yan, R. Arita, J. Kuneš, A. V. Kozhevnikov *et al.*, "Atomically resolved spectroscopic study of Sr_2IrO_4: Experiment and theory", *Scientific reports* **3**, 3073 (2013).

[132] J. Nichols, N. Bray-Ali, A. Ansary, G. Cao and K.-W. Ng, "Tunneling into the Mott insulator Sr_2IrO_4", *Phys. Rev. B* **89**, 085125 (2014).

[133] J. Dai, E. Calleja, G. Cao and K. McElroy, "Local density of states study of a spin-orbit-coupling induced Mott insulator Sr_2IrO_4", *Phys. Rev. B* **90**, 041102 (2014).

[134] J. Kim, D. Casa, M. H. Upton, T. Gog, Y.-J. Kim, J. F. Mitchell, M. van Veenendaal, M. Daghofer, J. van den Brink, G. Khaliullin and B. J. Kim, "Magnetic Excitation Spectra of Sr_2IrO_4 Probed by Resonant Inelastic X-Ray Scattering: Establishing Links to Cuprate Superconductors", *Phys. Rev. Lett.* **108**, 177003 (2012).

[135] D. Hsieh, F. Mahmood, D. H. Torchinsky, G. Cao and N. Gedik, "Observation of a metal-to-insulator transition with both Mott-Hubbard and Slater characteristics in Sr_2IrO_4 from time-resolved photocarrier dynamics", *Phys. Rev. B* **86**, 035128 (2012).

[136] H. Watanabe, T. Shirakawa and S. Yunoki, "Theoretical study of insulating mechanism in multiorbital Hubbard models with a large spin-orbit coupling: Slater versus Mott scenario in Sr_2IrO_4", *Phys. Rev. B* **89**, 165115 (2014).

[137] I. V. Solovyev, V. V. Mazurenko and A. A. Katanin, "Validity and limitations of the superexchange model for the magnetic properties of Sr_2IrO_4 and Ba_2IrO_4 mediated by the strong spin-orbit coupling", *Phys. Rev. B* **92**, 235109 (2015).

[138] S. Fujiyama, H. Ohsumi, K. Ohashi, D. Hirai, B. J. Kim, T. Arima, M. Takata and H. Takagi, "Spin and Orbital Contributions to Magnetically Ordered Moments in $5d$ Layered Perovskite Sr_2IrO_4", *Phys. Rev. Lett.* **112**, 016405 (2014).

[139] J. Kim, M. Daghofer, A. H. Said, T. Gog, J. Van den Brink, G. Khaliullin and B. J. Kim, "Excitonic quasiparticles in a spin-orbit Mott insulator", *Nature Communications* **5**, 4453 (2014).

[140] F. Ye, S. Chi, B. C. Chakoumakos, J. A. Fernandez-Baca, T. Qi and G. Cao, "Magnetic and crystal structures of Sr_2IrO_4: A neutron diffraction study", *Phys. Rev. B* **87**, 140406 (2013).

[141] G. Cao, J. Bolivar, S. McCall, J. E. Crow and R. P. Guertin, "Weak ferromagnetism, metal-to-nonmetal transition, and negative differential resistivity in single-crystal Sr_2IrO_4", *Phys. Rev. B* **57**, R11039 (1998).

[142] T. Takayama, A. Matsumoto, G. Jackeli and H. Takagi, "Model analysis of magnetic susceptibility of Sr_2IrO_4: A two-dimensional $j_{eff} = \frac{1}{2}$ heisenberg system with competing interlayer couplings", *Phys. Rev. B* **94**, 224420 (2016).

[143] I. Battisti, K. M. Bastiaans, V. Fedoseev, A. De La Torre, N. Iliopoulos, A. Tamai, E. C. Hunter, R. S. Perry, J. Zaanen, F. Baumberger *et al.*, "Universality of pseudogap and emergent order in lightly doped mott insulators", *Nature Physics* **13**, 21 (2017).

[144] A. de la Torre, S. McKeown Walker, F. Y. Bruno, S. Riccó, Z. Wang, I. Gutierrez Lezama, G. Scheerer, G. Giriat, D. Jaccard, C. Berthod, T. K. Kim, M. Hoesch, E. C. Hunter, R. S. Perry, A. Tamai and F. Baumberger, "Collapse of the Mott Gap and Emergence of a Nodal Liquid in Lightly Doped Sr_2IrO_4", *Phys. Rev. Lett.* **115**, 176402 (2015).

[145] Y. K. Kim, N. Sung, J. Denlinger and B. Kim, "Observation of a d-wave gap in electron-doped Sr_2IrO_4", *Nature Physics* **12**, 37 (2016).

[146] H. Watanabe, T. Shirakawa and S. Yunoki, "Monte Carlo Study of an Unconventional Superconducting Phase in Iridium Oxide $j_{eff} = 1/2$ Mott Insulators Induced by Carrier Doping", *Phys. Rev. Lett.* **110**, 027002 (2013).

[147] Z. Y. Meng, Y. B. Kim and H.-Y. Kee, "Odd-Parity Triplet Superconducting Phase in Multiorbital Materials with a Strong Spin-Orbit Coupling: Application to Doped Sr_2IrO_4", *Phys. Rev. Lett.* **113**, 177003 (2014).

[148] Y. Yang, W.-S. Wang, J.-G. Liu, H. Chen, J.-H. Dai and Q.-H. Wang, "Superconductivity in doped Sr_2IrO_4: A functional renormalization group study", *Phys. Rev. B* **89**, 094518 (2014).

[149] Y. Gao, T. Zhou, H. Huang and Q.-H. Wang, "Possible superconductivity in Sr_2IrO_4 probed by quasiparticle interference", *Scientific reports* **5**, 9251 (2015).

[150] F. C. Zhang and T. M. Rice, "Effective Hamiltonian for the superconducting Cu oxides", *Phys. Rev. B* **37**, 3759 (1988).

[151] H. Gretarsson, N. H. Sung, J. Porras, J. Bertinshaw, C. Dietl, J. A. N. Bruin, A. F. Bangura, Y. K. Kim, R. Dinnebier, J. Kim, A. Al-Zein, M. Moretti Sala, M. Krisch, M. Le Tacon, B. Keimer and B. J. Kim, "Persistent Paramagnons Deep in the Metallic Phase of $Sr_{2-x}La_xIrO_4$", *Phys. Rev. Lett.* **117**, 107001 (2016).

[152] X. Chen, T. Hogan, D. Walkup, W. Zhou, M. Pokharel, M. Yao, W. Tian, T. Z. Ward, Y. Zhao, D. Parshall, C. Opeil, J. W. Lynn, V. Madhavan and S. D. Wilson, "Influence of electron doping on the ground state of $Sr_{2-x}La_xIrO_4$", *Phys. Rev. B* **92**, 075125 (2015).

[153] X. Chen, J. L. Schmehr, Z. Islam, Z. Porter, E. Zoghlin, K. Finkelstein, J. P. Ruff and S. D. Wilson, "Unidirectional spin density wave state in metallic $Sr_{2-x}La_xIrO_4$", *Nature Communications* **9**, 103 (2018).

[154] V. Brouet, J. Mansart, L. Perfetti, C. Piovera, I. Vobornik, P. Le Fèvre,
F. Bertran, S. C. Riggs, M. C. Shapiro, P. Giraldo-Gallo and I. R. Fisher,
"Transfer of spectral weight across the gap of Sr_2IrO_4 induced by La doping",
Phys. Rev. B **92**, 081117 (2015).

[155] K. Terashima, M. Sunagawa, H. Fujiwara, T. Fukura, M. Fujii, K. Okada,
K. Horigane, K. Kobayashi, R. Horie, J. Akimitsu, E. Golias, D. Marchenko,
A. Varykhalov, N. L. Saini, T. Wakita, Y. Muraoka and T. Yokoya, "Evolution of
the remnant Fermi-surface state in the lightly doped correlated spin-orbit insulator
$Sr_{2-x}La_xIrO_4$", *Phys. Rev. B* **96**, 041106 (2017).

[156] Y. K. Kim, O. Krupin, J. D. Denlinger, A. Bostwick, E. Rotenberg, Q. Zhao, J. F.
Mitchell, J. W. Allen and B. J. Kim, "Fermi arcs in a doped pseudospin-1/2
Heisenberg antiferromagnet", *Science* **345**, 187 (2014).

[157] J. P. Clancy, A. Lupascu, H. Gretarsson, Z. Islam, Y. F. Hu, D. Casa, C. S.
Nelson, S. C. LaMarra, G. Cao and Y.-J. Kim, "Dilute magnetism and spin-orbital
percolation effects in $Sr_2Ir_{1-x}Rh_xO_4$", *Phys. Rev. B* **89**, 054409 (2014).

[158] T. F. Qi, O. B. Korneta, L. Li, K. Butrouna, V. S. Cao, X. Wan, P. Schlottmann,
R. K. Kaul and G. Cao, "Spin-orbit tuned metal-insulator transitions in
single-crystal $Sr_2Ir_{1-x}Rh_xO_4$ ($0 \leq x \leq 1$)", *Phys. Rev. B* **86**, 125105 (2012).

[159] Y. Cao, Q. Wang, J. A. Waugh, T. J. Reber, H. Li, X. Zhou, S. Parham, S.-R.
Park, N. C. Plumb, E. Rotenberg, A. Bostwick, J. D. Denlinger, T. Qi, M. A.
Hermele, G. Cao and D. S. Dessau, "Hallmarks of the Mott-metal crossover in the
hole-doped pseudospin-1/2 Mott insulator Sr_2IrO_4", *Nature Communications* **7**,
11367 (2016).

[160] S. Chikara, G. Fabbris, J. Terzic, G. Cao, D. Khomskii and D. Haskel, "Charge
partitioning and anomalous hole doping in Rh-doped Sr_2IrO_4", *Phys. Rev. B* **95**,
060407 (2017).

[161] S. Chikara, G. Fabbris, J. Terzic, G. Cao, D. Khomskii and D. Haskel, "Charge
partitioning and anomalous hole doping in rh-doped Sr_2IrO_4", *Phys. Rev. B* **95**,
060407 (2017).

[162] J. Jeong, Y. Sidis, A. Louat, V. Brouet and P. Bourges, "Time-reversal symmetry
breaking hidden order in Sr_2IrO_4", *Nature Communications* **8**, 15119 (2017).

[163] C. M. Williams, N. C. Koon and J. B. Milstein, "Cubic harmonic analysis of
magnetic anisotropy measurements on single crystal $Ho_xTb_{1-x}Fe_2$ laves phase
compounds", *Solid State Communications* **39**, 823 (1978).

[164] U. Atzmony, M. P. Dariel, E. R. Bauminger, D. Lebenbaum, I. Nowik and S. Ofer,
"Spin-Orientation Diagrams and Magnetic Anisotropy of Rare-Earth-Iron Ternary
Cubic Laves Compounds", *Phys. Rev. B* **7**, 4220 (1973).

[165] F. M. Mueller and M. G. Priestley, "Inversion of Cubic de Haas-van Alphen Data,
with an Application to Palladium", *Physical Review* **148**, 638 (1966).

[166] G. Aubert, D. Gignoux, B. Michelutti and A. N. Saada, "Torque measurements in the basal plane of a DyNi$_5$ crystal", *Journal of Magnetism and Magnetic Materials* **15-18**, 551 (1980).

[167] A. del Moral, J. Arnaudas, J. Cockaday and E. Lee, "Magnetic anisotropy in the paramagnetic phase of TbAl$_2$", *Journal of Magnetism and Magnetic Materials* **40**, 331 (1984).

[168] L. M. Pecora, "The reconstruction of the anisotropy free energy function from magnetic torque data", *Journal of Magnetism and Magnetic Materials* **82**, 57 (1989).

[169] S. Uji, K. Kodama, K. Sugii, T. Terashima, Y. Takahide, N. Kurita, S. Tsuchiya, M. Kimata, A. Kobayashi, B. Zhou and H. Kobayashi, "Magnetic torque studies on FFLO phase in magnetic-field-induced organic superconductor λ-(BETS)$_2$FeCl$_4$", *Phys. Rev. B* **85**, 174530 (2012).

[170] B. Bergk, A. Demuer, I. Sheikin, Y. Wang, J. Wosnitza, Y. Nakazawa and R. Lortz, "The Fulde-Ferrell-Larkin-Ovchinnikov state in the organic superconductor κ-(BEDT-TTF)$_2$Cu(NCS)$_2$ as observed in magnetic-torque experiments", *Physica C: Superconductivity and its Applications* **470**, S586 (2010).

[171] B. Bergk, A. Demuer, I. Sheikin, Y. Wang, J. Wosnitza, Y. Nakazawa and R. Lortz, "Magnetic torque evidence for the Fulde-Ferrell-Larkin-Ovchinnikov state in the layered organic superconductor κ-(BEDT-TTF)$_2$Cu(NCS)$_2$", *Phys. Rev. B* **83**, 064506 (2011).

[172] C.-w. Cho, J. Lyu, C. Y. Ng, J. J. He, K. T. Lo, D. Chareev, T. A. Abdel-Baset, M. Abdel-Hafiez and R. Lortz, "Evidence for the Fulde-Ferrell-Larkin-Ovchinnikov state in bulk NbS$_2$", *Nature Communications* **12**, 3676 (2021).

[173] J. C. Martínez, S. H. Brongersma, A. Koshelev, B. Ivlev, P. H. Kes, R. P. Griessen, D. G. de Groot, Z. Tarnavski and A. A. Menovsky, "Magnetic anisotropy of a Bi$_2$Sr$_2$CaCu$_2$O$_x$ single crystal", *Phys. Rev. Lett.* **69**, 2276 (1992).

[174] S. Tsuchiya, J.-i. Yamada, K. Sugii, D. Graf, J. S. Brooks, T. Terashima and S. Uji, "Phase Boundary in a Superconducting State of κ-(BEDT-TTF)$_2$Cu(NCS)$_2$: Evidence of the Fulde-Ferrell-Larkin-Ovchinnikov Phase", *Journal of the Physical Society of Japan* **84**, 034703 (2015).

[175] S. Sugiura, T. Isono, T. Terashima, S. Yasuzuka, J. A. and S. Uji, "Fulde-Ferrell-Larkin-Ovchinnikov and vortex phases in a layered organic superconductor", *npj Quant Mater* **4**, 7 (2019).

[176] M. S. Dresselhaus, G. Dresselhaus and A. Jorio, *Grouop Theory: Application to the Physics of Condensed Matter*. Springer, 2007.

[177] T. Konno, *Symmetry in Matter and Group Theory*. KYORITSU SHUPPAN, 2001.

[178] R. Okazaki, T. Shibauchi, H. J. Shi, Y. Haga, T. D. Matsuda, E. Yamamoto, Y. Onuki, H. Ikeda and Y. Matsuda, "Rotational Symmetry Breaking in the Hidden-Order Phase of URu$_2$Si$_2$", *Science* **331**, 439 (2011).

[179] T. Shibauchi and Y. Matsuda, "Thermodynamic evidence for broken fourfold rotational symmetry in the hidden-order phase of URu$_2$Si$_2$", *Physica C: Superconductivity* **481**, 229 (2012).

[180] T. T. M. Palstra, A. A. Menovsky, J. v. d. Berg, A. J. Dirkmaat, P. H. Kes, G. J. Nieuwenhuys and J. A. Mydosh, "Superconducting and Magnetic Transitions in the Heavy-Fermion System URu$_2$Si$_2$", *Phys. Rev. Lett.* **55**, 2727 (1985).

[181] S. Kasahara, H. J. Shi, K. Hashimoto, S. Tonegawa, Y. Mizukami, T. Shibauchi, K. Sugimoto, T. Fukuda, T. Terashima, A. H. Nevidomskyy and Y. Matsuda, "Electronic nematicity above the structural and superconducting transition in BaFe$_2$(As$_{1-x}$P$_x$)$_2$", *Nature* **486**, 382 (2012).

[182] Y. Matsubayashi, K. Sugii, D. Hirai, Z. Hiroi, T. Hasegawa, S. Sugiura, H. T. Hirose, T. Terashima and S. Uji, "Coexistence of odd-parity and even-parity order parameters in the multipole order phase of the spin-orbit coupled metal Cd$_2$Re$_2$O$_7$", *Phys. Rev. B* **101**, 205133 (2020).

[183] J. C. Petersen, M. D. Caswell, J. S. Dodge, I. A. Sergienko, J. He, R. Jin and D. Mandrus, "Nonlinear optical signatures of the tensor order in Cd$_2$Re$_2$O$_7$", *Nature Physics* **2**, 605 (2006).

[184] J. W. Harter, Z. Y. Zhao, J.-Q. Yan, D. G. Mandrus and D. Hsieh, "A parity-breaking electronic nematic phase transition in the spin-orbit coupled metal Cd$_2$Re$_2$O$_7$", *Science* **356**, 295–299 (2017).

[185] C. Rossel, P. Bauer, D. Zech, J. Hofer, M. Willemin and H. Keller, "Active microlevers as miniature torque magnetometers", *Journal of Applied Physics* **79**, 8166 (1996).

[186] E. Ohmichi and T. Osada, "Torque magnetometry in pulsed magnetic fields with use of a commercial microcantilever", *Review of Scientific Instruments* **73**, 3022 (2002).

[187] H. Murayama, Y. Sato, R. Kurihara, S. Kasahara, Y. Mizukami, Y. Kasahara, H. Uchiyama, A. Yamamoto, E.-G. Moon, J. Cai *et al.*, "Diagonal nematicity in the pseudogap phase of HgBa$_2$CuO$_{4+\delta}$", *Nature Communications* **10**, 3282 (2019).

[188] S. N. Putilin, E. V. Antipov, O. l. Chmaissem and M. Marezio, "Superconductivity at 94 K in HgBa$_2$CuO$_{4+\delta}$", *Nature* **362**, 226 (1993).

[189] A. Yamamoto, W.-Z. Hu, F. Izumi and S. Tajima, "Superconducting and structural properties of nearly carbonate-free HgBa$_2$CuO$_{4+\delta}$", *Physica C: Superconductivity* **351**, 329 (2001).

[190] Y. Li, V. Balédent, N. Barišić, Y. C. Cho, Y. Sidis, G. Yu, X. Zhao, P. Bourges and M. Greven, "Magnetic order in the pseudogap phase of $HgBa_2CuO_{4+\delta}$ studied by spin-polarized neutron diffraction", *Phys. Rev. B* **84**, 224508 (2011).

[191] W. Tabis, B. Yu, I. Bialo, M. Bluschke, T. Kolodziej, A. Kozlowski, E. Blackburn, K. Sen, E. M. Forgan, M. v. Zimmermann, Y. Tang, E. Weschke, B. Vignolle, M. Hepting, H. Gretarsson, R. Sutarto, F. He, M. Le Tacon, N. Barišić, G. Yu *et al.*, "Synchrotron x-ray scattering study of charge-density-wave order in $HgBa_2CuO_{4+\delta}$", *Phys. Rev. B* **96**, 134510 (2017).

[192] A. Schilling, M. Cantoni, J. D. Guo and H. R. Ott, "Superconductivity above 130 K in the Hg-Ba-Ca-Cu-O system", *Nature* **363**, 56 (1993).

[193] I. M. Vishik, N. Barišić, M. K. Chan, Y. Li, D. D. Xia, G. Yu, X. Zhao, W. S. Lee, W. Meevasana, T. P. Devereaux, M. Greven and Z.-X. Shen, "Angle-resolved photoemission spectroscopy study of $HgBa_2CuO_{4+\delta}$", *Phys. Rev. B* **89**, 195141 (2014).

[194] M. S. Grbić, N. Barišić, A. Dulčić, I. Kupčić, Y. Li, X. Zhao, G. Yu, M. Dressel, M. Greven and M. Požek, "Microwave measurements of the in-plane and c-axis conductivity in $HgBa_2CuO_{4+\delta}$: Discriminating between superconducting fluctuations and pseudogap effects", *Phys. Rev. B* **80**, 094511 (2009).

[195] S. I. Mirzaei, D. Stricker, J. N. Hancock, C. Berthod, A. Georges, E. van Heumen, M. K. Chan, X. Zhao, Y. Li, M. Greven, N. Barišić and D. van der Marel, "Spectroscopic evidence for Fermi liquid-like energy and temperature dependence of the relaxation rate in the pseudogap phase of the cuprates", *Proceedings of the National Academy of Sciences* **110**, 5774 (2013).

[196] S. A. Sreedhar, A. Rossi, J. Nayak, Z. W. Anderson, Y. Tang, B. Gregory, M. Hashimoto, D.-H. Lu, E. Rotenberg, R. J. Birgeneau, M. Greven, M. Yi and I. M. Vishik, "Three interaction energy scales in the single-layer high-T_c cuprate $HgBa_2CuO_{4+\delta}$", *Phys. Rev. B* **102**, 205109 (2020).

[197] J. M. Harris, Y. F. Yan, P. Matl, N. P. Ong, P. W. Anderson, T. Kimura and K. Kitazawa, "Violation of Kohler's Rule in the Normal-State Magnetoresistance of $YBa_2Cu_3O_{7-\delta}$ and $La_2Sr_xCuO_4$", *Phys. Rev. Lett.* **75**, 1391 (1995).

[198] K. Semba and A. Matsuda, "Vanishingly small Maki-Thompson superconducting fluctuation in the magnetoresistance of high-t_c superconductors", *Phys. Rev. B* **55**, 11103 (1997).

[199] T. Kimura, S. Miyasaka, H. Takagi, K. Tamasaku, H. Eisaki, S. Uchida, K. Kitazawa, M. Hiroi, M. Sera and N. Kobayashi, "In-plane and out-of-plane magnetoresistance in $La_{2-x}Sr_xCuO_4$ single crystals", *Phys. Rev. B* **53**, 8733 (1996).

[200] J. Y. T. Wei, C. C. Tsuei, P. J. M. van Bentum, Q. Xiong, C. W. Chu and M. K. Wu, "Quasiparticle tunneling spectra of the high-T_c mercury cuprates: Implications of the d-wave two-dimensional van Hove scenario", *Phys. Rev. B* **57**, 3650 (1998).

[201] W. Guyard, M. Le Tacon, M. Cazayous, A. Sacuto, A. Georges, D. Colson and A. Forget, "Breakpoint in the evolution of the gap through the cuprate phase diagram", *Phys. Rev. B* **77**, 024524 (2008).

[202] C. M. Varma, "Non-fermi-liquid states and pairing instability of a general model of copper oxide metals", *Phys. Rev. B* **55**, 14554 (1997).

[203] P. Bourges and Y. Sidis, "Novel magnetic order in the pseudogap state of high-T_c copper oxides superconductors", *Comptes Rendus Physique* **12**, 461 (2011).

[204] C. Weber, A. Läuchli, F. Mila and T. Giamarchi, "Orbital Currents in Extended Hubbard Models of High-T_c Cuprate Superconductors", *Phys. Rev. Lett.* **102**, 017005 (2009).

[205] V. M. Yakovenko, "Tilted loop currents in cuprate superconductors", *Physica B: Condensed Matter* **460**, 159 (2015).

[206] Y. Tang, L. Mangin-Thro, A. Wildes, M. K. Chan, C. J. Dorow, J. Jeong, Y. Sidis, M. Greven and P. Bourges, "Orientation of the intra-unit-cell magnetic moment in the high-T_c superconductor HgBa$_2$CuO$_{4+\delta}$", *Phys. Rev. B* **98**, 214418 (2018).

[207] Y. Li, V. Balédent, G. Yu, N. Barišić, K. Hradil, R. A. Mole, Y. Sidis, P. Steffens, X. Zhao, P. Bourges *et al.*, "Hidden magnetic excitation in the pseudogap phase of a high-t_c superconductor", *Nature* **468**, 283 (2010).

[208] S. Pailhès, Y. Sidis, P. Bourges, V. Hinkov, A. Ivanov, C. Ulrich, L. P. Regnault and B. Keimer, "Resonant magnetic excitations at high energy in superconducting YBa$_2$Cu$_3$O$_{6.85}$", *Phys. Rev. Lett.* **93**, 167001 (2004).

[209] J. Tranquada, H. Woo, T. Perring, H. Goka, G. Gu, G. Xu, M. Fujita and K. Yamada, "Quantum magnetic excitations from stripes in copper oxide superconductors", *Nature* **429**, 534 (2004).

[210] M. K. Chan, C. J. Dorow, L. Mangin-Thro, Y. Tang, Y. Ge, M. J. Veit, G. Yu, X. Zhao, A. D. Christianson, J. T. Park, Y. Sidis, P. Steffens, D. L. Abernathy, P. Bourges and M. Greven, "Commensurate antiferromagnetic excitations as a signature of the pseudogap in the tetragonal high-T_c cuprate HgBa$_2$CuO$_{4+\delta}$", *Nature Communications* **7**, 10819 (2016).

[211] M. K. Chan, Y. Tang, C. J. Dorow, J. Jeong, L. Mangin-Thro, M. J. Veit, Y. Ge, D. L. Abernathy, Y. Sidis, P. Bourges and M. Greven, "Hourglass Dispersion and Resonance of Magnetic Excitations in the Superconducting State of the Single-Layer Cuprate HgBa$_2$CuO$_{4+\delta}$ Near Optimal Doping", *Phys. Rev. Lett.* **117**, 277002 (2016).

[212] G. Yu, Y. Li, E. M. Motoyama, X. Zhao, N. Barišić, Y. Cho, P. Bourges, K. Hradil, R. A. Mole and M. Greven, "Magnetic resonance in the model high-temperature superconductor HgBa$_2$CuO$_{4+\delta}$", *Phys. Rev. B* **81**, 064518 (2010).

[213] D. LeBoeuf, N. Doiron-Leyraud, J. Levallois, R. Daou, J.-B. Bonnemaison, N. E. Hussey, L. Balicas, B. J. Ramshaw, R. Liang, D. A. Bonn, W. N. Hardy, S. Adachi, C. Proust and L. Taillefer, "Electron pockets in the Fermi surface of hole-doped high-T_c superconductors", *Nature* **450**, 533 (2007).

[214] N. Baršić, S. Badoux, M. K. Chan, C. Dorow, W. Tabis, B. Vignolle, G. Yu, J. Béard, X. Zhao, C. Proust and M. Greven, "Universal quantum oscillations in the underdoped cuprate superconductors", *Nature Physics* **9**, 761 (2013).

[215] M. K. Chan, N. Harrison, R. D. Mcdonald, B. Ramshaw, K. A. Modic, N. Barišić and M. Greven, "Single reconstructed Fermi surface pocket in an underdoped single-layer cuprate superconductor", *Nature Communications* **7**, 12244 (2016).

[216] W. Tabiś, P. Popčević, B. Klebel-Knobloch, I. Biało, C. M. N. Kumar, B. Vignolle, M. Greven and N. Barišić, *Arc-to-pocket transition and quantitative understanding of transport properties in cuprate superconductors*, 2021.

[217] A. Yamamoto, W.-Z. Hu and S. Tajima, "Thermoelectric power and resistivity of $HgBa_2CuO_{4+\delta}$ over a wide doping range", *Phys. Rev. B* **63**, 024504 (2000).

[218] X. Zhao, G. Yu, Y.-C. Cho, G. Chabot-Couture, N. Barišić, P. Bourges, N. Kaneko, Y. Li, L. Lu, E. Motoyama, O. Vajk and M. Greven, "Crystal Growth and Characterization of the Model High-Temperature Superconductor $HgBa_2CuO_{4+\delta}$", *Advanced Materials* **18**, 3243 (2006).

[219] D. C. Johnston and J. H. Cho, "Magnetic-susceptibility anisotropy of single-crystal $Bi_2Sr_2CaCu_2O_8$", *Phys. Rev. B* **42**, 8710 (1990).

[220] T. Watanabe, T. Fujii and A. Matsuda, "Pseudogap in $Bi_2Sr_2CaCu_2O_{8+\delta}$ Studied by Measuring Anisotropic Susceptibilities and Out-of-Plane Transport", *Phys. Rev. Lett.* **84**, 5848 (2000).

[221] Y. Itoh, T. Machi and A. Yamamoto, "Magnetic susceptibility of optimally doped $HgBa_2CuO_{4+\delta}$", *Phys. Rev. B* **96**, 235118 (2017).

[222] M. Tuominen, A. M. Goldman, Y. Z. Chang and P. Z. Jiang, "Magnetic anisotropy of high-T_c superconductors", *Phys. Rev. B* **42**, 412 (1990).

[223] J. Mosqueira, R. I. Rey and F. Vidal, "Magnetization vector in the reversible region of the highly anisotropic cuprate superconductor $Tl_2Ba_2Ca_2O_{10}$: Anisotropy factor and the role of two-dimensional vortex fluctuations", *Phys. Rev. B* **81**, 174509 (2010).

[224] V. G. Kogan, M. M. Fang and S. Mitra, "Reversible magnetization of high-T_c materials in intermediate fields", *Phys. Rev. B* **38**, 11958 (1988).

[225] C. C. Todari, M. A. Subramanian, J. C. Calabrese, J. Gopalakrishnan, K. J. Morrissey, T. R. Askew, R. B. Flippen, U. Chowdhry and A. W. Sleight, "Crystal Structure of $Tl_2Ba_2Ca_2Cu_3O_{10}$, a 125 K Superconductor", *Science* **240**, 631 (1988).

[226] Z. Hao, "Transverse magnetization, torque, and anisotropy in anisotropic type-II superconductors in the mixed state", *Phys. Rev. B* **48**, 16822 (1993).

[227] K. Ishida, S. Hosoi, Y. Teramoto, T. Usui, Y. Mizukami, K. Itaka, Y. Matsuda, T. Watanabe and T. Shibauchi, "Divergent nematic susceptibility near the pseudogap critical point in a cuprate superconductor", *Journal of the Physical Society of Japan* **89**, 064707 (2020).

[228] S. Lee, J. Jung, A. Go and E.-G. Moon, *Exotic Z_2 Symmetry Breaking Transitions in 2D Correlated Systems*, 2018.

[229] N. Gauquelin, D. Hawthorn, G. Sawatzky, R. Liang, D. Bonn, W. Hardy and G. Botton, "Atomic scale real-space mapping of holes in $YBa_2Cu_3O_{6+\delta}$", *Nature Communications* **5**, 4275 (2014).

[230] M. Magnuson, T. Schmitt, V. N. Strocov, J. Schlappa, A. S. Kalabukhov and L.-C. Duda, "Self-doping processes between planes and chains in the metal-to-superconductor transition of $YBa_2Cu_3O_{6.9}$", *Scientific reports* **4**, 1 (2014).

[231] S. Nakata, M. Horio, K. Koshiishi, K. Hagiwara, C. Lin, M. Suzuki, S. Ideta, K. Tanaka, D. Song, Y. Yoshida *et al.*, "Nematicity in a cuprate superconductor revealed by angle-resolved photoemission spectroscopy under uniaxial strain", *npj Quantum Materials* **6**, 86 (2021).

[232] S. De Almeida-Didry, Y. Sidis, V. Balédent, F. Giovannelli, I. Monot-Laffez and P. Bourges, "Evidence for intra-unit-cell magnetic order in $Bi_2Sr_2CaCu_2O_{8+\delta}$", *Phys. Rev. B* **86**, 020504 (2012).

[233] K. K. Gomes, A. N. Pasupathy, A. Pushp, S. Ono, Y. Ando and A. Yazdani, "Visualizing pair formation on the atomic scale in the high-T_c superconductor $Bi_2Sr_2\,CaCu_2O_{8+\delta}$", *Nature* **447**, 569 (2007).

[234] M. Hashimoto, I. M. Vishik, R.-H. He, T. P. Devereaux and Z.-X. Shen, "Energy gaps in high-transition-temperature cuprate superconductors", *Nature Physics* **10**, 483 (2014).

[235] T. A. Webb, M. C. Boyer, Y. Yin, D. Chowdhury, Y. He, T. Kondo, T. Takeuchi, H. Ikuta, E. W. Hudson, J. E. Hoffman and M. H. Hamidian, "Density Wave Probes Cuprate Quantum Phase Transition", *Phys. Rev. X* **9**, 021021 (2019).

[236] M. J. Rice, "Electron-Electron Scattering in Transition Metals", *Phys. Rev. Lett.* **20**, 1439 (1968).

[237] B. Zwartsenberg, R. P. Day, E. Razzoli, M. Michiardi, N. Xu, M. Shi, J. D. Denlinger, G. Cao, S. Calder, K. Ueda, J. Bertinshaw, H. Takagi, B. J. Kim, I. S. Elfimov and A. Damascelli, "Spin-orbit-controlled metal–insulator transition in Sr_2IrO_4", *Nature Physics* **16**, 290 (2020).

[238] A. Louat, F. Bert, L. Serrier-Garcia, F. Bertran, P. Le Fèvre, J. Rault and V. Brouet, "Formation of an incoherent metallic state in Rh-doped Sr_2IrO_4", *Phys. Rev. B* **97**, 161109 (2018).

[239] D. Song, G. Han, W. Kyung, J. Seo, S. Cho, B. S. Kim, M. Arita, K. Shimada, H. Namatame, M. Taniguchi, Y. Yoshida, H. Eisaki, S. R. Park and C. Kim, "Electron Number-Based Phase Diagram of $Pr_{1-x}LaCe_xCuO_{4-\delta}$ and Possible Absence of Disparity between Electron- and Hole-Doped Cuprate Phase Diagrams", *Phys. Rev. Lett.* **118**, 137001 (2017).

[240] N. P. Armitage, F. Ronning, D. H. Lu, C. Kim, A. Damascelli, K. M. Shen, D. L. Feng, H. Eisaki, Z.-X. Shen, P. K. Mang, N. Kaneko, M. Greven, Y. Onose, Y. Taguchi and Y. Tokura, "Doping Dependence of an n-Type Cuprate Superconductor Investigated by Angle-Resolved Photoemission Spectroscopy", *Phys. Rev. Lett.* **88**, 257001 (2002).

[241] J. P. Clancy, H. Gretarsson, M. H. Upton, J. Kim, G. Cao and Y.-J. Kim, "Magnetic excitations in hole-doped Sr_2IrO_4: Comparison with electron-doped cuprates", *Phys. Rev. B* **100**, 104414 (2019).

[242] C. J. Jia, E. A. Nowadnick, K. Wohlfel, Y. F. Kung, C.-C. Chen, S. Johnston, T. Tohyama, B. Moritz and T. P. Devereaux, "Persistent spin excitations in doped antiferromagnets revealed by resonant inelastic light scattering", *Nature Communication* **5**, 3314 (2014).

[243] W. S. Lee, J. J. Lee, E. A. Nowadnick, S. Gerber, W. Tabis, S. W. Huang, V. N. Strocov, E. M. Motoyama, G. Yu, B. Moritz, H. Y. Huang, R. P. Wang, Y. B. Huang, W. B. Wu, C. T. Chen, D. J. Huang, M. Greven, T. Schmitt, Z. X. Shen and T. P. Devereaux, "Asymmetry of collective excitations in electron- and hole-doped cuprate superconductors", *Nature Physics* **10**, 883 (2014).

[244] L. C. Chapon and S. W. Lovesey, "The magnetic motif and the wavefunction of Kramers ions in strontium iridate (Sr_2IrO_4)", *Journal of Physics: Condensed Matter* **23**, 252201 (2011).

[245] S. Calder, G.-X. Cao, M. D. Lumsden, J. W. Kim, Z. Gai, B. C. Sales, D. Mandrus and A. D. Christianson, "Magnetic structural change of Sr_2IrO_4 upon Mn doping", *Phys. Rev. B* **86**, 220403 (2012).

[246] O. P. Vajk, P. K. Mang, M. Greven, P. M. Gehring and J. W. Lynn, "Quantum Impurities in the Two-Dimensional Spin One-Half Heisenberg Antiferromagnet", *Science* **295**, 1691 (2002).

[247] L. Fruchter, D. Colson and V. Brouet, "Magnetic critical properties and basal-plane anisotropy of Sr_2IrO_4", *Journal of Physics: Condensed Matter* **28**, 126003 (2016).

[248] M. Herak, M. Miljak, G. Dhalenne and A. Revcolevschi, "Easy plane anisotropy in Bi_2CuO_4", *Journal of Physics: Condensed Matter* **22**, 026006 (2009).

[249] H. Murayama, K. Ishida, R. Kurihara, T. Ono, Y. Sato, Y. Kasahara, H. Watanabe, Y. Yanase, G. Cao, Y. Mizukami, T. Shibauchi, Y. Matsuda and S. Kasahara, "Bond Directional Anapole Order in a Spin-Orbit Coupled Mott Insulator $Sr_2Ir_{1-x}Rh_xO_4$", *Phys. Rev. X* **11**, 011021 (2021).

[250] H. Murayama, Y. Sato, R. Kurihara, S. Kasahara, Y. Mizukami, Y. Kasahara, H. Uchiyama, A. Yamamoto, E.-G. Moon, J. Cai, J. Freyermuth, M. Greven, T. Shibauchi and Y. Matsuda, "Diagonal nematicity in the pseudogap phase of $HgBa_2CuO_{4+\delta}$", *Nature Communications* **10**, 3282 (2019).

[251] J.-H. Chu, H.-H. Kuo, J. G. Analytis and I. R. Fisher, "Divergent nematic susceptibility in an iron arsenide superconductor", *Science* **337**, 710 (2012).

[252] A. Shekhter and C. M. Varma, "Considerations on the symmetry of loop order in cuprates", *Phys. Rev. B* **80**, 214501 (2009).

[253] N. A. Spaldin, M. Fiebig and M. Mostovoy, "The toroidal moment in condensed-matter physics and its relation to the magnetoelectric effect", *Journal of Physics: Condensed Matter* **20**, 434203 (2008).

[254] Y. F. Popov, A. M. Kadomtseva, G. P. Vorobév, V. A. Timofeeva, D. M. Ustinin, A. K. Zvezdin and M. M. Tegeranchi, "Magnetoelectric effect and toroidal ordering in $Ga_{2-x}Fe_xO_3$", *Journal of Experimental and Theoretical Physics* **87**, 146 (1998).

[255] Y. F. Popov, A. M. Kadomtseva, D. V. Belov, G. P. Vorobév and A. Zvezdin, "Magnetic-field-induced toroidal moment in the magnetoelectric Cr_2O_3", *Journal of Experimental and Theoretical Physics Letters* **69**, 330 (1999).

[256] B. B. Van Aken, J.-P. Rivera, H. Schmid and M. Fiebig, "Observation of ferrotoroidic domains", *Nature* **449**, 702 (2007).

[257] A. S. Zimmermann, D. Meier and M. Fiebig, "Ferroic nature of magnetic toroidal order", *Nature Communications* **5**, 4796 (2014).

[258] H. Saito, K. Uenishi, N. Miura, C. Tabata, H. Hidaka, T. Yanagisawa and H. Amitsuka, "Evidence of a New Current-Induced Magnetoelectric Effect in a Toroidal Magnetic Ordered State of UNi_4B", *Journal of the Physical Society of Japan* **87**, 033702 (2018).

[259] I. B. Zel'Dovich, "Electromagnetic interaction with parity violation", *Sov. Phys. JETP* **6**, 1184 (1958).

[260] H. Watanabe and Y. Yanase, "Photocurrent response in parity-time symmetric current-ordered states", *Phys. Rev. B* **104**, 024416 (2021).

Publication

Main papers

1. <u>H. Murayama</u>, Y. Sato, R. Kurihara, S. Kasahara, Y. Mizukami, Y. Kasahara, H. Uchiyama, A. Yamamoto, E.-G. Moon, J. Cai, J. Freyermuth, M. Greven, T. Shibauchi and Y. Matsuda
"Diagonal nematicity in the pseudogap phase of $HgBa_2CuO_{4+\delta}$"
Nature Communications **10**, 3282 (2019); arXiv:1805.00276.

2. <u>H. Murayama</u>, K. Ishida, R. Kurihara, T. Ono, Y. Sato, Y. Kasahara, H. Watanabe, Y. Yanase, G. Cao, Y. Mizukami, T. Shibauchi, Y. Matsuda and S. Kasahara
"Bond Directional Anapole Order in a Spin-Orbit Coupled Mott Insulator $Sr_2(Ir_{1-x}Rh_x)O_4$"
Phys. Rev. X **11**, 011021 (2021); arXiv:2008.06380.

Reference papers

1. Y. Sato, S. Kasahara, <u>H. Murayama</u>, Y. Kasahara, E.-G. Moon, T. Nishizaki, T. Loew, J. Porras, B. Keimer, T. Shibauchi and Y. Matsuda
"Thermodynamic evidence for a nematic phase transition at the onset of the pseudogap in $YBa_2Cu_3O_y$"
Nature Physics **13**, 1074–1078 (2017); arXiv:1706.05214.

2. Y. Sato, Z. Xiang, Y. Kasahara, T. Taniguchi, S. Kasahara, L. Chen, T. Asaba, C. Tinsman, <u>H. Murayama</u>, O. Tanaka, Y. Mizukami, T. Shibauchi, F. Iga, J. Singleton, Lu Li and Y. Matsuda
"Unconventional thermal metallic state of charge-neutral fermions in an insulator"
Nature Physics **15**, 954-959 (2019); arXiv:1905.05357.

3. <u>H. Murayama</u>, Y. Sato, T. Taniguchi, R. Kurihara, X. Z. Xing, W. Huang, S. Kasahara, Y. Kasahara, I. Kimchi, M. Yoshida, Y. Iwasa, Y. Mizukami, T. Shibauchi, M. Konczykowski and Y. Matsuda
"Effect of quenched disorder on the quantum spin liquid state of the triangular-lattice antiferromagnet $1T-TaS_2$"
Phys. Rev. Research **2**, 013099 (2020); arXiv:1909.00583.

4. <u>H. Murayama</u>, T. Tominaga, T. Asaba, A. de Oliveira Silva, Y. Sato, H. Suzuki, Y. Ukai, S. Suetsugu, Y. Kasahara, R. Okuma, I. Kimchi and Y. Matsuda
"Universal scaling of the specific heat in $S = 1/2$ quantum kagome antiferromagnet

herbertsmithite"
arXiv:2106.07223.

Acknowledgment